Phuong Chi Hoang
Kurt-Schumacher-Str. 22
D-67663 Kaiserslautern
Geburtsort: Hanoi/Vietnam

Applications of Photonic Crystals in Communications Engineering and Optical Imaging

deutscher Titel:

Anwendungen der Photonischen Kristalle in der Kommunikationstechnik und bei der Optischen Abbildung

Vom Fachbereich Elektrotechnik und Informationstechnik
der Technischen Universität Kaiserslautern
zur Verleihung des akademischen Grades
Doktor der Ingenieurwissenschaften (Dr.-Ing.)
genehmigte Dissertation
D 386
von
M.Sc. Phuong Chi Hoang

Tag der Einreichung:	22. Oktober 2008
Tag der mündlichen Prüfung:	22. Januar 2009
Dekan des Fachbereichs Elektrotechnik:	Univ.-Prof. Dr. Steven Liu
Vorsitzender der Prüfungskommission:	Prof. Dr.-Ing. Andreas König
1. Berichterstatter:	Prof. Dr.-Ing. Remigius Zengerle
2. Berichterstatter:	Prof. Dr.-Ing. habil. Dr.-Ing. E.h. Paul Walter Baier

Acknowledgements

I would like to express my gratefulness to Prof. Dr.-Ing. R. Zengerle who supported me consistently during my PhD thesis. With plentiful experiences in the area of optical communications, he gave me many useful suggestions from the choosing the topic of my PhD thesis to the detailed steps in the implementation of my PhD thesis.

I would like to thank Dipl.-Ing. R. Stemler for his very careful preparation for my working place. All the computer systems always run well under his installation and maintenance.

I would like to thank Prof. Dr.-Ing. habil. Dr.-Ing. E. h. Paul Walter Baier for taking time to review my dissertation and for very useful suggestions.

I would like to thank Prof. Dr.-Ing. Andreas König for being the presider of my PhD examination.

I also like to thank all the team workers at the chair of Electrodymanic and Optical Technology for always making a friendly cooperative environment.

And I also like to thank Dr.-Ing. Bernd Gutheil and Dr.-Ing. habil. C. Tuttas for their help during my study in Germany.

Finally, I would like to give my special thanks to my husband, my mother, my father, and my brother, who are always by my side to encourage me all the time.

Chapter 1

Introduction

1.1 Definition of photonic crystals

Photonic crystals (PhCs) are inhomogeneous dielectric media with periodic variation of the refractive index. In general, photonic crystals have a photonic band gap. That is the range of frequencies in which light cannot propagate through the structure.

1.2 History of photonic crystals

Artifical structures with the optical equivalent to the energy gap in semiconductors promise a wealth of new devices that could satisfy the demand for ever faster computers and optical communications. Since 1970, the number of electronic components that can be fitted onto a microchip has doubled every 18 months, allowing computers to double in speed, or half in price, during the same period. Although this trend – which was predicted by Gordon Moore of Intel in the 1960s - may continue for the next few years, the top speed at which integrated circuits can operate is starting to level out. In reality, with our current understanding of semiconductor technology, it seems to be difficult even to produce a 10 GHz personal computer. However, by transmitting signals with light rather than electrons, it might be possible to build a computer that operates at hundreds of terahertz (10^{12} Hz). It’s now believed by the researchers that such an awesome processing engine could be built from optical components made from so-called photonic crystals and quasi-crystals. These materials have highly periodic structures that can be designed to control and manipulate the propagation of light.

Electromagnetic wave propagation in periodic media was first studied by Lord Rayleigh in 1888 [Ray1888]. These structures were one-dimensional photonic crystals which have a narrow band gap prohibiting light propagation through the planes. About 100 years later, in 1987, Yablonovitch and John - by using the tools of classical electromagnetism and solid-state physics - introduced the concepts of omnidirectional photonic band gaps in two and three dimensions [Yab87, Joh87]. From then, the name "photonic crystal" was created and led to many subsequent developments in their fabrication, theory, and application.

A few years later in 1991, Yablonovitch and co-workers produced the first photonic crystal by mechanically drilling holes a millimeter in diameter into a block of material with a refractive index of 3.6 [YGL91]. That material known as "Yablonovit" prevented microwaves from propagating in any direction so that a 3D photonic bandgap existed. Other structures, which have bandgaps at microwave and radio frequencies, are being used to make e.g antennas that direct radiation away from the heads of mobile phone users.

About a decade later on, one has successfully fabricated photonic crystals that work in the near-infrared (780-3000 nm) and in the visible (450-750 nm) regions of the spectrum.

1.3 Photonic crystal devices state of the art and future aspects

A photonic crystal gives us new tools for the manipulation of photons and thus has received great interests in a variety of fields.

There are numerous applications, including sub-wavelength imaging, scanning photon tunneling microscopy, and devices such as ultrahigh-sensitivity phase shifters and optical switches.

Bandgap or defect engineering is one of the design criteria of photonic crystals. To control light in various ways, one introduces into the crystal an artificial disturbance, or "defect". By introducing line-shaped defects, it is possible to form an ultra-small waveguide that permits the transmission of light only along the defects [MCKFVJ96, CON02, NYSTTY01, SAN04]. To form a photonic nanocavity, one introduces into the crystal point defects so that light can be trapped [TAAN04, CMIN01]. By combining these line and point defects, it is possible to form ultra-small photonic circuits with various functions [AASN03, TSAN06, OKN03]. Moreover, the bandgap itself makes it possible to suppress spontaneous emission, which is a fundamental factor limiting the performance of various photonic devices.

In a photonic crystal, one can also engineer the band edge [CBB05, SMSOON05], where the group velocity of light becomes zero. At the band edge, light propagating in various directions is combined by Bragg reflection to form a standing wave. By using this standing wave as a cavity mode, for example, a laser that enables coherent oscillation over a large 2D area can be realized. Therefore, the use of various types of novel nonlinear optical phenomena might also be possible.

The other kind of engineering in photonic crystals is band engineering which focuses on the transmission bands that allow the propagation of light. By manipulating the dispersion relation obtained from the band structure, one can control the light in many ways. It is suggested that by considerably slowing the propagation speed and by altering the propagation direction of the light in a photonic crystal, or by making negative refraction possible, a variety of novel application and photonic devices will be developed for imaging.

It is expected that, over the next several years, nanoprocessing technology will quickly advance and that more reliable and precise devices will continue to be developed. In 2D photonic crystal slabs, there is promise of remarkable advance in Si-based systems, in addition to progress in integration with electronic circuits. Moreover, significant advances in combined optical and electronic circuits equipped with features such as optical switching, tuning, and delay functionality can be predicted.

The size and power consumption of such devices are expected to be many times smaller than they are now. There is no doubt that there are advances in a large number of applications, such as developments in next-generation miniaturized multiple-wavelength light sources [KK99, BN02] based on the addition of active functionality, supersensitive sensors [RTLPSHS04], optical memory functions that require a high Q-value [AASN05] and single-photon light sources [GMSEMFDPLAW07].

People hoped that, band-edge lasers [YSN04, CBB05, SMSOON05] will enable surface emission over a large area with a single wavelength, single light polarization, and single spot, and that by controlling the photonic crystal structure, the beam pattern will also be fully controllable. In the future, band-edge lasers will be applied to a wide range of fields, including information processing, communications and bio-related fields. It is believed that progress in integrating photonic crystals with organic electroluminescent and blue LED devices will also be made and that important advances will occur in highly efficient organic light-emitting diodes and display technology [FUIANOTNS04].

Technology available for the fabrication of 3D photonic crystals, which are considered to be more difficult to fabricate than 2D photonic crystals at the present time, is expected to advance over the coming decade and that 3D crystals will allow completely new levels of light control over three dimensions instead of two dimensions as in most of the present cases.

Photonic crystals are expected to be used in novel optical devices such as thresholdless laser diodes [NKB07], single mode light emitting diodes [Yab87], small waveguides with low loss sharp bends [MCKFVJ96, SHE03, MJFVHJ99, EAPSO01, JFVJ99], small prisms [KKTNTSK98], and small optical integrated circuits [NTYC00]. They can even be operated as "left handed materials" which are capable of focusing a transmitted waves into a sub-wavelength spot due to negative refraction.

The traditional limitation on lens focussing performance can also be broken through by photonic crystals. For the focussing of near field components, this is due to the restoration of the evanescent field components [LJJP03].

Photonic crystals can give the promise of flexibility on control over photons. We have far more control over the properties of photonic crystals than we do over the electronic properties of semiconductors. Photonic crystals could play a great role in the 21st century, particularly in the optical communications industry. Photonic crystals could address many of the problems that currently limit the speed and capacity of optical communication networks. For example, photonic crystals could be used to create novel LEDs and lasers that emit light in a very narrow wavelength range, together with highly selective optical filters that could be integrated on a chip [TAAN04].

One can use photonic crystals to design a mirror that reflects a selected wavelength of light from any angle with high efficiency. Moreover, they could be integrated within the photoemissive layer to create a LED that emits light at a specific wavelength and direction [DKSCJLKL03].

In addition, photonic crystals built from photoemissive materials, such as III-V semiconductors and glasses doped with rare-earth atoms, can also be used to make narrow linewidth lasers that could potentially be integrated with other components in an optical communication systems. The lasers are made by introducing a small number of holes that are slightly smaller or larger than the other holes in the photonic crystal lattice. These "microcavities" generate a narrow so-called defect mode within the photonic bandgap. Photonic crystal microcavities that are fabricated from passive materials, such as silicon dioxide and silicon nitride, could also be used to create filters that only transmit a very narrow range of wavelengths. Such filters could be used to select a wavelength channel in a DWDM communication system. Indeed, arrays of these devices could be integrated onto a chip to form the basic of a channel demultiplexer that separates and sorts light pulses of different wavelengths.

Materials with photonic band gaps could speed up the Internet by improving the transmission of long distance optical signals. Conventional optical fibers have one drawback that different wavelengths of light can travel through the material at different speed. Due to chromatic dispersion, a pulse of light traveling through such a fiber broadens out, thereby limiting the amount of data that can be sent. These problems could be solved by an extremely unusual "holey fiber" developed by Philip Russell and Jonathan Knight of the University of Bath and co-workers [KBR01]. The fiber has a regular lattice of air holes running along its length and transmits a wide range of wavelengths without suffering from dispersion. It's made by packing a series of hollow glass capillary tubes around a solid glass core that run through the center. This structure is then heated and stretched to create a long fiber that is only a few microns in diameter. The fiber can also have the unusual property that is transmits only a single mode of light, even if the diameter of the core is very large.

1.4 Goal and structure of the thesis

The goals of this thesis are to design photonic crystal structures to be used in optical communications and optical imaging:

- Photonic crystal structures for potential dispersion management in optical telecommunication systems

- 2D non-uniform photonic crystal waveguides based on a square lattice for wide-angle beam refocusing using negative refraction

- 2D non-uniform photonic crystal slabs using a triangular lattice for all-angle beam refocusing

- Compact band-pass transmission filter based on phase-shifted photonic crystals

Corresponding to the above goals, the thesis consists of 8 chapters:

A general introduction such as definition, history and future aspects of of photonic crystals is discussed in Chapter 1. Chapter 2 presents Maxwell's equations in periodic media, the modelling of wave propagation in photonic crystals by Bloch waves and Brillouin zones.

The wave-vector diagram of photonic crystals is showed in Chapter 3. Here the calculation model of wave-vector diagram for square and triangular photonic crystal structures is discussed.

In Chapter 4 some important characteristics of photonic crystals are investigated: photonic bandgap, negative refraction, imaging and sub-wavelength imaging. In Chapter 5, photonic crystal structures for potential dispersion management in optical telecommunication systems are presented.

Two-dimensional square non-uniform photonic crystal waveguides for wide-angle beam refocusing using negative refraction are discussed in Chapter 6. Chapter 7 comprises 2D triangular non-uniform photonic crystal slabs for all-angle beam refocusing. A compact phase-shifted band-pass transmission filter based on photonic crystals is given in Chapter 8.

Finally, the thesis is summarized in Chapter 9.

Chapter 2

Maxwell’s equations in periodic media

2.1 Maxwell’s equations in periodic media

In 1928, Felix Bloch [Blo29] extended an 1883 theorem in one dimension by G. Floquet [Flo1883] and studied the wave propagation in three dimensional periodic media. Bloch proved that waves in such a medium can propagate without scattering and their behavior is governed by a periodic envelope function multiplied by a function representing a plane wave. Maxwell’s equation can be written as the generalized eigenproblem in the magnetic field $\vec{H}$ with time dependence $e^{-i\omega t}$ in a source-free linear periodic dielectric with the dielectric function $\varepsilon(x,y,z)$ and c is the speed of light [JISWJF02, JJ03]:

$$\vec{\nabla}\times\frac{1}{\varepsilon}\vec{\nabla}\times\vec{H}=\left(\frac{\omega}{c}\right)^{2}\vec{H}\cdot \qquad (2.1)$$

This is an eigenvalue equation, with eigenvalue $(\omega/c)^2$ and eigen-operator $\vec{\nabla}\times\frac{1}{\varepsilon}\vec{\nabla}\times$ that is Hermitian under the inner product $\int\overrightarrow{F*}\cdot\vec{G}$ between the two arbitrary fields $\vec{F}$ and $\vec{G}$. (The two curls correspond roughly to the "kinetic energy" and $1/\varepsilon$ to the "potential" compared to the Schroedinger Hamiltonian ∇^2+V).

It is sometimes more convenient to write a generalized Hermitian eigenproblem in the electric field $\vec{E}$:

$$\vec{\nabla} \times \vec{\nabla} \times \vec{E} = \left(\frac{\omega}{c}\right)^2 \varepsilon \vec{E} \tag{2.2}$$

which separates the kinetic and potential terms.

2.2 Modeling of wave propagation in photonic crystals

The spacing between the air holes in a photonic crystal structure with air holes embedded in dielectric material (or the lattice size) is given roughly by the wavelength of the light divided by the refractive index of the dielectric material. The problem in making these small structures is enhanced because it is more favorable for a photonic band gap to form in dielectrics with a high refractive index, which reduces the size of the lattice spacing even further. Let’s suppose that we want to create a photonic crystal which could trap near infrared light with a wavelength of 1µm in a material with a refractive index of 3.0. We would have to create a structure in which the air holes were separated by about 0.3 µm, which is an extremely difficult task. If the scale was 1000 times smaller, we could build the structure atom-by-atom using a chemical reaction, and if it was 1000 times larger we were able to build the structure mechanically, as Yablonovitch and co-workers did [YGL91]. To be able to create photonic crystals for optical devices, we need to use state-of-the-art semiconductor micro-fabrication techniques which require high production costs and investment. Because of this, computer modeling of prospective photonic crystal structures is also a very important area of research, as it may prevent expensive fabrication errors later. There are typically three types of computational methods: time-domain "numerical experiments" [CDYSHS94, CLH95, FVJ96, SS97, AWP99, WP00] that model the time-evolution of the fields with arbitrary starting conditions in a discretized system (e.g. using finite differences); definite-frequency transfer matrices [PM92, BPMW95, ET96, CBMR97] wherein the scattering matrices are computed to extract transmission/reflection through the structure; and frequency-domain methods [JJ01] to directly extract the Bloch fields and frequencies by diagonalizing the eigenoperator. The first two categories intuitively correspond to directly measurable quantities such as transmission, whereas the third is more abstract, yielding the band diagrams that provides a guide to interpretation of measurements as well as a starting-point for device design and semi-analytical methods.

Maxwell’s equations can be solved numerically either in the time domain or in the frequency domain. Each method has its strong points and its disadvantages. The frequency domain method, which assumes that the time dependence is harmonic, plays an important role in calculating the eigenstates and band structures. On the other hand, the time domain method, which solves the time dependent Maxwell equations directly on spatial grids, is well suited for computing problems that involve the evolution of electromagnetic fields and for systems containing complex materials.

The computational method we used to simulate photonic crystal structures is the time-domain method. The simulation is based on the well known finite-difference time-domain (FDTD) technique. The FDTD method is a rigorous solution to Maxwell’s equation and does not have any approximations or theoretical restrictions. This method is widely used as a propagation solution technique in integrated optics. FDTD is a direct solution of Maxwell’s curl equations and therefore includes many more effects than a solution of the monochromatic wave equation.

Now we consider the FDTD algorithm. Imagine a region of space which contains no flowing currents or space charges. Maxwell’s curl equations can be written in Cartesian coordinates as six simple scalar equations. Two examples are:

$$\frac{\partial Hx}{\partial t} = \frac{-1}{\mu}\left(\frac{\partial Ey}{\partial z} - \frac{\partial Ez}{\partial y}\right). \tag{2.3}$$

$$\frac{\partial Ey}{\partial t} = \frac{-1}{\varepsilon}\left(\frac{\partial Hx}{\partial z} - \frac{\partial Hz}{\partial x}\right). \tag{2.4}$$

The other four equations are symmetric equivalents of the above and are obtained by cyclically exchanging the *x*, *y*, and *z* subscripts and derivatives.

Maxwell's equations describe a situation in which the temporal change in the E-field is dependent upon the spatial variation of the H field, and vice versa. The FDTD method solves Maxwell's equations by first discretizing the equations via central differences in time and space and then numerically solving these equations in software. The most common method to solve these equations is based on Yee's mesh and computes the E- and H-field components at points on a grid with grid points spaced Δx, Δy, and Δz apart. The E- and H-field components are then interlaced in all three spatial dimensions as shown in Figure 2.1 [Yee96]

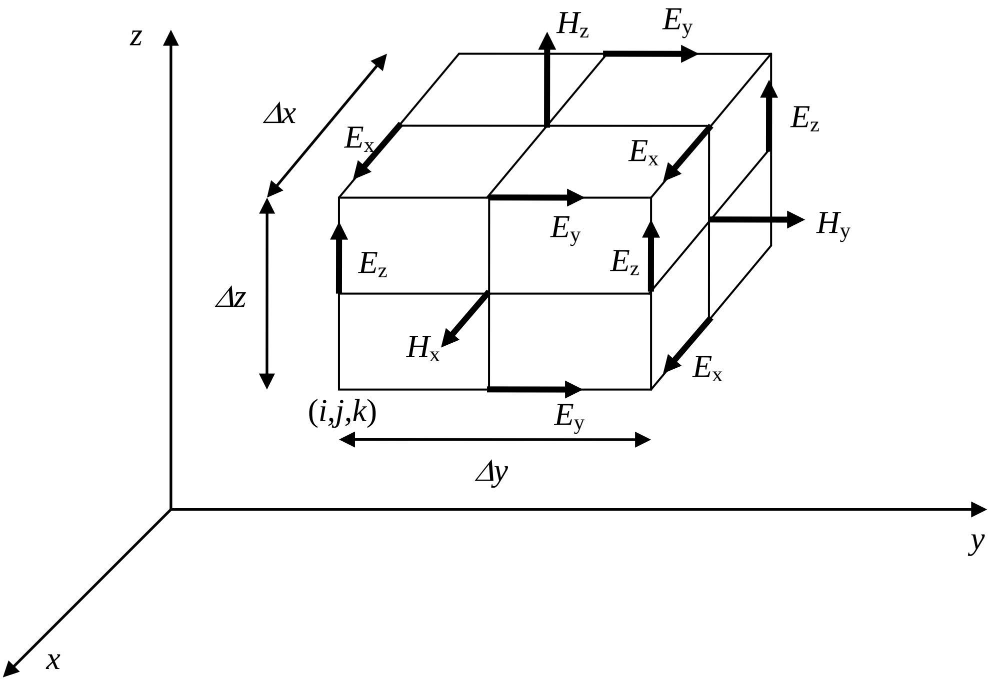

Fig. 2.1. In a Yee cell of dimension *Ax*, *Ay*, *Az*, note how the H-field is computed at points shifted one-half grid spacing from the E-field grid points [Yee96].

Furthermore, time is broken up into discrete steps of Δt. The E-field components are then computed at time $t=n\Delta t$ and the H-field at times $t = (n+1/2)\Delta t$, where *n* is an integer representing the compute step. For instance, the E-field at a time $t = n\Delta t$ is equal to the E-field at $t = (n-1)\Delta t$ plus an additional term computed from the spatial variation, or curl, of the H-field at time t.

This method results in six equations that can be used to compute the field at a given mesh point, denoted by integers i, j, k. For example, two of the six are:

$$H_{x(i,j,k)}^{n+\frac{1}{2}} = H_{x(i,j,k)}^{n-\frac{1}{2}} + \frac{\Delta t}{\mu \Delta z}\left(E_{y(i,j,k)}^{n} - E_{y(i,j,k-1)}^{n}\right) - \frac{\Delta t}{\mu \Delta y}\left(E_{z(i,j,k)}^{n} - E_{z(i,j-1,k)}^{n}\right). \tag{2.5}$$

$$E_{x(i,j,k)}^{n+1} = E_{x(i,j,k)}^{n} + \frac{\Delta t}{\varepsilon \Delta y}\left(H_{z(i,j+1,k)}^{n+\frac{1}{2}} - H_{z(i,j,k)}^{n+\frac{1}{2}}\right) - \frac{\Delta t}{\varepsilon \Delta z}\left(H_{y(i,j,k+1)}^{n+\frac{1}{2}} - H_{y(i,j,k)}^{n+\frac{1}{2}}\right). \tag{2.6}$$

These equations are iteratively solved in a leapfrog manner, alternating between computing the E and H-fields at subsequent $\Delta t/2$ intervals.

2.3 Bloch waves and Brillouin zones

A photonic crystal corresponds to a periodic dielectric material, represented by the function $\varepsilon(\vec{x}) = \varepsilon(\vec{x} + \vec{R}_i)$ for some primitive lattice vectors $\vec{R}_i$ (i = 1,2,3 for a crystal periodic in all three dimensions). In this case, the Bloch-Floquet theorem for periodic eigenproblems states that the solutions to equation

$$\vec{\nabla} \times \frac{1}{\varepsilon} \vec{\nabla} \times \vec{H} = \left(\frac{\omega}{c}\right)^2 \vec{H} \tag{2.7}$$

can be chosen of the form [JJ03]

$$\vec{H}(\vec{x}) = e^{i\vec{k}\vec{x}}\vec{H}_{n,\vec{k}}(\vec{x}) \cdot \tag{2.8}$$

With eigenvalue $\omega_n(\vec{k})$, where $\vec{H}_{n,\vec{k}}$ is a periodic envelope function satisfying

$$(\vec{\nabla} + i\vec{k}) \times \frac{1}{\varepsilon}(\vec{\nabla} + i\vec{k}) \times \vec{H}_{n,\vec{k}} = \left(\frac{\omega_n(\vec{k})}{c}\right)^2 \vec{H}_{n,\vec{k}} \cdot \tag{2.9}$$

This equation is a Hermitian eigenproblem over the primitive cell of the lattice at each Bloch wave vector $\vec{k}$. The primitive cell is a finite domain if the structure is periodic in all directions, leading to discrete eigenvalues labeled by n = 1,2,…These eigenvalues $\omega_n(\vec{k})$ are a continuous functions of $\vec{k}$, forming discrete "bands", in a "band structure" or forming a dispersion diagram. These representations map out all possible electromagnetic interactions in the system. Here $\vec{k}$ is not required to be real. A complex $\vec{k}$ gives evanescent modes that can exponentially decay from the boundaries of a finite crystal.

In addition, the eigensolutions are also periodic functions of $\vec{k}$ that means the solution at $\vec{k}$ is the same as the solution at $\vec{k} + \vec{G}_j$, where $\vec{G}_j$ is a primitive reciprocal lattice vector defined by $\vec{R}_i \cdot \vec{G}_j = 2\pi\delta_{ij}$. Due to this periodicity, one needs only to compute the eigensolutions for $\vec{k}$ within the primitive cell of this reciprocal lattice – or, more conventionally, one considers the set of inequivalent wavevectors closest to the $\vec{k}$ = 0 origin, a region called the first Brillouin zone. For example, in a one-dimensional system, where $R_1 = a$ for some periodicity a and $G_1 = 2\pi/a$, the first Brillouin zone is the region $k = -\pi/a \ldots \pi/a$; all other wavevectors are equivalent under translation by a multiple of G_1. Moreover, the first Brillouin zone may itself be redundant if the crystal features additional symmetries such as mirror planes. By eliminating these redundant regions, one obtains the irreducible Brillouin zone. In the preceding one-dimensional example, since most systems will have time-reversal symmetry, the irreducible Brillouin zone would be $k = 0 \ldots \pi/a$.

In case of uniform waveguides, the dispersion relations arise as a special case of the Bloch formalism: The Brillouin zone of the wavevector $\vec{k}$ (also called β) is unbounded, and the envelope function $\vec{H}_{n,k}$ is a function only of the transverse coordinates.

Chapter 3

Wave-vector diagram

In conventional geometric optics, light propagation and energy flow in a dielectric material is described by the phase refractive index and Snell’s law. Other way, energy flow in a periodic structure, such as photonic crystals, is different from that in conventional materials. The direction of light propagation inside a photonic crystal is determined by the equi-frequency surface or wave-vector diagram. The wave-vector diagram describes the loci of all relevant wave vectors at a fixed wavelength. In principle, they show how the effective index of the structure depends on the direction of propagation.

3.1 Wave propagation in two–dimensional photonic crystals

A two-dimensional photonic crystal is periodic along two directions in the x-y plane and homogeneous in the z direction. We consider the square or triangular lattice of dielectric columns with circular cross section in air (see Figure 3.1). Only in-plane propagation is considered.

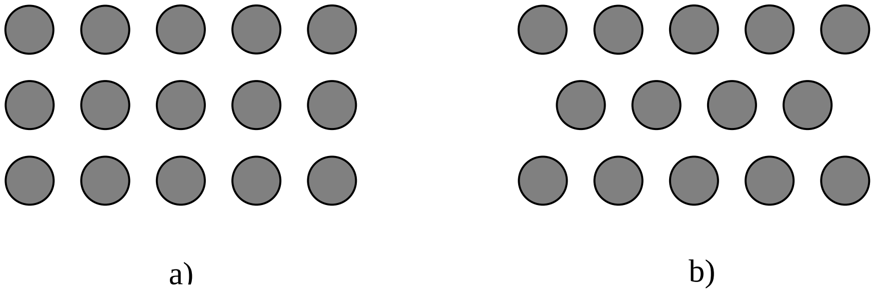

Fig. 3.1. A two-dimensional photonic crystal consisting of dielectric columns with circular cross-section in air. These are cuts in the x-y plane for a) square lattice b) triangular lattice.

The wave equations for the z components of the field are:

For TM modes:

$$\frac{\partial^2 E_z}{\partial x^2} + \frac{\partial^2 E_z}{\partial y^2} + k^2 n^2(x,y) E_z = 0 \tag{3.1}$$

For TE modes:

$$\frac{\partial}{\partial x}\left(n^{-2}(x,y) \frac{\partial H_z}{\partial x} \right) + \frac{\partial}{\partial y}\left(n^{-2}(x,y) \frac{\partial H_z}{\partial y} \right) + k^2 H_z = 0 \tag{3.2}$$

with the wave number $k = 2\pi/\lambda$.

For the field pattern, we take the Floquet-Bloch expansion for E_z (or H_z):

$$E_z = e^{i\vec{\beta}.\vec{r}} \sum_{m=-\infty}^{+\infty} \sum_{n=-\infty}^{+\infty} c_{m,n} e^{i\left(m\vec{b}_1 + n\vec{b}_2\right).\vec{r}} \tag{3.3}$$

With $\vec{r} = (x, y)$, $\vec{\beta} = \left(\beta_x, \beta_y\right)$ and the reciprocal lattice vectors $\vec{b}_1, \vec{b}_2$.

An analogous plane wave expansion for the periodic refractive index distribution

$$n^{\pm 2}(x, y) = \sum_{m=-\infty}^{+\infty} \sum_{n=-\infty}^{+\infty} f_{m,n} e^{i\left(m\vec{b}_1 + n\vec{b}_2\right).\vec{r}} \tag{3.4}$$

can be calculated analytically. In doing this, n_0 and n_1 denote the refractive indices of air and the columns, respectively, *r* is the radius of the columns, *a* is the lattice constant and $\Omega = \frac{2\pi}{a}$.

For the square lattice we have $\vec{b}_1 = \Omega\vec{e}_x, \vec{b}_2 = \Omega\vec{e}_y$ and obtain

$$f_{0,0} = n_0^2 + \left(n_1^2 - n_0^2\right)\pi\left(\frac{r}{a}\right)^2 \tag{3.5}$$

$$f_{m,n} = \frac{n_1^2 - n_0^2}{\sqrt{m^2 + n^2}} \cdot \frac{r}{a} \cdot J_1\left(2\pi\sqrt{m^2 + n^2}\,\frac{r}{a}\right) \cdot \tag{3.6}$$

For the triangular lattice $\vec{b}_{1,2} = \Omega\left(\vec{e}_x \pm \frac{1}{3}\vec{e}_y\right)$ and we get

$$f_{0,0} = n_0^2 + \left(n_1^2 - n_0^2\right)\frac{2\pi}{\sqrt{3}}\left(\frac{r}{a}\right)^2 \tag{3.7}$$

$$f_{m,n} = \frac{2}{\sqrt{3}}\frac{n_1^2 - n_0^2}{\sqrt{(m+n)^2 + \frac{1}{3}(m-n)^2}} \cdot \frac{r}{a} \cdot J_1\left(2\pi\sqrt{(m+n)^2 + \frac{1}{3}(m-n)^2}\,\frac{r}{a}\right) \cdot \tag{3.8}$$

These above formulas hold for the case of TM modes. For TE modes, one needs only to replace the refractive indices in them by their reciprocal values.

3.2 Eigenvalue equations

Consider the TM modes of a **square** lattice. Inserting the expansion (3.3) and (3.4) into equation (3.1), one gets after lengthy algebra the equation [Lem02]:

$$\begin{gathered}\left[(\beta_x + m\Omega)^2 + \left(\beta_y + n\Omega\right)^2\right] \cdot c_{m,n} = k^2 \sum_i \sum_j f_{m-i,n-j} c_{i,j} \\ m,n = \ldots -2,-1,0,1,2,\ldots\end{gathered} \tag{3.9}$$

$c_{i,j}$ will be defined later on.

This equation can be processed in two different ways. In band structure calculations, we take a particular normalized vector $\vec{k} = \left(k_x, k_y\right) = \left(\frac{\beta_x}{\Omega}, \frac{\beta_y}{\Omega}\right)$ and get from equation (3.9) the equation:

$$\left[(k_x+m)^2+(k_y+n)^2\right]\cdot c_{m,n}=\left(\frac{\omega a}{2\pi c}\right)^2\sum_i\sum_j f_{m-i,n-j}c_{i,j}\,. \tag{3.10}$$

This is a generalized symmetric eigenvalue problem for the dimensionless frequency. If this eigenvalue calculation is performed for all values of $\vec{k}$ in the first Brillouin zone, we get the well-known band structure diagrams.

In wave-vector diagram calculations, we take at a chosen fixed wavelength λ (or frequency ω) a particular direction of the vector $\vec{\beta}$, characterized by an angle φ with respect to the x-axis. It is $\beta_x=\left|\vec{\beta}\right|\cos\varphi,\beta_y=\left|\vec{\beta}\right|\sin\varphi$, and with the normalized parameters $\Lambda=\frac{\left|\vec{\beta}\right|}{k},q=\frac{\lambda}{a}$, we get from equation (3.9):

$$\left[\Lambda^2+2\Lambda(m\cos\varphi+n\sin\varphi)q+\left(m^2+n^2\right)q^2\right]c_{m,n}=\sum_i\sum_j f_{m-i,n-j}c_{i,j}\,. \tag{3.11}$$

This is a quadratic eigenvalue problem for Λ, the normalized length of the vector $\vec{\beta}$. If this eigenvalue calculation is performed for all directions φ and we plot in polar coordinates $\rho=\left|\vec{\beta}\right|(\varphi)$, we get the wave-vector diagram at the wavelength λ.

The quadratic eigenvalue equation (3.11) holds for TM modes of a **square** lattice. The other cases have been treated analogously with the following results:

TE modes of **square** lattice:

$$c_{m,n}=\sum_i\sum_j\left\{\Lambda^2+\Lambda[(m+i)\cos\varphi+(n+j)\sin\varphi]\cdot q+(m.i+n.j)\cdot q^2\right\}\cdot f_{m-i,n-j}c_{i,j}\,. \tag{3.12}$$

TM modes of **triangular** lattice:

$$\begin{aligned}&\left\{\Lambda^2+2\Lambda\left[(m+n)\cos\varphi+(m-n)\sin\varphi/\sqrt{3}\right]\cdot q+\left[(m+n)^2+(m-n)^2/3\right]\cdot q^2\right\}\cdot c_{m,n}\\&=\sum_i\sum_j f_{m-i,n-j}c_{i,j}\,.\end{aligned}\tag{3.13}$$

TE modes of **triangular** lattice:

$$c_{m,n}=\sum_i\sum_j\left\{\begin{array}{l}\Lambda^2+\Lambda\left[(m+n+i+j)\cos\varphi+(m-n+i-j)\sin\varphi/\sqrt{3}\right]\cdot q\\+\left[(m+n)(i+j)+(m-n)(i-j)/3\right]\cdot q^2\end{array}\right\}f_{m-i,n-j}c_{i,j}\,.\tag{3.14}$$

3.3 Calculation of wave-vector diagrams

By using the expansion of Guenther (Guenther 1876 [Gün1876]; W. H. Press et al.1992 [PTVF92]), the equations (3.11) to (3.14) can be turned into linear problems. The quadratic eigenvalue problems $\left(\Lambda^2\hat{A}+\Lambda\hat{B}+\hat{C}\right)\vec{x}=0$, where $\hat{A},\hat{B},\hat{C}$ are $n\times n$ matrices, is equivalent to introducing an additional unknown vector $\vec{y}$ and solving the $2n\times 2n$ generalized linear eigenvalue problem $\begin{pmatrix}\hat{O} & \hat{I}\\ -\hat{C} & -\hat{B}\end{pmatrix}\cdot\begin{pmatrix}\vec{x}\\ \vec{y}\end{pmatrix}=\Lambda\begin{pmatrix}\hat{I} & \hat{O}\\ \hat{O} & \hat{A}\end{pmatrix}\cdot\begin{pmatrix}\vec{x}\\ \vec{y}\end{pmatrix}$. The Guenther expansion has two disadvantages: the resulting linear eigenvalue problem is non-symmetric (hence pairs of complex conjugated eigenvalues appear) and its size doubles.

To solve numerically the eigenvalue problems in (3.11) to (3.14), which are infinite-dimensional, these equations must be truncated. If we take M plane waves in the expansions (3.4) (3.5) and (3.6) along each reciprocal lattice vector direction, we get finally non-symmetric $L\times L$ matrices with a size $L = 2(2M+1)^2$. In order to calculate the eigenvalues, for convenience's sake standard routines from the NAG Fortran Library were used.

Large discontinuities in the refractive index distribution at the boundaries between the dielectric columns and air may cause poor convergence of the plane wave expansion and the use of appropriate smoothing methods can accelerate the convergence (e.g. Meade et al. 1993 [MRBJA93]; Johnson and Joannopoulos 2001 [JJ01]).

Chapter 4

Characteristics of photonic crystals

4.1 Photonic bandgap

A photonic bandgap is the range of frequencies where the light cannot propagate through the structure.

To understand the behavior of light in a photonic crystal, one should compare it to the movement of electrons and holes in a semiconductor. In a silicon crystal, the atoms are arranged in a diamond-lattice structure, and electrons moving through this lattice experience a periodic potential as they interact with the silicon nuclei via the Coulomb force. This interaction results in the formation of allowed and forbidden energy levels. However, for real materials, electrons can have an energy within the forbidden band if the periodicity of the lattice is broken by a missing silicon atom or by an impurity atom occupying a silicon site, or if the material contains interstitial impurities (additional atoms located at non-lattice sites).

Now we consider photons moving through a block of transparent dielectric material that contains a number of tiny air holes arranged in a lattice pattern. The photons will pass through regions of high refractive index – the dielectric – interspersed with regions of low refractive index – the air holes. To a photon, this contrast in refractive index looks just like the periodic potential that an electron experiences traveling through a silicon crystal. Indeed, if there is large contrast in refractive index between the two regions then most of the light will be confined either within the dielectric material or the air holes. This confinement results in the formation of allowed energy regions separated by a forbidden region – the so-called photonic bandgap. Under certain conditions, the patterned dielectric material will block light with wavelengths in the photonic bandgap, while allowing other wavelengths to pass freely.

It is possible to create energy levels in the photonic bandgap by introducing a special form of doping the photonic crystals by changing the size of a few of air holes in the material. This is the photonic equivalent to breaking the perfect periodicity of the silicon-crystal lattice. In the photonic case, the diameter of the air holes and the contrast in refractive index throughout the material are critical parameters.

Photonic bandgap structures can also be made from a lattice of high-refractive-index material embedded within a medium with a lower refractive index. An example of such material is opal. However, the contrast in the refractive index in opal is rather small which results in a rather small band gap.

4.2 Imaging

Free-space optical switching is sometimes referred to as imaging optical switching, because most proposed systems use imaging operations to control the divergence of the optical signals and concentrate the optical power. Even the relatively well-behaved optical output of a laser diverges as a Gaussian beam [Zen05]

$$\theta_d = \frac{2\lambda}{\pi d_0} \tag{4.1}$$

where θ_d is the full divergence angle,

λ is the laser wavelength, and

d_0 is the diameter of the Gaussian beam waist at its $1/e^2$ intensity points.

Since laser thresholds may be lowered by minimizing their active volumes, we may expect that the output beam waist of a transmitter will continue to be only a few micrometers in size.

The imaging systems must have the following characteristics:

- High resolution: to collect all of the light from small sources or modulators and concentrate the signal energy onto small detectors.

- Isoplanaticism, so that the size, shape, and energy content of the signal spots do not change significantly across the array of devices. This implies an optical system with very little aberration and with minimal vignetting of the signal beams, which might cause energy difference between them.

- Low loss since power loss will affect system speed and tolerances

4.3 Negative refraction

One of the most fundamental phenomena in optics is refraction: when a beam of light crosses the interface between two different materials, its path is altered depending on the difference in the refractive indices of the materials. Refraction is the basic principle behind lenses and other optical elements that focus, guide or otherwise manipulate light. Highly sophisticated and complex optical devices are developed by carefully shaping materials so that light is refracted in desired ways.

The principle of refraction can be applied to all electromagnetic waves not just visible light. Every material, including air, has an index of refraction (or refractive index):

$$\frac{c_{med}}{c_0} = \frac{1}{n_{med}}. \tag{4.2}$$

When an electromagnetic wave traverses the interface from a material with refractive index n_1 to another material with refractive index n_2, the change in the direction of its trajectory can be determined from the ratio of refractive indices n_2/n_1 by the use of Snell's Law

$$n_1 \sin\theta_1 = n_2 \sin\theta_2 \cdot \tag{4.3}$$

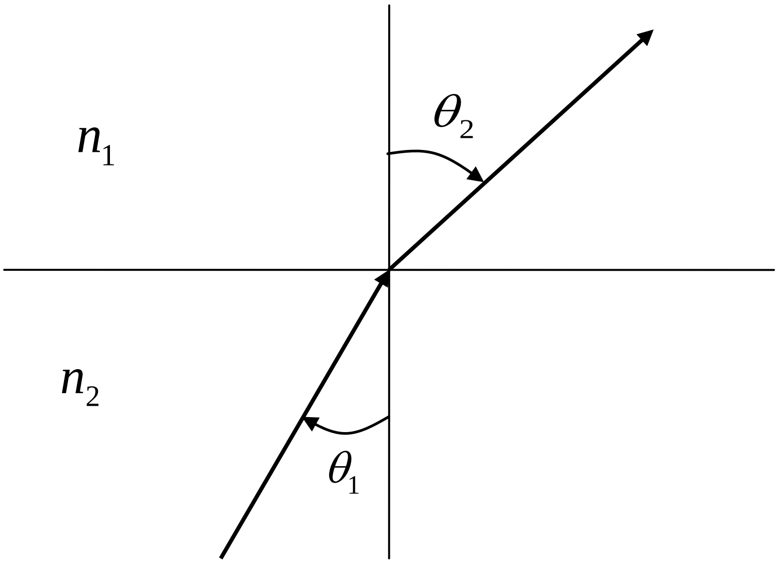

Fig. 4.1. Principle of refraction by Snell's law.

To apply Snell's Law, consider an interface between two materials and an imaginary line that runs perpendicular to the interface (the surface normal). The angles in Snell's Law are measured with respect to the surface normal.

For all known naturally occurring materials, the refractive index takes only positive values. In 1968, Veselago published a theoretical analysis of the electromagnetic properties of materials with simultaneous negative permittivity and negative permeability [Ves68]. Maxwell's equation relates the permittivity and the permeability to the refractive index as follows:

$$n = \pm\sqrt{\varepsilon\mu}\cdot \tag{4.4}$$

The sign of the index is usually taken as positive. However, Veselago showed that if a medium has both negative permittivity and negative permeability, this convention must be reversed: we must choose the negative sign of the square root. That mean, as Veselago hypothesized, a material with a negative refractive index could exist without violating any of the laws of physics. He also predicted that this remarkable material would exhibit a wide variety of new optical phenomena.

When the refractive index is negative, the phase velocity – given by *c/n* – is negative and the wave travels backwards towards the source. The phase velocity determines the rate at which the peaks of a wave pass a given point in time. But this is not the most relevant definition of a wave’s velocity: we can also define the group, energy, signal and front velocities and these generally differ from the phase velocity.

When the refractive index of a material does not vary with the wavelength of light that travels through it, then all of the velocity definitions above are the same and we can intuitively use the index as a measure of the wave’s velocity. However, when a material is dispersive – has an index that varies with wavelength – then the various velocities are different. As Veselago showed, the phase and energy velocities are opposite in negative index materials.

Negative refraction of waves propagating from one medium to another is a phenomenon where the light is refracted in a way to propagate along the same side as the incident light with respect to the normal of the interface, contrary to the normal light refractions (see Fig. 4.2).

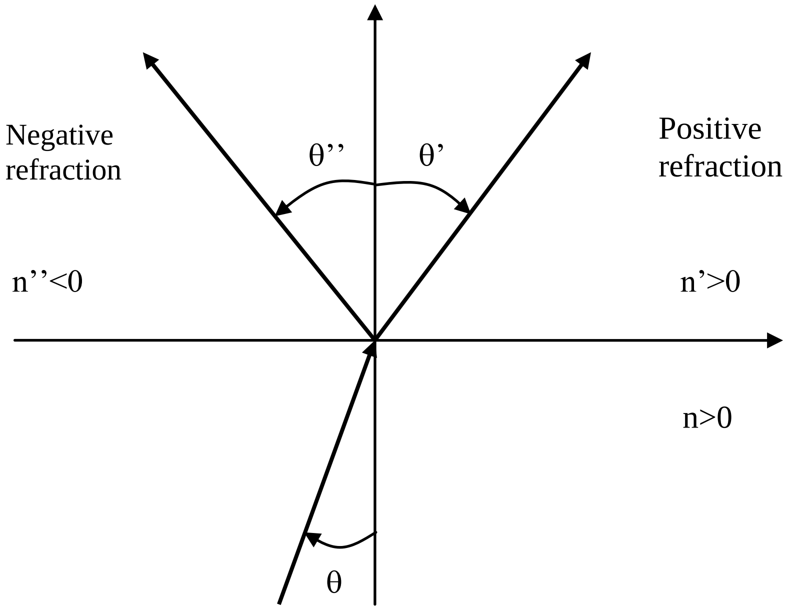

Fig. 4.2. Negative and positive refraction.

Negative refraction leads to a variety of interesting phenomena and potential applications. One of the most interesting applications is the superlens. Pendry suggested that a negative index material slab could make a superlens with a resolution far beyond the diffraction limit that is inherent in the conventional far-field lens [Pen00]. For the near-field case, a negative index material slab can amplify the evanescent wave components to form a high-resolution image.

A negative index of refraction would allow a flat slab of a material to behave as a lens. There are two types of negative refraction. The first type has simultaneous negative permittivity and negative permeability and the other type arises from beam steering phenomena in photonic crystals where we can get a negative refraction of the directions of the group velocities at the interfaces.

4.4 Sub-wavelength imaging

One of the interesting properties of negative index materials is their ability to focus light. Conventional lenses are convex and have a converging effect on light rays. The resolution of a conventional (convex) lens is always limited by the wavelength of the light. A light beam cannot be focused to a spot with a diameter smaller than about half of the wavelength of the light [Pen00]. In 1968, Veselago [Ves68] has shown theoretically that a convex lens made of a negative index material would lead to a divergent light, and that a concave lens made of negative index material would lead to a convergent light [Ves68]. This behavior is thus opposite to the behavior observed for conventional convex and concave lenses made of positive index materials. Veselago also noted that a flat plate of thickness T made of negative index material with n_1 = -1 and located in vacuum can focus radiation from a point source P positioned at a distance $D<T$ from one side of the plate to a point P’ located at a distance T-D from the other side of the plate (Fig. 4.3) [Ves68]. As can be seen from Fig. 4.3, also an image inside the slab is formed. When the source is closer to the slab, or the slab becomes thicker, the distance of the refocus will be increased. However, Veselago also remarked that the flat plate, unlike a conventional lens, will not focus at a point a beam of rays coming from infinity [Ves68].

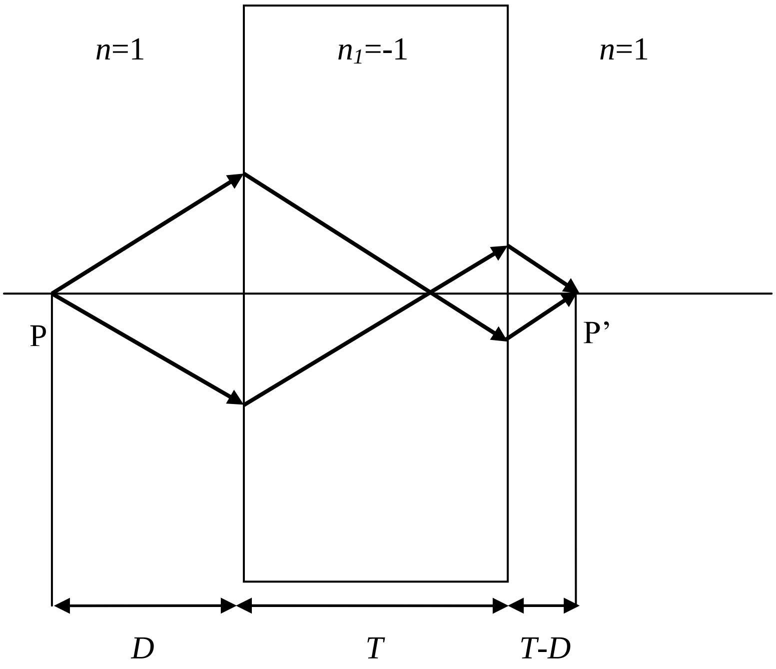

Fig. 4.3. Imaging by a flat slab of thickness *T* of negative index material with n_1 = -1 and surrounded by vacuum. A point source P is positioned at a distance D from the left surface of the slab. A "perfect" image of the source can be observed at the point P’, located at a distance *T-D* from the right surface of the slab.

In 1978, Silin showed that plane-parallel lenses can be constructed on the basis of media with negative dispersion [Sil78]. In 2000, Pendry pointed out that flat slabs of negative index material with *n* = -1 and surrounded by vacuum makes perfect lenses or superlenses since both propagating and evanescent waves contribute to the resolution of the image [Pen00]. These lenses are just predicted to have sub-wavelength resolution better than the diffraction limit.

Chapter 5

Photonic crystal structures for potential dispersion management in optical telecommunication systems

5.1 Introduction

For applications of photonic crystals in new or improved functional components used for communications, several unique properties which may be of special interest are investigated: spatial and chromatic dispersion as well as anomalous refraction phenomena. Photonic crystal structures can be used in two distinct ways: firstly the direct use of the photonic bandgap itself for example as filters or for suppression of unwanted spontaneous emission [Yab87]. The other way is to use the strong dispersion in the vicinity of an optical bandgap [Rus81] both in space or frequency domains. Especially the strong angular difference between phase and group velocity directions may be used in practical devices. This strongly frequency dependent beam-steering effect in periodic structures was demonstrated by Zengerle decades before [UZ80, Zen87, Zen79]. It may now be interesting for spatial optical frequency discrimination and thus also for dispersion compensation or pulse shaping. Photonic Crystal Fibers can reveal very strong unusual chromatic dispersion characteristics [RKR02], however, waveguiding is limited along the fiber axis alone. 2D-waveguide structures offer the ability to use both the spatial and chromatic dispersion characteristics. Thus by changing the geometry of wave propagation adaptive dispersion management may be possible.

5.2 Principle of operation

The principle for dispersion compensation here is based on the effect of beam-steering [MA70] which can be highly frequency-dependent in periodic waveguides. This effect including a frequency-dependent beam-steering angle after the transition from a smooth waveguide to a 1D or 2D periodically modulated waveguide was used for frequency filtering [ZL90] in applications e.g. as optical multiplexer or polarization beam splitter [Zen88].

A very convenient way to represent the most important basic waveguiding properties of these structures (described by Floquet-Bloch waves [Bri46]) is done in the wave vector space using the so-called wave vector diagrams (WVDs). In Fig. 5.1.a such a diagram is drawn in the vicinity of the optical band gap (or classically spoken for weak periodic modulation "in the regime of Bragg reflection"). One can see two cases: One at the beginning of the transition from a smooth waveguide (dashed small circles) to the photonic crystal area with the wavevector $\vec{\beta}_{0,u}$, and one for wave propagation in the grating itself with the wavevector $\vec{\beta}_{0,m}$. The direction of energy flow can be derived from the normal to the dispersion contours. Thus, if the grating area with two straight boundaries is embedded in between two smooth regions, an incident light beam (represented by the direction of energy flow) will - after passing the photonic crystal structure - be laterally shifted as shown in Fig. 5.1.b [Zen87]. For optical carrier frequencies in the vicinity of the bandgap (here slightly below the bandgap) this lateral beam-shift caused by beam steering is strongly frequency dependent as also shown in Fig. 5.1.b.

As the pathway of the energy flow in the periodic region varies with frequency and additionally there exists a strong group velocity dispersion near the photonic bandgap, these effects may also be used for dispersion "management" purposes. Such a proposal was presented in [KK99] for a doubly periodic structure. However, it exists also even for inclined singly periodic waveguides.

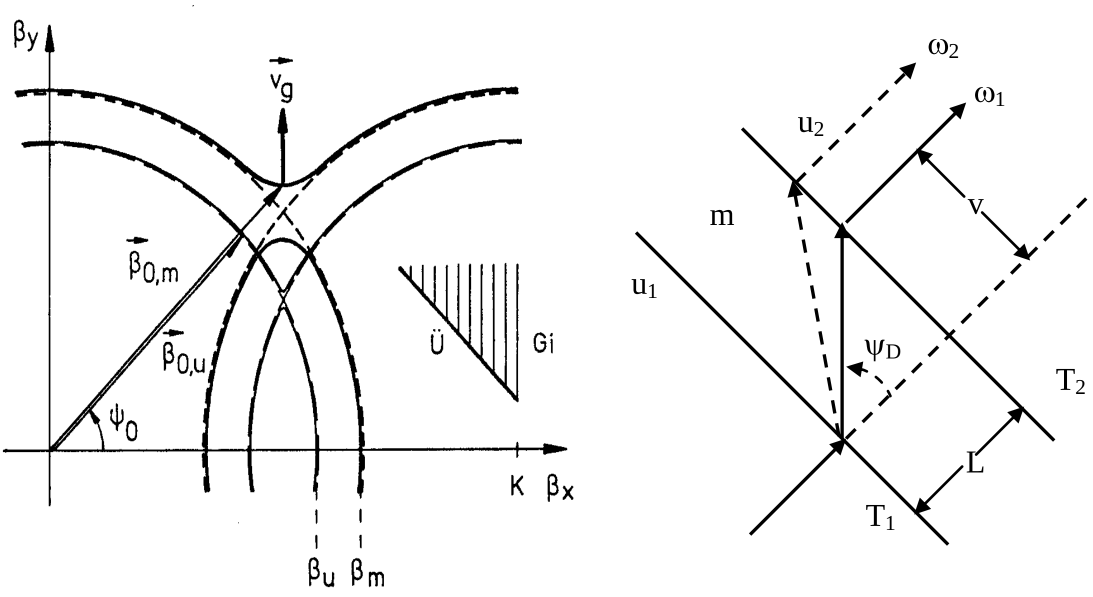

(a) (b)

Fig. 5.1. Beam-steering and lateral beam shift of a guided beam propagating across a 1D photonic crystal waveguide embedded in between two smooth waveguide regions. The periodic structure is inclined by an angle of 45 degrees with respect to the straight boundaries.

(a) Representation in the wavevector diagram (WVD) and (b) in real space, according to [Zen87].

The effect of frequency-dependent beam-steering was experimentally proven and investigated in [Zen87] for a singly periodic waveguide oriented at an angle of 45 degrees with respect to the straight boundaries embedded in between two unmodulated regions (see Fig. 5.2). Strong beam steering (Fig. 5.2.b) leads near the photonic bandgap to a significant lateral beam-shift after passing through the photonic crystal part. Increasing the optical carrier frequency in the vicinity of "strong dispersion" below the photonic bandgap (Fig. 5.2.d) can even significantly increase the amount of lateral beam shift.

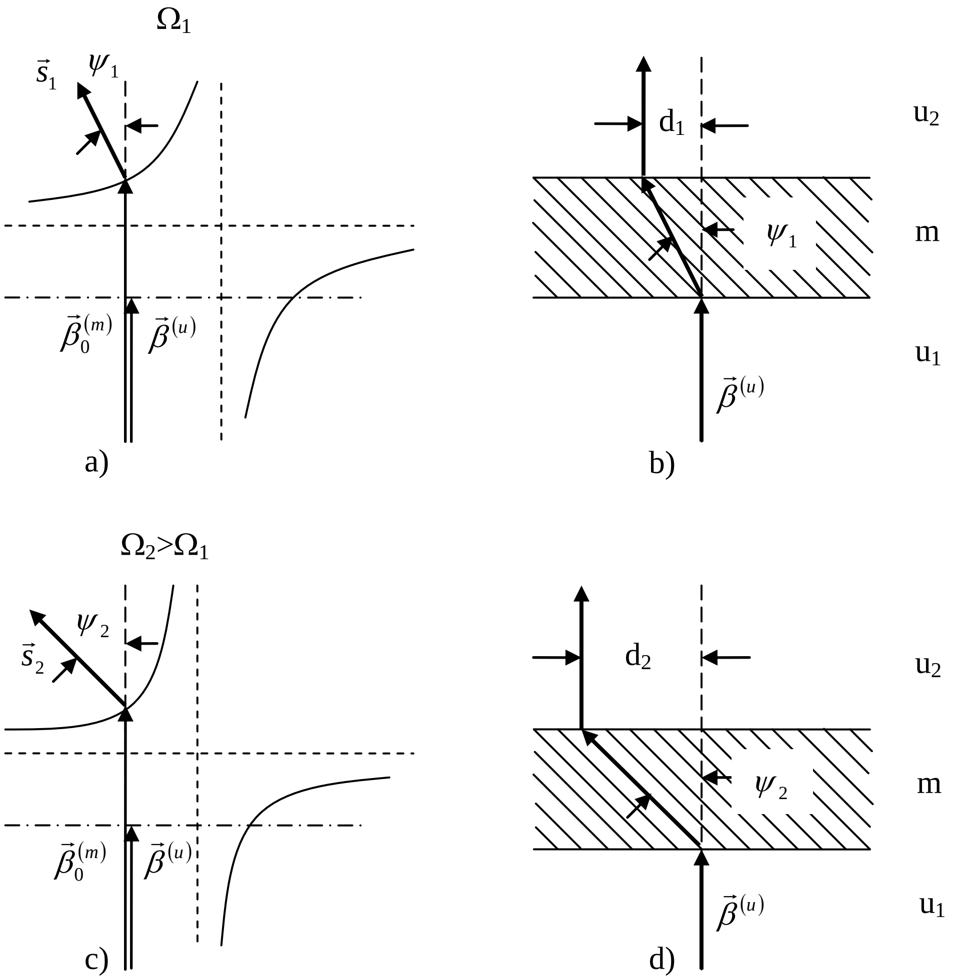

Fig. 5.2. Frequency dependence of the lateral beam shift produced by a 1D photonic crystal waveguide at frequencies (normalized to the center frequency of the photonic bandgap) in a range below the optical bandgap

(a), (c) Representation in WVD and (b), (d) real space (dashed lines are linearized detail of the approximation circles).

In the subsequent chapters we will discuss the usage of the above explained effects for dispersion management in telecommunications.

For adaptive dispersion management one can profit from the combined effect of the spatial and chromatic dispersion. This can be intuitively explained by the old experimental verification in Fig. 5.3, which was shown for the first time concerning photonic crystal waveguides in [Zen79]. Here in a 1D photonic crystal waveguide embedded between two unmodulated regions both dispersion parameters are changed: the angle of incidence using a divergent Gaussian beam, and the frequency.

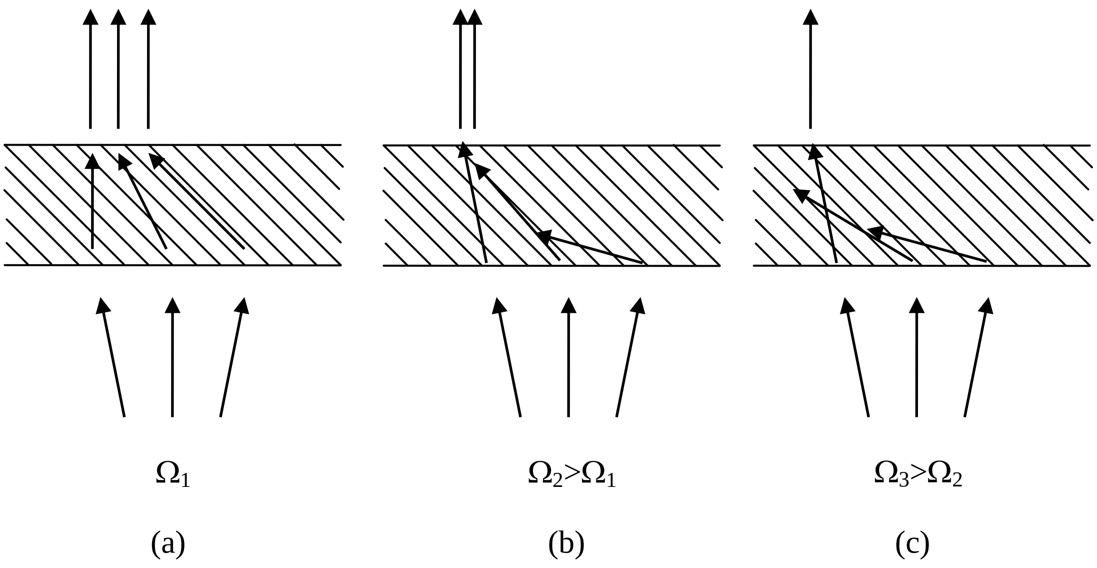

Fig. 5.3. Verification of angular and frequency dispersion in a 1D photonic crystal waveguide [Zen79].

In all three cases a slightly divergent beam is propagating upwards in a smooth waveguide region for different normalized frequencies (normalized with respect to the center of the photonic bandgap). Small changes in the angles of incidence with respect to the normal of the boundaries (represented by a divergent beam) reveal the strong angular dispersion of the resulting lateral beam shift. Additionally, small changes in the carrier frequency (b,c) have substantial influence on the amount of lateral beam-shift, too.

In Fig. 5.3 a divergent input beam (carrier wavelength around 600 nm) is launched into a smooth planar waveguide (lower parts), travels then through a 1D photonic crystal waveguide and propagates - after leaving the corrugated region - along a following smooth waveguide. This is done at three different optical frequencies with the normalized deviation from the center of the photonic bandgap of $\Omega_1 > \Omega_2 > \Omega_3$. One can see two different dispersion phenomena: First angular dispersion: A slight change of the angle of incidence of an input beam with narrow angular divergence leads to a lateral beam-shift indicating the effect of "super-refraction" in the periodic structure. On the other hand, maintaining the angle of incidence results in a frequency dependent beam steering angle and thus in a frequency-dependent lateral beam-shift as already shown in Fig. 5.2.

5.3 Device layout

For tuning (adaptation) of the chromatic dispersion we use the combined spatial and chromatic dispersion effects described in chapter 5.2. The overall layout of the dispersion compensator in Fig. 5.4 consists of two structures with complementary layout of the inclined gratings each located between smooth waveguides. The gratings itself can be turned in opposite directions, thus the incident and the output beams remain at the same positions only in the center region there is a parallel shift of the "beam". So the dispersive effects of both single structures can be doubled and the outgoing beam is collinear to the incoming beam.

Dispersion adaptation can be done by turning both gratings in opposite directions by the angle Φ_{incl}. This is shown in the dashed part in Fig. 5.4 assuming the same optical carrier frequency at the entrance of the whole structure.

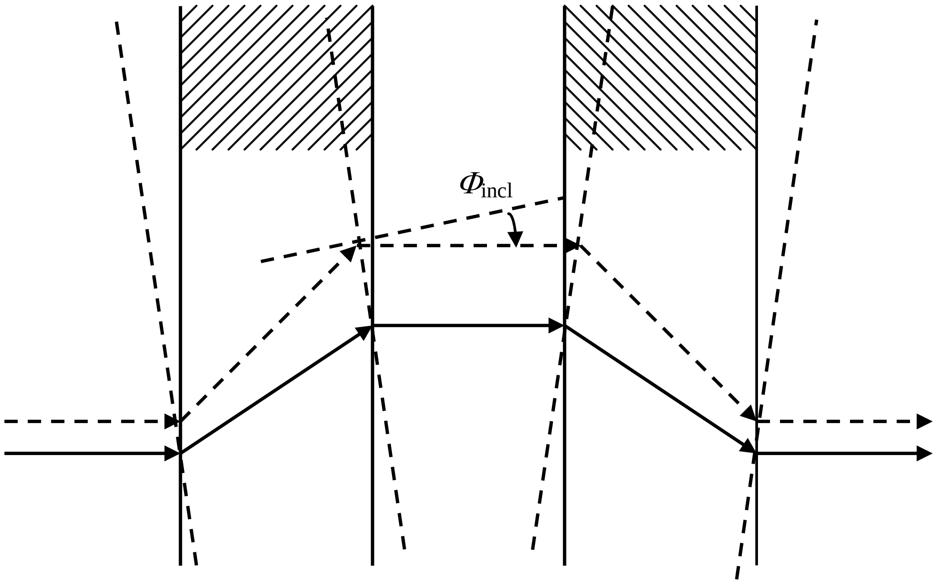

Fig. 5.4. Dispersion compensator, consisting of two complementary inclined 1D photonic crystal waveguides.

Tuning can be done by changing the angle of inclination Φ_{incl} of both substructures in a reverse sense.

The normal group velocity dispersion in the structures above is even enhanced for large beam steering angles due to the fact, that the resulting effective group velocity (which is "lowered") is the projection of the group velocity in the direction of incidence. The group velocity itself can be deduced from the gradients in the WVD being normal to the dispersion contours.

For increased dispersion one can insert in the space between both periodic structures a series of different delay lines (similar to arrayed waveguide structures as planar lightwave circuits, so-called PLCs) maintaining the possibility for tuning of dispersion. Additional spectral adaptation may be also possible using a free space interface region in conjunction with switchable adaptation of delay lines for tailoring of the spectral time delay.

In chapter 5.4 we investigate the group-velocity dispersion using a 1D grating structure which - in principle - shows similar characteristics like that in Fig. 5.2. However, the theoretically investigated structure is only 10 µm long and based on the parameters of current III-V semiconductor technology for new one- and two-dimensional functional devices [HKF03]. Here we use an array of vertically oriented infinite slices to get a two-dimensional structure for numerical simulations with a grating constant of 282.2 nm.

5.4 Method of investigation

The so-called group velocity is mathematically well defined and represents the velocity of energy flow i.e.. the velocity of the movement of envelope of a wave packet. The signal for transmission will be detected as the time varying energy flow onto the optical receiver. In a direct detection system this signal is represented by the envelope of the modulated optical carrier amplitude. Group velocity dispersion leads to signal distortion. If - due to an extreme group velocity dispersion - the envelope is too strongly distorted, signal transmission will be impossible. Thus in these cases it makes no longer sense to look for terms for higher order dispersion. Only in the case of dispersion compensation this may be helpful.

Here we look quantitatively at the dispersion that may be introduced or compensated using an adaptive photonic crystal structure. This is done in a direct way: looking at the propagation of an optical impulse for characterisation of the energy flow.

The whole layout for simulations is a combination of three substructures as shown in Fig. 5.5. It consists of two homogeneous waveguides with the effective index $n_{eff} = 2.3$. The photonic crystal structure in the centre is a one-dimensional grating structure consisting of vertical slices inclined at an angle of 45 degrees with respect to the straight boundaries and having a constant refractive index of $n = 3.2$.

In order to obtain a realistic insight in the dispersion phenomena we launched for numerical evaluation a short optical pulse in the lower homogeneous medium of our layout, shortly in front of the grating structure and looked at its propagation through the grating and the subsequent unmodulated waveguide represented again by a homogeneous medium.

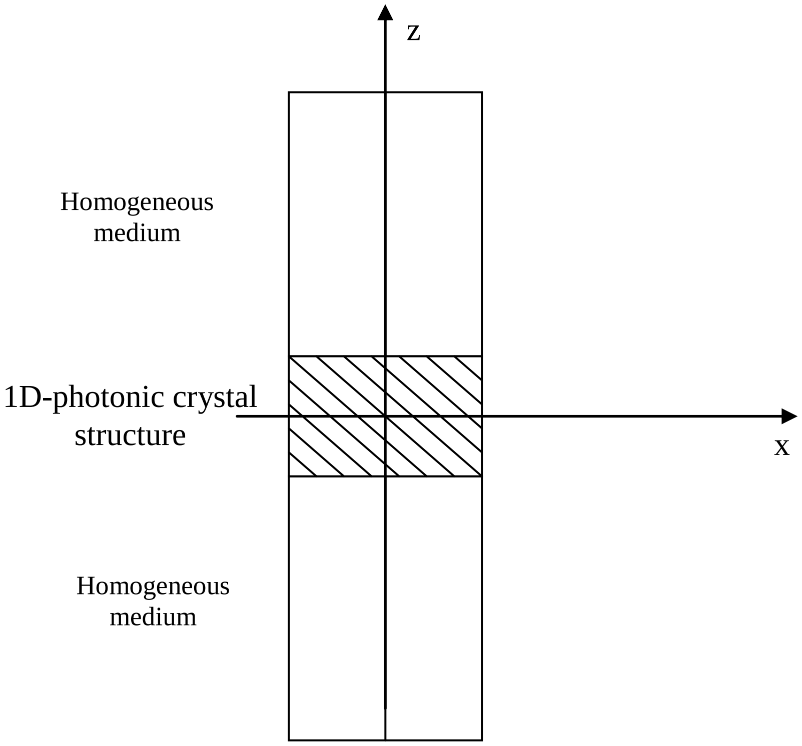

Fig. 5.5. Layout for simulation of the group velocity dispersion.

The simulation is performed using a 2D FDTD software which permits to obtain the output fields as a function of space along a predefined trace and at a fixed time. We launch a Gaussian beam right in front of the photonic crystal structure. The launched wave packet with transverse Gaussian field distribution (spot-size about 10 µm) is a single impulse with an excitation impulse width of 0.015 ps in time space (FWHM) corresponding to an impulse width of 4.5 µm in real space.

The position of the launch field in *x* direction is at $x = 6$ µm and in *z* direction this is

$z = -6$ µm, which means 1 µm just in front of the grating structure. We simulate three different cases for the angle of incidence with respect to the normal of incidence (being equivalent to the *z*-axis): 0, 2, and 4 degrees. In order to maintain the major pulse propagation directions (in the *x*-*z* plane) after passage of the photonic crystal structure, the time monitor is also set at 0, 2 and 4 degree inclination, respectively. In every case, we simulate pulse propagation in a wavelength range from 1100 nm to 1600 nm with the wavelength step-size of 20 nm.

After wave propagation through all three subsections, the output beam is monitored in the third subsection after the same predefined time *T* by a series of time monitors however at different carrier wavelengths. From the output field monitored by the time monitor, one can determine the position of the envelope of the light pulse after a given time *T* and then one can calculate the group velocity.

As examples for impulse propagation at different carrier frequencies with different group velocities in the grating region, Fig. 5.6 and Fig. 5.7 show the impulse propagation in the unmodulated region after passing the photonic crystal waveguide region. This is drawn for the above mentioned very short optical impulse in order to have a good possibility for comparison of impulse propagation at the carrier wavelengths of 1320 nm and 1180 nm at an inclination angle for the incoming Gaussian beam of 0 degrees with respect to the normal of incidence. The origin of the *z'*-coordinate is located 25 µm after the end of the periodic structure.

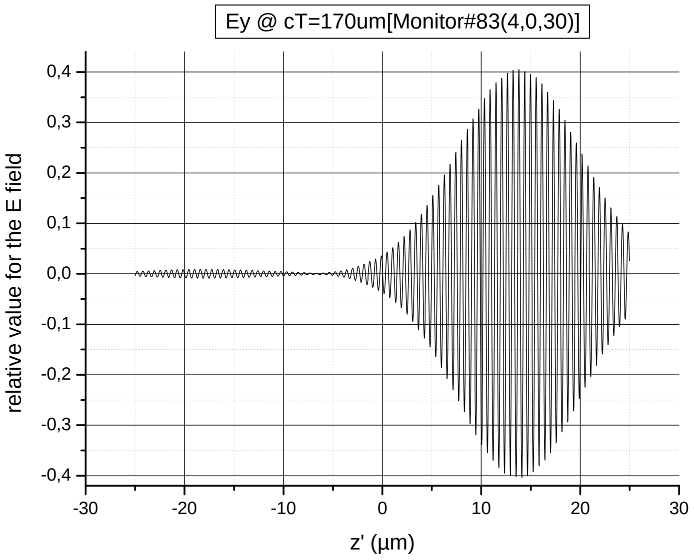

Fig. 5.6. Impulse propagation at 1320 nm, angle of inclination: 0 degrees.

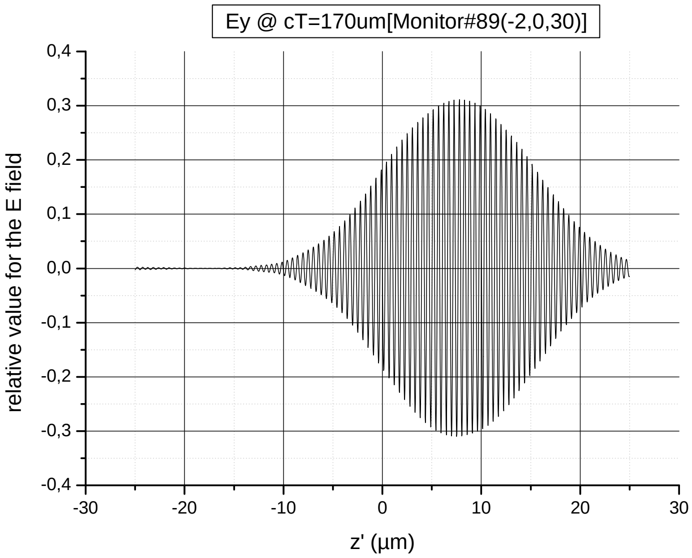

Fig. 5.7. Impulse propagation at 1180 nm, angle of inclination: 0 degrees.

In order to get the correct values for the group velocity, one has to analyse precisely the movement of the envelope function of the propagating electromagnetic field. As the "test impulse" for efficient calculations is very short, its spectrum on the wavelength scale is relatively broad and covers about 25 nm. From the envelope, one can easily determine the position of the beam and after that calculate the group velocity. For precise evaluation of the envelope, we have to demodulate the signal. So, at first we take the fast Fourier transform of the signal. As the envelope function has only low frequency components, we used appropriate low-pass filtering, getting the spectrum of the envelope. After inverse Fourier transformation we can determine the signal in time space and get the position of the impulse from the following approximation, valid for weakly distorted impulses: Take the two-sided 70 % values of the field (corresponding to the FWHM of the local power) and use the average for getting the position z_{sig} of the impulse centre.

The numerical reference value of group velocity in the homogeneous regions can be obtained by simulating the impulse propagation along the homogeneous medium for two different spans T_1 and T_2 at the appropriate wavelengths. Taking into account impulse propagation in all three different substructures at known geometry one can calculate the resulting group velocity in the *z* direction. Repeating this procedure for every wavelength in the range from 1100 nm to 1600 nm, we obtain the group velocity in the photonic crystal waveguide as a function of wavelength.

The result of numerous runs is presented in Fig. 5.8 for 3 different angles of inclination to the normal of incidence: 0, 2 and 4 degrees. As one can clearly see: far away from the photonic bandgap (for wavelengths exceeding 1500 nm) the angular spread of the group velocity is low, however near the photonic bandgap (at wavelengths below 1100 nm) this spreading is very pronounced and can be used for adaptive dispersion compensation.

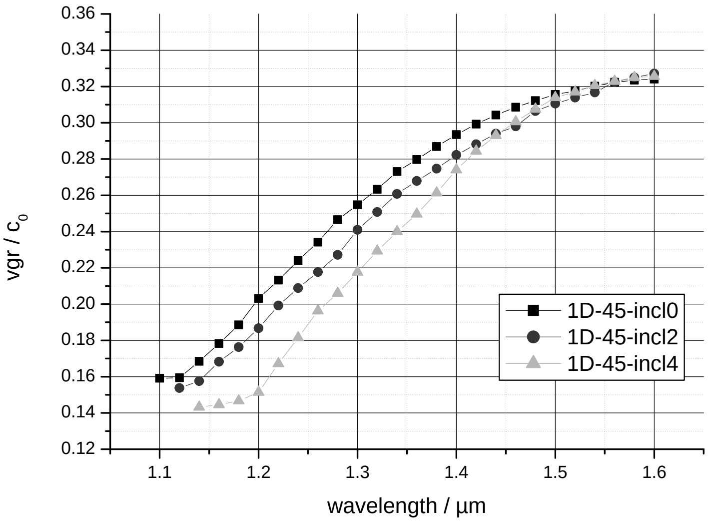

Fig. 5.8. Group velocity (normalized to the vacuum velocity c_0 of light) in the photonic crystal structure (projection versus the *z*-axis) near the photonic bandgap as a function of wavelength for different angles of inclination: 0, 2, 4 degrees.

In a second step the calculated group velocity dispersion was used to make a linear model of a 1D waveguide. This waveguide is added to a conventional fibre link operated at 640 Gbit/s RZ-transmission.

5.5 Numerical results for adaptive dispersion control

The results of our investigations in the previous chapters will now be used for demonstration of adaptive dispersion compensation in an optical link. For possible applications in ultra-high speed communications we take an OTDM system comprising 16 time-multiplexed channels at 40 Gbit/s per channel, resulting in a bit sequence of 640 Gbit/sec. In this case the FWHM for a single pulse must be significantly lower than 1.5 ps and thus we take 0.5 ps FWHM for the RZ-signal.

We extrapolate the chromatic dispersion properties of our structures to structures with a length of 10 mm both on the "demultiplexer" and "multiplexer" sides.

The program used for simulation of the propagation system is described in detail in [Qua03]. The nonlinear system of equations is derived from Maxwell’s equations in order to model the signal propagation in single mode optical multi-channels systems. Here, the nonlinear terms are systematically considered in the equation system and are solved step by step along the propagation line using numerical methods. The solving algorithms of equation systems are developed based on the Split-Step-Fourier-Method. In each split-step step, the Runge-Kutta-Method is used. The propagation system is divided into three functional groups: the sender, the propagation line and the receiver as in the Fig. 5.9.

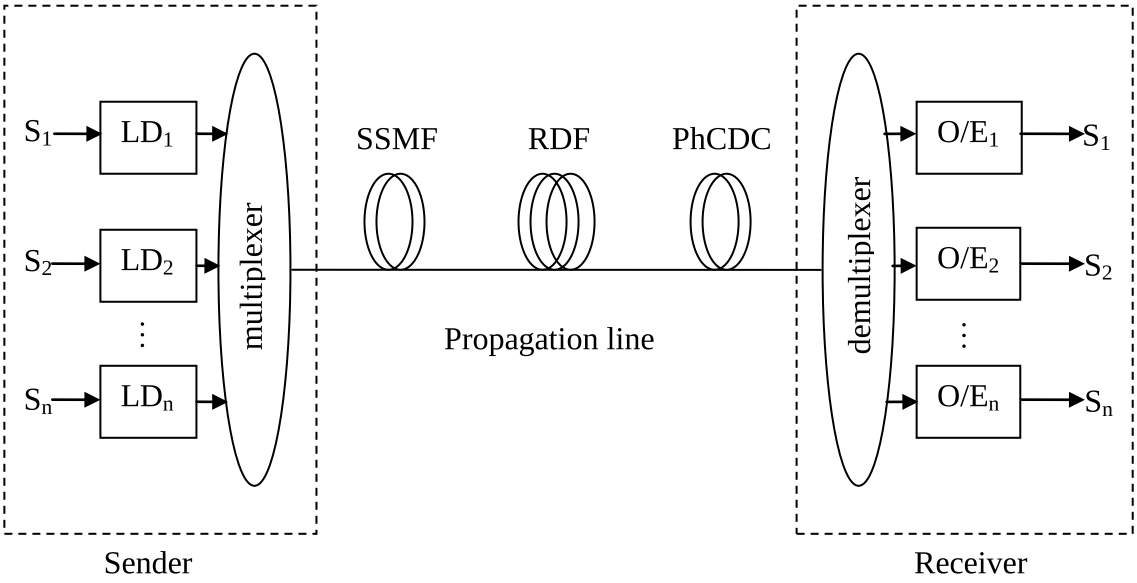

Fig. 5.9. Optical wavelength division multiplex system.

The dispersion parameters of the photonic crystal dispersion compensator are calculated from the group velocity characteristics in section 5.4. Group velocity is described as a function of wavelength $v_{gr}(\lambda)$ [m/s]. The group delay τ is then analysed as

$\tau(\lambda)=1/v_{gr}(\lambda)$ [s/m]. After chaging in unit scale, we got $\tau(\lambda)$ [ns/km].

Then, $\tau(\lambda)$ is approximated in a 7-order polynom:

$$\tau(\lambda)\left[\frac{ns}{km}\right]=a_0+a_1\lambda+a_2\lambda^2+a_3\lambda^3+a_4\lambda^4+a_5\lambda^5+a_6\lambda^6+a_7\lambda^7\cdot \tag{5.1}$$

From $\tau(\lambda)$ in (5.1), the dispersion parameters of the photonic crystal dispersion compensator can be calculated with the unit of λ of µm as follows:

$$\tau(\lambda) = \beta_1 \tag{5.2}$$

$$D_2(\lambda)\left[{}^{ps}\!\big/_{nm \cdot km}\right] = \frac{d\beta_1}{d\lambda} = \frac{d\tau}{d\lambda} = a_1 + 2a_2\lambda + 3a_3\lambda^2 + 4a_4\lambda^3 + 5a_5\lambda^4 + 6a_6\lambda^5 + 7a_7\lambda^6 \tag{5.3}$$

$$D_3(\lambda)\left[{}^{ps}\!\big/_{nm^2 \cdot km}\right] = \frac{dD_2(\lambda)}{d\lambda} \cdot 10^3 = \left(2a_2 + 6a_3\lambda + 12a_4\lambda^2 + 20a_5\lambda^3 + 30a_6\lambda^4 + 42a_7\lambda^5\right) \cdot 10^3 \tag{5.4}$$

For the unit normalization, the multiplication with 10^3 is needed.

$$D_4(\lambda)\left[{}^{ps}\!\big/_{nm^3 \cdot km}\right] = \frac{dD_3(\lambda)}{d\lambda} \cdot 10^6 = \left(6a_3 + 24a_4\lambda + 60a_5\lambda^2 + 120a_6\lambda^3 + 210a_7\lambda^4\right) \cdot 10^6 \tag{5.5}$$

For the unit normalization, the multiplication with 10^6 is needed.

D_2, D_3, D_4 are the dispersion parameters of the photonic crystal dispersion compensator. In this case, only the chromatic dispersion D_2 is considered.

First we look at data transmission over a 10 km span of standard single-mode fiber at a carrier wavelength slightly above vanishing chromatic dispersion. The remaining dispersion is partly compensated by a reverse-dispersion fiber (RDF) as e. g. suggested for ultra-high bitrate transmission [NYT02]. At the end of this link we insert our photonic crystal dispersion compensator with an effective length of 20 mm. The length of the RDF is chosen as 428 m for perfect dispersion compensation in the overall link and at an angle of inclination of the PhC-compensator of 2 degrees. This is illustrated in Fig. 5.10 for the cases of the original impulse, the impulse after propagation along the SSMF, after propagation along the RDF (resulting in an impulse broadening of more than a factor of 4) and after passing the additional dispersion compensator. The final impulse shape is nearly identical to the original one. Changing the angle of inclination to 4 degrees shows a significant impulse broadening of a factor of > 2 (Fig. 5.11). Perfect compensation of the chromatic dispersion can be reinstalled for a modified length of the RDF of 421 m (Fig. 5.12). So our structure can be used for compensation of tolerances of the required fiber lengths in ultrahigh-speed signal transmission. Assuming a tuning range of +/- 2 degrees around an inclination angle of 2 degrees, in the case of the RDF a full span of 421 m to 431 m for the length of the RDF - this means a length variation of about 10 m - can be adaptively compensated.

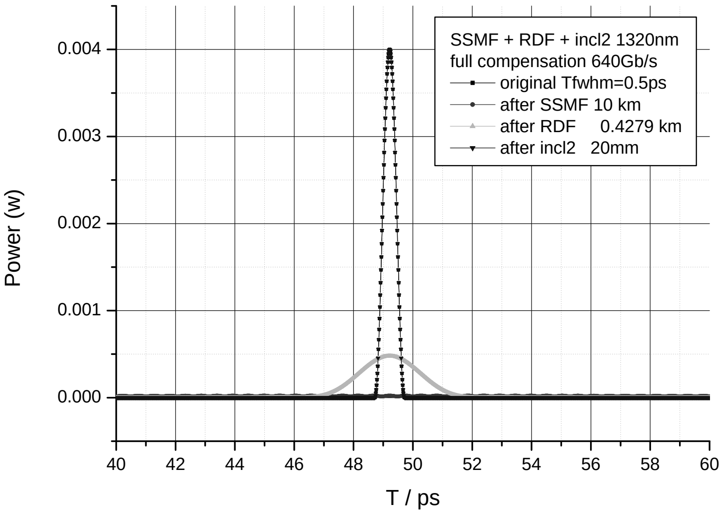

Fig. 5.10. Compensation of the chromatic dispersion at a bitrate of 640 Gbit/s. Full dispersion compensation in the overall link at an angle of inclination of the PhC-compensator of 2 degrees.

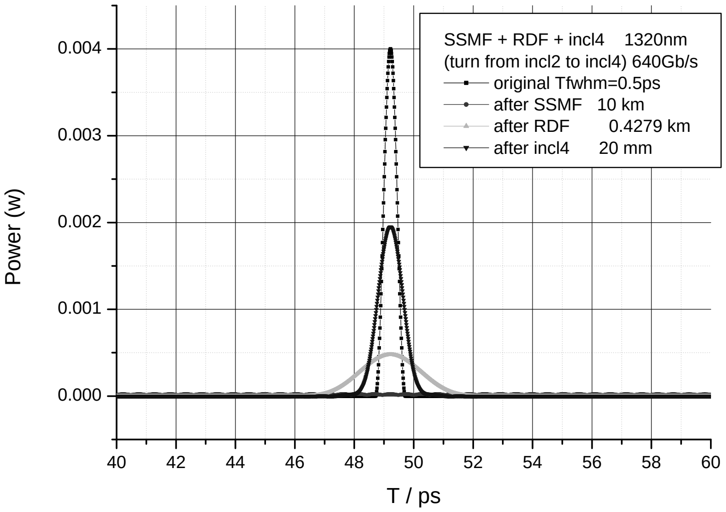

Fig. 5.11. Compensation of the chromatic dispersion at a bitrate of 640 Gbit/s.

Changing the angle of inclination to 4 degrees shows a significant impulse broadening of a factor of > 2.

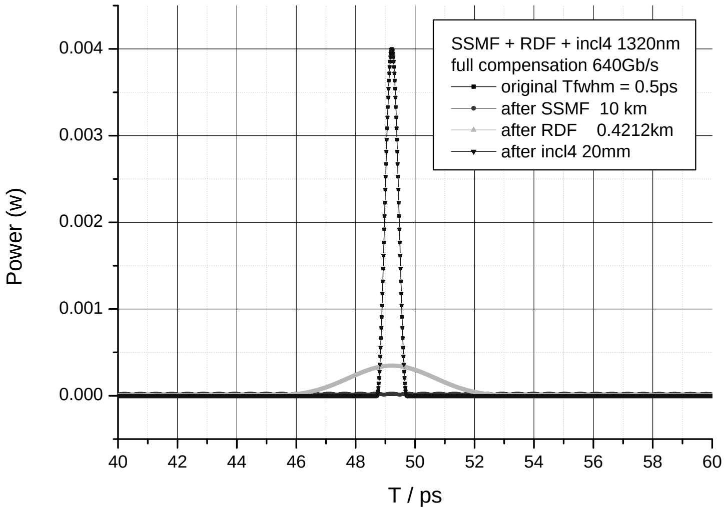

Fig. 5.12. Compensation of the chromatic dispersion at a bitrate of 640 Gbit/s. Perfect compensation of the chromatic dispersion can be reinstalled for a modified length of the RDF of 421 m.

5.6 Conclusion

In summary, we demonstrated theoretically the principle of adaptive dispersion compensation using one-dimensional photonic crystals in planar waveguides. The principle of operation is based on the combined strong angular and chromatic dispersion of wave propagation in these waveguides. Adaptive dispersion compensation is done by turning the photonic crystal structures.

Chapter 6

Wide-angle beam refocusing using negative refraction in non-uniform photonic crystal waveguides

6.1 Introduction

Anomalous refraction phenomena in electrodynamics such as negative refraction have a long history, dating back to a speculative discussion by A. Schuster in 1904 [Sch1904]. Far later on in 1968, Veselago intensively studied the general properties of wave propagation in negative refractive index media [Ves68]. Especially for applications in the microwave region, Silin described negative refraction in a review [Sil72]. Dated back to 1978, Silin also described the possibility to construct a plane-parallel lens [Sil78] using a material that allows for negative refraction at the straight boundaries to the surrounding medium providing an internal ray crossover, and it was expected that artificial media will also be found for the optical range to construct such a lens.

For optical wavelengths the basics of dispersive and refractive properties of strongly modulated 1D and 2D periodic light-guides near the optical bandgap were investigated in [Zen79, UZ80]. The fundamentals of anomalous refraction phenomena such as superrefraction and negative refraction with respect to the group velocity directions were explained in detail both theoretically and experimentally using Floquet-Bloch waves and wave-vector diagrams (WVDs). In a later publication [Zen87], further details on refraction, frequency dependent focusing and Floquet-Bloch wave interferences inside a doubly periodic lightguide as well as imaging phenomena including the crossover effect of ray propagation were explained. In more recent publications, Kosaka also describes super- and anomalous refraction [KKTNTSK98], which is an interference effect of Floquet-Bloch waves [Rus86]. Wave-vector representations were also used by Notomi [Not00] especially for the explanation of negative refraction. All-angle negative refraction for imaging with a photonic crystal superlens at very small distances with respect to the photonic crystal structure was described by Luo [LJJP02], however, with several constraints on incoming wave-vectors and dispersion contours. Wave focusing inside a negative index photonic crystal slab was also recently reported by A. Martinez [MM05]. The phenomenon of negative refraction at the boundaries from homogeneous to periodic structures can be obtained in several ways. One way is the usage of the first photonic band and a direction of propagation in wave-vector space being around one of the corners of the first Brillouin-zone. This leads in a relatively small frequency band to the required concave shape of the relevant part of the dispersion contour, as shown in [Zen87, LJJP02]. The other way is to use - in an appropriate frequency band - the nearly circular shape of the dispersion contour around the origin in a higher-order photonic band [Not00, MM05].

Left-handed materials with their inherent negative refractive index allow for a similar ray path to construct a "perfect lens" [Pen00]. Refocusing using negative refraction was also studied recently experimentally [BMSQTTA04] in the near infrared using photonic crystal waveguides. As an additional design tool, polarization discrimination using polarization dependent beam-steering in PhCs [Zen88] may be also taken into account. High-resolution superlens imaging in a triangular photonic crystal has been investigated theoretically [WRK04] at abrupt boundaries, however, resulting in reduced transmission efficiency. The strong influence of the surface termination for a good image quality is analyzed in [XQRH04]. An intense study of mainly near-field imaging phenomena in photonic crystal slabs is given in [LL03], and self-focusing in the microwave regime is described in [MMGM04].

A number of imaging principles were demonstrated in the past, however, for potential applications they have to be combined with efficiency. Here, the results of a theoretical study with the main goal of efficient far-field imaging (refocusing) of wide angle (high NA) Gaussian beams are presented. The major problems to solve in this case are the reduction of reflection losses due to mismatch at the boundaries of the photonic crystal slabs and to find a solution of the inherent problem that the real shape of the dispersion contours of a homogeneous photonic crystal usually causes significant aberrations at high NA.

To reduce the reflection problem, gradual (tapered) transitions will be used. The advantage of such transitions was also already widely investigated in early experiments [Zen87]. For solving the problem of precise imaging, an inhomogeneous photonic crystal structure is introduced, with a non-uniform background refractive index of the still homogeneous grating itself in order to get additional degrees of freedom for design. Using these principles, far-field refocusing of a Gaussian beam by a photonic crystal slab is presented for a spot-size of 1.6 µm emerging in air, and a more tentative layout is given for refocusing in a dielectric "immersion material" to reduce the spot size to 0.8 µm, both in the infrared region at 1345 nm.

6.2 Principle of operation and design of the investigated structures

The basic principle of beam refocusing in a photonic crystal structure is negative ray refraction at interfaces to homogeneous media. Here, a 2D highly modulated square grating structure inclined at 45 degrees with respect to the straight boundaries is used. For quantitative evaluation a grating consisting of cylindrical dielectric columns (refractive index of 3.2) with a pitch of 282 nm, embedded in air is assumed. For the case of homogeneous 2D photonic crystals (PhCs) the principle of imaging is described in Fig. 6.1 (a, b), the case of an inhomogeneous photonic crystal structure including a lateral gradient in the background index (characterized by areas with different grey levels, details see below) is shown in Fig. 6.1 (c, d). The representations both in real space and in wave-vector (reciprocal) space are used. For simplicity only the relevant inner parts of the dispersion contours in the wave-vector diagrams (WVDs) are drawn and only TM-polarization is considered. In both cases, a highly divergent Gaussian beam is launched in air at a distance of several micrometers in front of the photonic crystal, using a wavelength of 1345 nm. This corresponds to a normalized frequency of 0.21 (which is defined as the ratio of grating constant to the wavelength a/λ).

After refraction at the first boundary, the path of the transmitted rays are redirected forming a crossover so that - after passing the second boundary of the photonic crystal - the emerging beam is strongly convergent in air with a beam waist ("focal point") at the same distance to the boundary as for the incident beam. This beam path is due to negative ray refraction and is explained in Fig. 6.1 (a, b) using - besides the central unperturbed ray - some outermost "rays". Due to boundary conditions, an incident ray represented by the wave-vector ① will be transformed at the boundary to a set of Floquet-Bloch waves with identical group velocity directions as described in the WVD. The direction of energy flow in the photonic crystal is indicated by the vector ② resulting in a direction of energy flow in real space as shown by vector ③. At the second boundary the Floquet-Bloch waves are reconverted into single waves oriented in the original direction ④, however, laterally shifted, so that the original divergent beam is now convergent with nearly the original beam waist in the focal point. This kind of propagation was in principle demonstrated and explained in [Zen87] for visible light.

The shape of the dispersion contour in the WVD of a homogeneous PhC however is not well suited for precise refocusing of wide-angle beams due to "over-focusing" as will be shown later on. Advanced dispersion engineering however allows for defined local tuning of the dispersion contours as shown in Fig. 6.1 (c, d). This is done by changing the background index of the photonic crystal (i.e., the basic refractive index in the periodic regions to which the index difference of the dielectric columns with respect to air has to be added. So, here it is set to *nback* = 1.0). In certain segments the background index can be increased by individual values of *dnback*, resulting in different "local forms" of the dispersion contours, whereas the periodic modulation of the photonic crystal itself remains still homogeneous (constant index change of the dielectric columns with constant diameter). The result in real space shows that with the aid of inclined boundaries between the regions of different background index, ray redirection is also possible to form a convergent beam for refocusing, however with the additional freedom of beam shaping to compensate for angular aberrations, maintaining the advantage of plane boundaries.

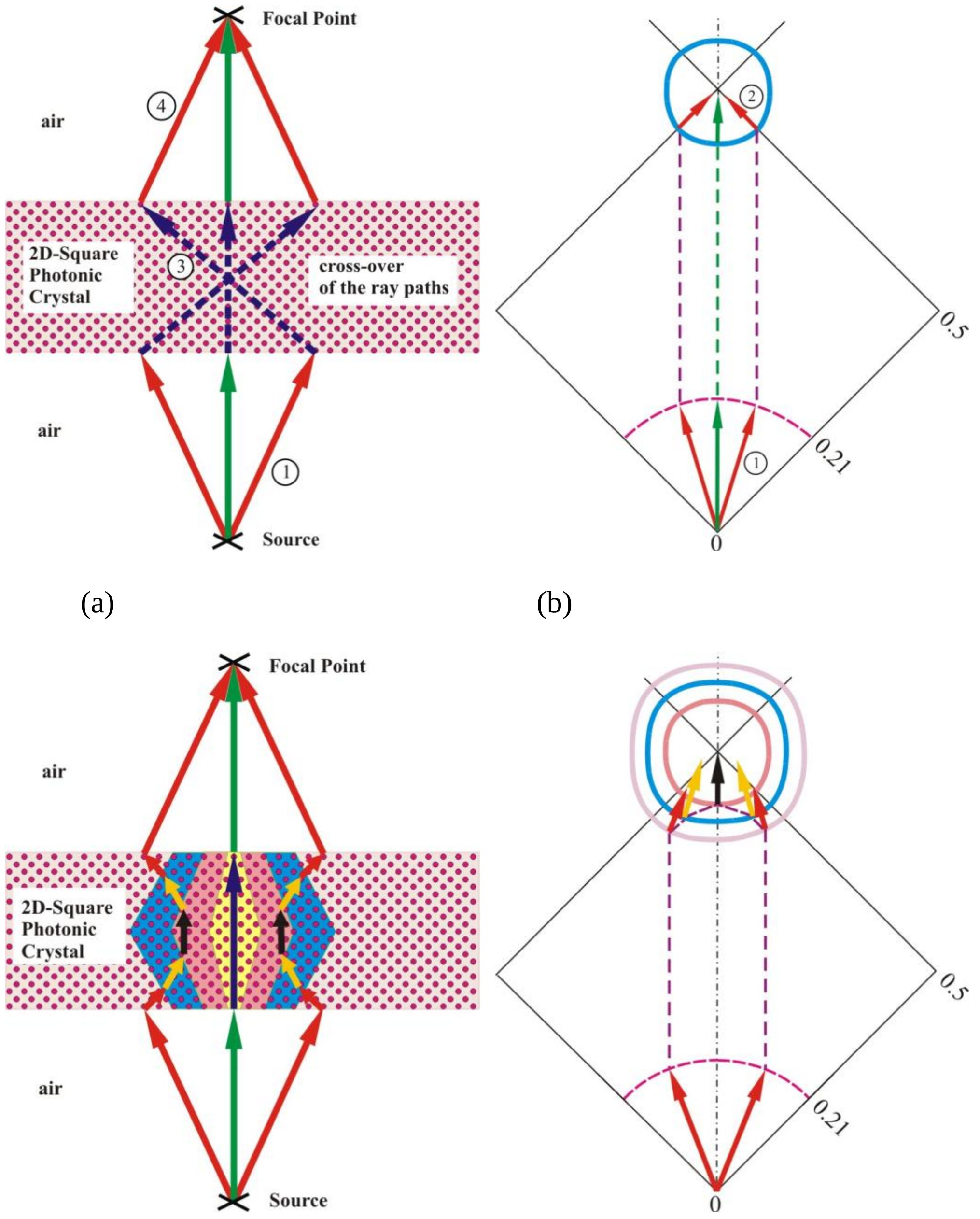

(a) (b)

(c) (d)

Fig. 6.1. Principle of refocusing in real space and in wave-vector space explained in a WVD (only the central and outermost ray paths are drawn). The WVD is normalized to the grating constant. (a, b) homogeneous (c, d) inhomogeneous photonic crystal at a normalized frequency of 0.21. In (c, d) we use three different values of *dnback* (0.43, 0.45 and 0.5 for the inner contour curve).

In the case of a lateral index gradient, one special phenomenon has to be taken into account for optimum power transfer using our initial layout: In real space there exists no longer a crossover for the ray path. The continuity condition with respect to the oppositely slanted boundaries at the second half of the PhC cause only a cross over of the ray directions in the k-space during propagation in this part of the PhC structure, whereas in real space no crossover takes place and the major trace of energy flow remains at its original side with respect to the normal of the transitions (details later on in Fig. 6.3).

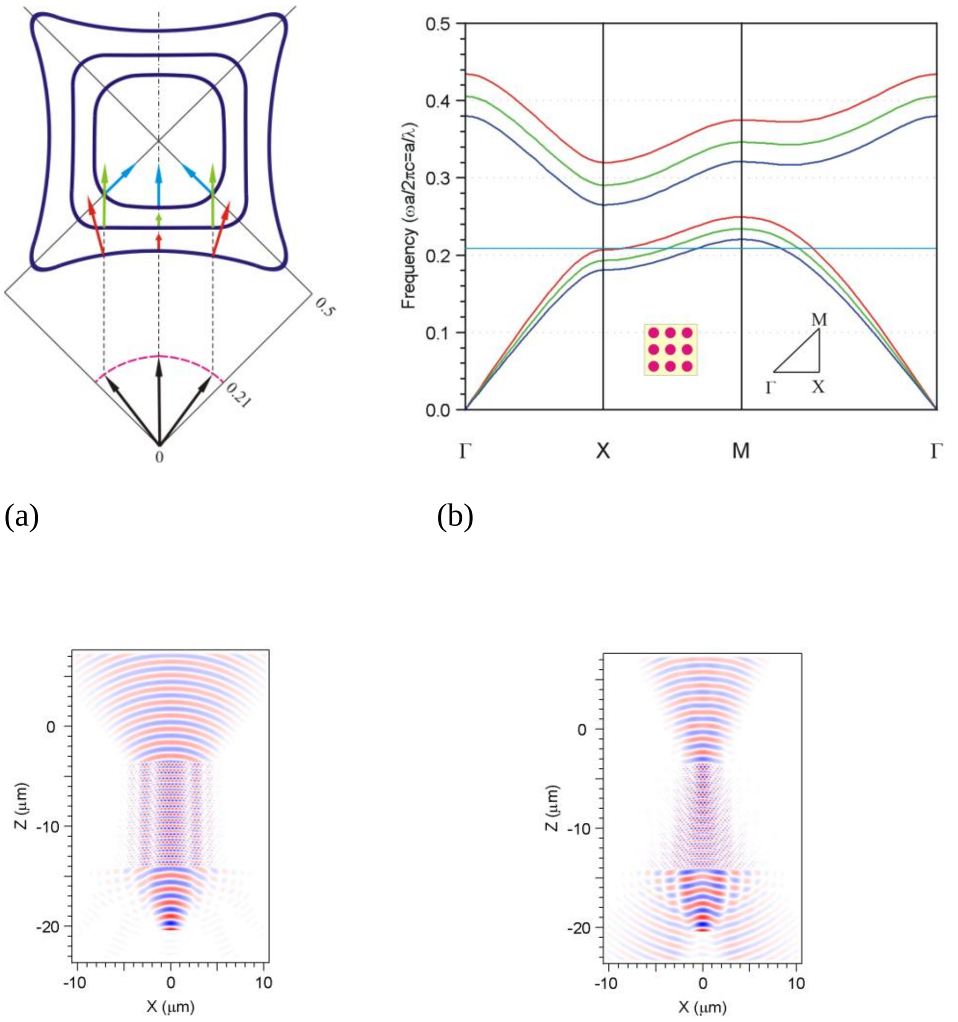

(a) (b)

(c) (d)

Fig. 6.2. (a) Wave-vector diagram: Detail oriented in the launch direction at different background refractive index differences (*dnback* = 0.0; 0.2; 0.4) at constant wavelength of 1345 nm. (b) Band diagram including the used frequency of 0.21. (c) Shift of the (real) beam waist from z = -20 µm to a virtual beam waist at z = -10 µm due to "wide-angle self-collimation" at *dnback* = 0.2. (d) Shift of the image beam waist to the second transition by negative ray refraction.

In Fig. 6.2 some quantitative details for this new kind of dispersion engineering at constant optical carrier in a normalized WVD (Fig. 6.2.a) are given. They were calculated using algorithms based on a semi-analytical approach and plane-wave expansion [Lem02]. The corresponding band diagram with the frequency of operation in the first photonic band is given in Fig. 6.2.b. The background index is varied from 1.0 to 1.4.

Depending on the background index in wave-vector space, three different principal orientations for the vectors of energy flow can be stated. For the case of *dnback* = 0.0, an incident divergent beam remains divergent in the PhC, too. For *dnback* = 0.2, however, we get a very special solution: For an incident beam covering a total angular range of about 75 degrees , the direction of energy flow remains in the direction of the central ray. Thus self-collimation ("beaming") can be maintained over a large angular range. This was also verified by numerical simulations using a 2D finite difference time domain (FDTD) method. In Fig. 6.2.c. the strongly divergent incident beam emerges with the same wave-field after passing the PhC. Its origin, however, is shifted by the length of the photonic crystal region. For *dnback* > 0.2, the phenomenon of negative ray refraction takes place and allows for beam focusing in the photonic crystal itself. In Fig. 6.2.d the focus is located at the second boundary. Further increase of *dnback* leads to a stronger angular deflection and shifts the "focus" inside the photonic crystal for imaging applications as explained above. A similar behavior is also possible by changing the optical carrier wavelength instead of *dnback.*

Another crucial point for wide-angle refocusing is the usable angular range of the incident divergent beam due to the limited angular extension of the inner dispersion contour in the WVD. In [LJJP02] the conditions for extension and shape of the dispersion contours for the photonic crystal itself with respect to the diameter of the air contour are given to get "all-angle" negative refraction for imaging applications. However, no compensation of aberrations is possible. In our cases, the major restriction - concerning a homogeneous photonic crystal - remains the same: For "all-angle" refocusing the projection of the outermost region of the nearly circular dispersion contour for the photonic crystal with respect to the boundary between the homogeneous medium and the photonic crystal itself must be larger than the corresponding projection for the circle representing the effective index in the homogeneous region outside the photonic crystal. In our "wide-angle" case of Fig. 6.1.d the radius of the outer - nearly circular dispersion contour - represents an "effective index" of 0.66 leading to an angular acceptance range of about +/- 40^0. As can be seen from the outermost dispersion contour in Fig. 6.2.a a locally restricted partly concave shape (for getting group-velocity vectors being directed versus the grating diagonal) is sufficient to accept also larger angles of incidence. Thus, in order to extend the acceptance angle, or to realize "all-angle" refocusing also for surrounding homogeneous media with a refractive index $nhom > 1$ (leading to larger free-space circles instead of the air contour) we can take advantage of our inhomogeneous photonic crystal design. Large acceptance angles of the divergent incident beam can be achieved by using - for the outer angular regions - photonic crystal sections with extended dispersion contours, corresponding to small background indices. Subsequent correction of focusing aberrations is done by specially designed crystal inhomogeneities (see below). Therefore, our concept of using inhomogeneous photonic crystals by changing the background refractive index has two important consequences: Real wide-angle imaging up to "all-angle" imaging using moderate beam-steering angles (for high coupling efficiency) and compensation of inherent aberrations in square photonic lattices by proper layout of the inhomogeneity itself.

As can also be seen from Fig. 6.2.a, the steering-angle of energy flow in the outer angular parts is too high, leading to overfocusing in outer angular ranges as already explained in [Zen87]. The possibility of compensation by introduction of different background indices is explained in Fig. 6.3 by taking only an inclined, slightly divergent Gaussian beam (waist of 5 µm) at the same launch position to represent the outer "rays" in Fig. 6.1. With the large beam waist, only Floquet-Bloch waves in a small angular range in the WVD are excited, corresponding to wave-vector directions around the launch angle of the incident ray.

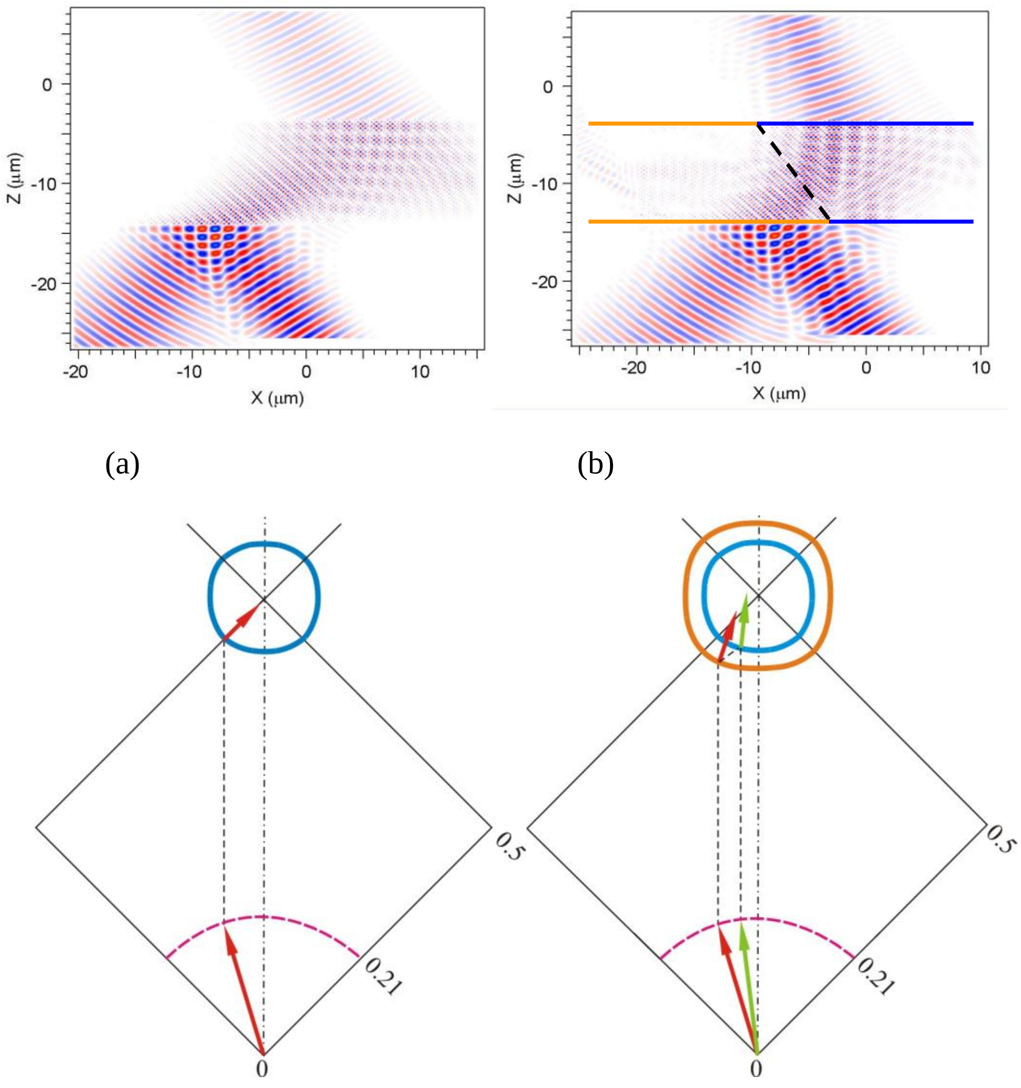

(a) (b)

(c) (d)

Fig. 6.3. (a) Negative ray refraction in a homogeneous 2D-photonic crystal, (b) Negative ray refraction and ray redirection in a 2-section inhomogeneous 2D photonic crystal; dashed line: Boundary for different background indices.

Fig. 6.3 (a, c) shows the conventional case of negative ray refraction in a photonic crystal with homogeneous background index. In Fig. 6.3 (b, d) the background index at the right hand side with respect to the dashed boundary is larger. Due to the boundary condition the ray is redirected into the direction of the grating diagonal, giving the explanation for the ray trace in Fig. 6.1.c. Thus, this local dispersion tuning allows for compensation of "imaging aberrations", however, maintaining the advantage of plane boundaries.

Local variation of the background refractive index is one possible way of aberration correction. Our approach may be replaced by changing the radius of the dielectric columns as explained in section 6.5.

One remarkable effect caused by the divergence of a Gaussian beam is that the divergence of the original beam (convex wave-fronts) is maintained after reflection, however, due to negative ray refraction the transmitted beam is convergent (concave wave-fronts) and – in the case of change to another background index in Fig. 6.3.b – the transmission direction in air is also modified.

6.3 Effect of tapered transitions

It is well known that strong beam-steering effects occur in PhCs near the edges of the photonic band gap. As there exists also a strong dispersion of the group velocity, its absolute value can be highly different from the values of the surrounding homogeneous media, leading to significant mismatch problems and thus low coupling efficiency. Here we use a taper structure which allows for significant reduction of reflections over a wide angular range. For our generalized layout in Fig. 6.4.a we use a 10-step bilinearly tapered transition, where the refractive index of the homogeneous section (*n*hom) decreases linearly in the taper section down to a predefined background index (in the cases presented here: *nback* = 1.0) in the PhC itself, whereas the refractive index of the grating columns increases linearly to a maximum, maintaining the radii of the dielectric columns.

In order to show the efficiency to reduce reflections over a large angular range using our proposal, the subsequent numerical experiment using 2D - FDTD- simulations was done: We take the worst case of a refractive index *nhom* = 1.0 for the homogeneous region outside of the periodic structure and its transitions and look at the reflection properties only at one transition. Therefore possible interference phenomena caused by multiple reflections at two boundaries are avoided. For ease of numerical evaluation we take an incident Gaussian beam with a spot size of 5 µm, launched shortly in front of the transition at different angles and investigate the reflection properties. As a measure of the reflection properties we take the ratio between the maximum local power in the "reflected" beam and the incident beam, corrected with respect to the intensity decay along the path of the Gaussian beam, as drawn in Fig. 6.4.b.

For comparison we investigated three cases: Firstly we consider the case of a step transition with an angular span for the incident beam from normal incidence up to an angle of 50 degrees. The other cases use a 10-step transition with 9 tapered intermediate columns, by changing their refractive index. For the tapered case we use both a linear taper and a nonlinear (exponential) one. The classical step-like transition reveals already at normal incidence a high power reflectivity of 38 %. This increases gradually to up to 63% at an angle of incidence of 50 degrees. The linear taper decreases - at normal incidence - the reflection to about only 2 % with a gradual increase for angles below 20 degrees. At 30 degrees the residual reflection still remains half of the value for a step-transition. For still larger angles of incidence the reflectivity increases to about the values for a step transition. Using a nonlinear tapering the residual reflection can be reduced to nearly zero in an angular range of up to 20 degrees, however, a better compromise to enhance the angular range is to allow for some residual reflection for small angles. The result is shown in Fig. 6.4.b and reveals a reduction of the power reflection by a factor of 10 up to about 20 degrees and still nearly by a factor of 3 up to an angle of incidence of 35 degrees. So both tapered transitions are well suited as highly transparent interfaces for transmission of wide-angle beams.

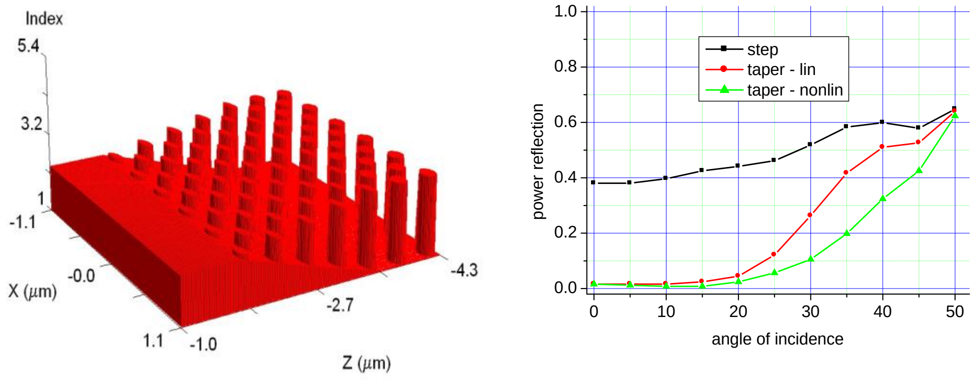

(a) (b)

Fig. 6.4. (a) Refractive index profile used for modeling the tapered photonic crystal transitions using 9 rows of dielectric columns: Generalized layout with a refractive index of the surrounding medium $nhom \geq 1$ (b) Simulation results for the power reflection at different angles of incidence with respect to the *x*-axis and $nhom = 1$. Three cases are drawn: Step-like transition, linear and nonlinear taper functions with respect to the change of the refractive index of the columns.

6.4 Simulation results

As numerical method of investigation we use 2D – FDTD- simulations, and all our structures will be 2D devices. We investigated two series for refocusing of a Gaussian beam, one with a spot-size of 1.6 μm emerging in air ($nhom = 1$), and a more tentative layout for refocusing in a dielectric medium with $nhom = 2$ using a spot-size of 0.8 μm, both in the infrared region of 1345 nm. By scaling down the lattice constant, the principle should be applicable to refocus a beam with a spot-size of about 0.3 μm at a wavelength of 500 nm. For simplicity we use as definition for focusing efficiency the ratio of maximum power in the focal point with respect to the maximum power at the launch point.

The complete basic layout for all cases of investigation is shown in Fig. 6.5. This layout includes two tapered transitions from the photonic crystal slab to the homogeneous outside with the refractive index *nhom*. Additionally we introduce the possibility to verify lateral inhomogeneities in selected areas (see marked regions in Fig. 6.5) using a change in the local background refractive index *nback* = 1.0 by *dnback* , both in the tapered regions and in the photonic crystal itself. For the purpose of comparison, we can remove the tapered transitions and also verify a homogeneous background index.

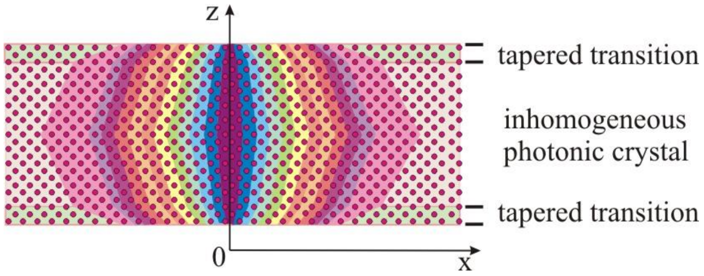

Fig. 6.5. Schematic layout of an inhomogeneous 2D photonic crystal planar lens with tapered transitions to the surrounding homogeneous medium along the *z*-axis. The background index in the marked regions can be individually changed by different values of *dnback*, forming lateral index inhomogeneities in the periodic regions.

First the focusing properties of a homogeneous photonic crystal with straight boundaries and abrupt (step-like) transitions were investigated (Fig. 6.6). A strongly divergent Gaussian beam with a spot-size of 1.6 µm was launched at z = -20 µm in air, the photonic crystal being located between -14 µm < z < -4 µm. At the expected focal point (near to z = 2 µm) we got a focusing efficiency of 19 % in air.

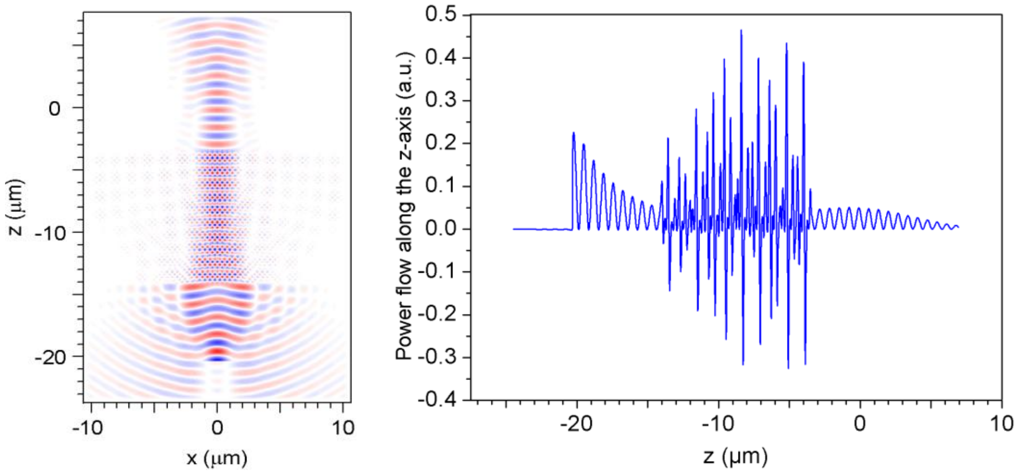

(a) (b)

Fig. 6.6. **Homogeneous** photonic crystal lens with **straight** boundaries and **abrupt** (step-like) **transitions**. Focusing efficiency**: 19 %**. (a) Field map (b) Intensity trace along the *z*-axis at $x=0$.

In order to reduce the influence of reflections at both step discontinuities we used tapered transitions as described in Fig. 6.4.a with *nhom* = 1 and get a focusing efficiency of 57.5 % (Fig. 6.7) outside the photonic crystal. Due to the contribution of over-focused outer rays the maximum local power in the PhC is shifted from the center to the first transition.

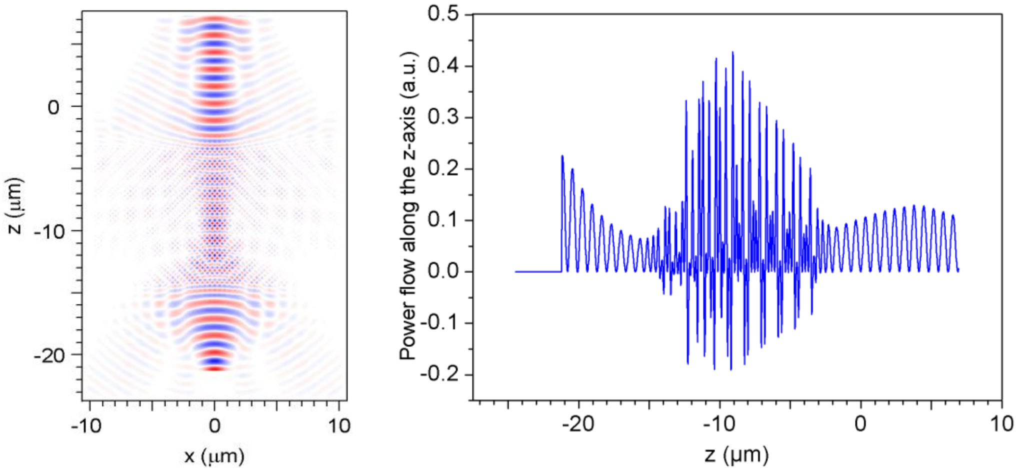

Fig. 6.7. **Homogeneous** photonic crystal lens **with tapered transitions**. Focusing efficiency: **57.5 %.**

For compensation of the significant focusing aberrations in the case of wide-angle beams we additionally tried to improve the performance by introduction of a lateral refractive index gradient. The initial runs revealed that a focusing efficiency of 90 % is - numerically - possible (Fig. 6.8). The best shape of this index gradient should be determined by further optimization using optimization algorithms.

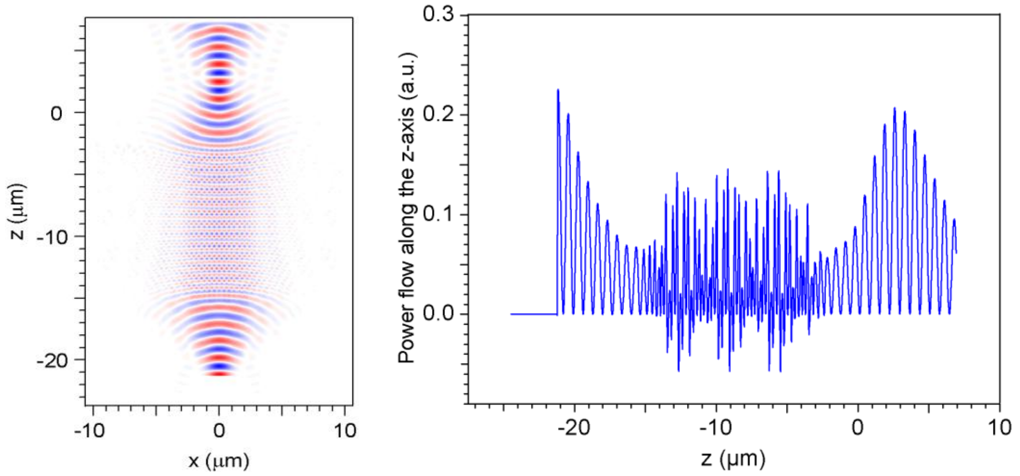

Fig. 6.8. **Inhomogeneous** photonic crystal with **tapered transitions**: Focusing efficiency: **90 %**.

In order to verify whether efficient refocusing of smaller spot-sizes is also possible, the embedding of the photonic crystal structure into a homogeneous medium with the refractive index *nhom* = 2.0 was simulated. In analogy to the numerical sequence above, a homogeneous photonic crystal with straight boundaries and abrupt transitions showed a refocusing efficiency of 19 %. Adding tapered transitions increased the focusing efficiency up to 36.5 %. Again, the best refocusing was possible with the additional lateral index inhomogeneity, leading to a focusing efficiency of 85 % (Fig. 6.9).

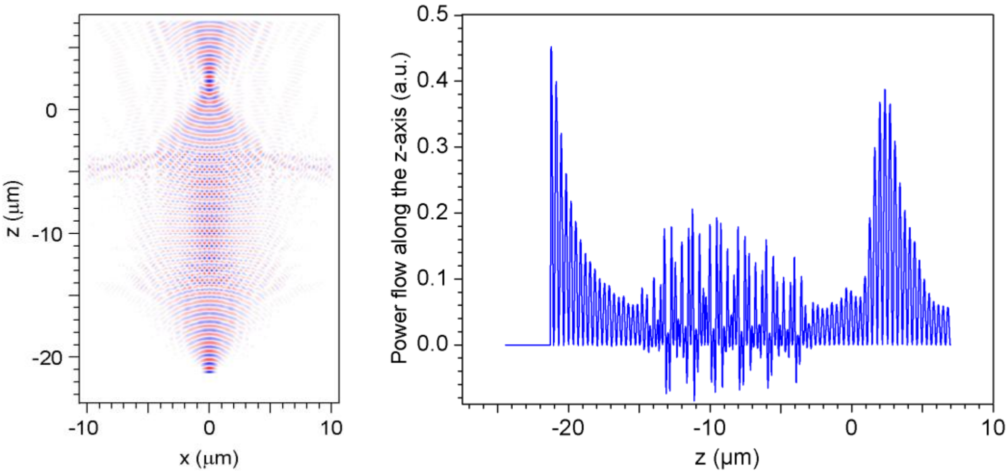

Fig. 6.9. **Inhomogeneous** photonic crystal together with **tapered transitions** to surrounding media with *n = 2.0.* Spot-size: 0.8 µm. Focusing efficiency: **85 %.**

6.5 Alternative methods for realization of inhomogeneous photonic crystals

So far, in the numerical simulations, a variation of the background refractive index both for the tapered transitions and the laterally graded photonic crystal region was used, maintaining the diameter of the dielectric columns. Another approach is to leave the background index constant and change the diameter of the dielectric columns, keeping their maximum refractive index fixed. Starting with vanishing background refractive index difference and a given radius of the dielectric columns, we determined the required change *dr* of the column radii to get (nearly) equivalent dispersion contours in the WVD with respect to the case of altering the background index. The drawings in Fig. 6.10 confirm clearly that this equivalence is possible at least in the range of a background index variation between 0 and 0.5.

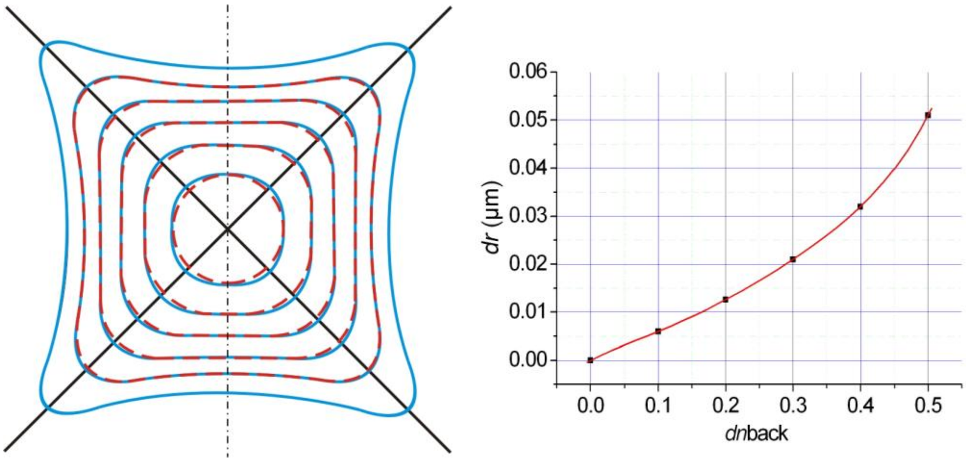

(a) (b)

Fig. 6.10. (a) Relevant detail of the WVD oriented in the direction of a grating diagonal. Equivalence between changes in the background index and the radius of the dielectric columns. The solid curves denote changes in the radii of the columns whereas the dashed curves represent changes in the background index. (b) Relation between changes in background index and variations in the radii of the dielectric columns.

6.6 Summary

We proposed and investigated the highly efficient refocusing (imaging) properties of wide-angle Gaussian beams using modified square photonic crystal structures with tapered transitions and precisely defined lateral refractive index inhomogeneities. With tapered transitions the reflection loss can be significantly reduced with respect to a step-transition up to angles of incidence of 35 degrees. For a smaller angular range almost vanishing reflection can be archived. Using the introduced new form of local dispersion engineering we were able - in a first step of optimization - to improve the refocusing efficiency to 90 % for a 1.6 µm wide Gaussian beam launched in air. At least 85 % for refocusing of a 0.8 µm wide Gaussian beam in homogeneous media with a refractive index of 2.0 are possible. Compared to a value of less than 20 % for a homogeneous photonic crystal structure with step-like transitions, this is an enormous progress in giving design rules for efficient practical applications of photonic crystal lenses.

Chapter 7

All-angle beam refocusing in non-uniform triangular photonic crystal slabs

7.1 Introduction

Despite significant progress [DEWSL06] there are still enormous difficulties in designing and fabricating materials with simultaneous negative permeability and permittivity in the optical range. Another approach is photonic crystals (PhCs) which can also show negative ray refraction of Floquet-Bloch waves without being a left-handed material.

As shown by Luo [LJJP02] all-angle negative refraction can be obtained without negative effective index using photonic crystals for imaging at very small distances with respect to a PhC slab. The sub-wavelength resolution of an image due to the negative refraction in 2D PhCs has been studied theoretically and experimentally in the microwave region [CAOFS03]. High resolution super-lens imaging in a triangular PhC has been investigated theoretically at abrupt boundaries [WRK04], however, resulting in reduced transmission efficiency. The strong influence of the surface termination on the image quality is analyzed in [XQRH04]. For highly efficient light transmission, Baba proposed different kinds of interfaces [BO01], however, not optimized for a wide range of angles of incidence. Recently, Bulu [BCO05] obtained wide-angle negative refraction and focusing of microwaves using metallodielectric PhCs. Recently it was shown [SF06] that all angle imaging can be achieved also in planar waveguides by using a hybrid metal-dielectric multilayer structure similar to the ideas of Pendry [Pen00], i.e. without the requirement of periodic or meta structures, however, the efficiency was very low.

In this chapter highly effective all-angle sub-wavelength refocusing is presented using triangular PhC slabs both in the far- and near-field domains with clearly improved far-field imaging properties in comparison to a square lattice. Point sources are introduced for precise analysis of the refocusing properties of PhC slabs for different widths ranging from 10 µm to less than 1 µm.

As the shape of the dispersion contour of the wavevector diagram for a triangular PhC slab around the origin is no ideal circle, wide-angle or even all-angle imaging with a homogeneous grating suffers from aberrations, especially for larger distances of the point source with respect to the PhC slab. So, we introduce as in chapter 6 lateral inhomogeneities in the refractive index distribution of the PhC structure to get additional design freedom for aberration compensation and compare its improvement with respect to a homogeneous crystal lattice. We demonstrate that our non-uniform PhC structure can effectively compensate for the aberrations in the far-field region with respect to all-angle imaging using triangular lattices. Moreover, by introducing a carefully positioned step-like super-structure boundary we can further reduce the wide-angle reflection loss due to mismatch at the boundaries of the PhC slab obtaining an imaging efficiency of up to 97 %.

7.2 Principle of operation

The basic principle of beam refocusing using planar PhC structures is negative ray refraction at the two interfaces to the surrounding homogeneous media as explained in chapter 6.1 and shown in Fig.7.1.a for the current crystal geometry. Here a 2D triangular lattice of air holes in a dielectric material is used with a refractive index of 3.6 and a grating constant of a = 282 nm. The radius of the air holes is $r = 0.4a$.

In order to obtain all-angle operation with small spatial distortions and relaxed design tolerances we are working in the second photonic band of the triangular photonic crystal. In Fig. 7.1 (c, d) the wave-vector diagrams are displayed for TE and TM polarizations at three different normalized optical frequencies $\omega = a/\lambda$. In both cases the optical carrier frequencies are chosen to match the size of the dispersion contours of the PhC with the size of the equifrequency contour of air (air circles). This certifies "all-angle" operation. As the inner areas of the dispersion contours of the PhC shrink with increasing frequencies, the corresponding energy flow directions (normal to the dispersion contours) are directed towards the inside. In the case of TM polarization the curvature of the dispersion contour is nearly circular (Fig. 7.1.d) and all energy flow directions are mainly oriented versus the origin. For TE polarization (Fig. 7.1.c), however, the flow directions partially show a strong deviation from pointing to the origin and does (as shown later on by numerical simulation) not allow for efficient refocusing. So we mainly concentrate on TM polarization. If appropriate parameters are chosen, the averaged radius of the photonic crystal dispersion contour in wavevector space is identical to the radius of the circular equifrequency contour representing free space (Fig. 7.1.b). With respect to the ray optical picture this provides nearly perfect negative refraction of the energy flow directions with an effective refractive index of -1 in the photonic crystal structure itself.

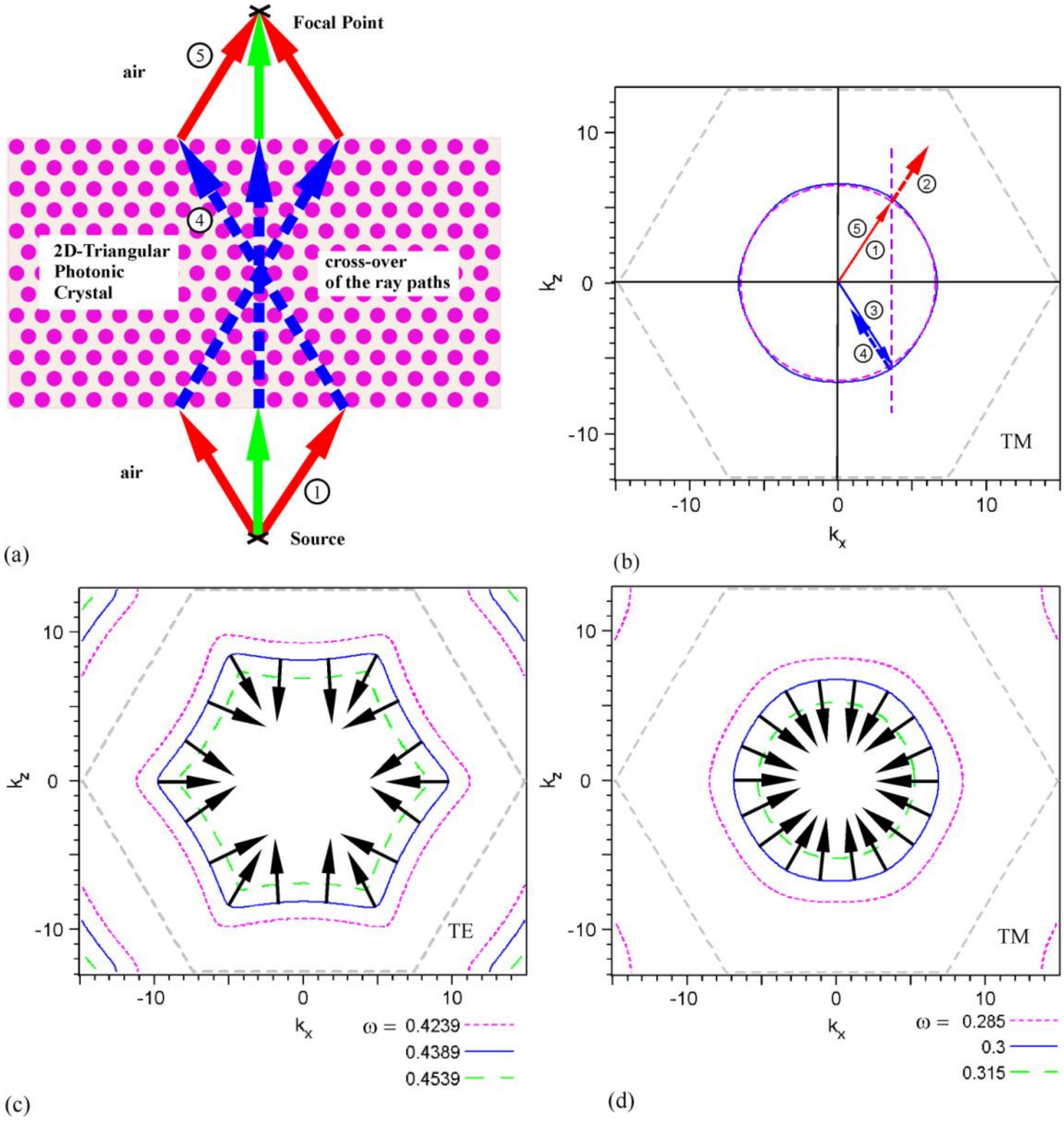

Fig. 7.1. Principle of refocusing in real space and in wave-vector space: (a) Ray path in real space (only the central and outermost ray paths are drawn). (b) Equifrequency curves in wave-vector space for explanation of negative ray refraction: Air circle (broken lines) and dispersion contour for the PhC area at a normalized frequency of 0.3018. ①, ③, ⑤ are wave-vector directions, ②, ④ are energy flow directions. (c) Wave-vector diagram for TE polarization at different normalized frequencies a/λ, (d) Wave-vector diagram for TM polarization at different normalized frequencies.

The details of imaging for the case of a homogeneous 2D photonic crystal and TM polarization are also described in Fig. 7.1(a, b) both in real space and in wave-vector (reciprocal) space at a normalized optical frequency $\omega = a/\lambda \approx 0.3$ (corresponding to a wavelength of 935 nm). The path of energy flow for refocusing is similar to the crossed ray tracing used for demonstration of a perfect lens by Pendry [Pen00]. A plane wave (represented by the wave vector ①) is propagating in air in the farfield of a point source at a certain angle with respect to the normal of incidence. This wave has the identical group velocity direction ② (normal to the air circle). At the boundary to the PhC the incident wave will be transformed into a Floquet-Bloch wave consisting of an infinite set of spatial harmonics. As the tangential component of the incident wave vector is conserved at the interface, one of the excited spatial harmonics can be represented by wave vector ③ with group velocity direction ④ (normal to the dispersion contour of the PhC). According to Fig. 7.1.b the group velocity inside the PhC is now oriented to the origin and reveals together with the group velocity direction ② of the incident wave the phenomenon of negative ray refraction at the lower boundary. After passing the PhC the Floquet-Bloch wave is reconverted at the second boundary into a single wave. This wave has now the phase velocity direction ⑤ being identical to the original phase velocity direction ①. The same happens to the group velocity direction at the second interface being again identical to the original group velocity direction ②. So the original divergent beam reconverges to a small beam waist, the "focal point".

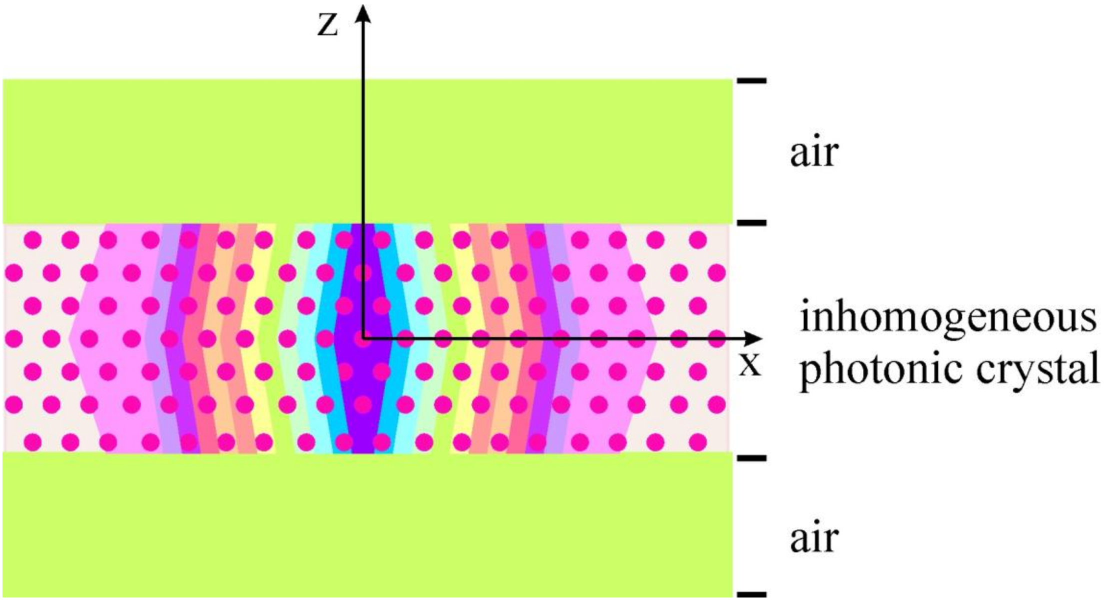

Fig.7.2. Schematic layout of an inhomogeneous 2D photonic crystal planar lens with step transitions to the surrounding homogeneous medium in the *z*-direction. In the grey scaled segments the local refractive index is individually changed, forming lateral index inhomogeneities in the periodic regions.

As the photonic crystal is a periodic and thus an inhomogeneous structure, the dispersion contours will reflect the triangular symmetry and remaining deviations from an ideal circle will occur. These deviations can be reduced by increasing the optical carrier frequency, however, leading to a smaller diameter of the photonic crystal dispersion contour with respect to the corresponding air circle and consequently to the loss of the all-angle imaging property. In the ray picture this would mean an absolute value of <1 for the negative index of refraction of the PhC. On the other hand, reducing the optical carrier frequency would increase the diameter of the photonic crystal dispersion contour and has no effect on the all-angle property, however the distortions of the "circle" increase significantly leading also to stronger imaging aberrations. So in all the subsequent investigations, we use the case of identical radii of the dispersion contours.

As already mentioned the shape of dispersion contours in the WVD of a homogeneous PhC reveals to be not a perfect circle even in the case of TM polarization. So some additional degree of freedom is needed for local adaption of dispersion contours in the PhC in order to compensate for imaging aberrations. This is done again by local refractive index variations as explained in detail in chapter 6. In certain segments, as shown in Fig. 7.2, the local refractive index in the PhC can be increased by individual values resulting in different local shapes of dispersion contours, whereas the periodic modulation of the PhC itself remains still homogeneous (constant diameters of the holes). Alternatively, as also shown in chapter 6 the change in the refractive index can be replaced by local variations of the diameters of the lattice holes. As will be clarified in the subsequent numerical calculations these lateral inhomogeneities will be the only way to get refocusing in the case of TE-polarization.

7.3 Optimized step-size boundaries

As it is intended to characterize the imaging properties of photonic crystal slabs both for the far field and near field cases we use transitions with minimized extensions in the *z*-direction. For our simulations we investigate two kinds of step transitions being convenient for low reflection losses over a wide range of angles of incidence. For comparison, we take the common truncated holes step transition [LJJP02] in Fig. 7.3.a. In order to improve especially the wide-angle behavior we add a substructure at the straight side ends of the truncated holes (Fig. 7.3.b).

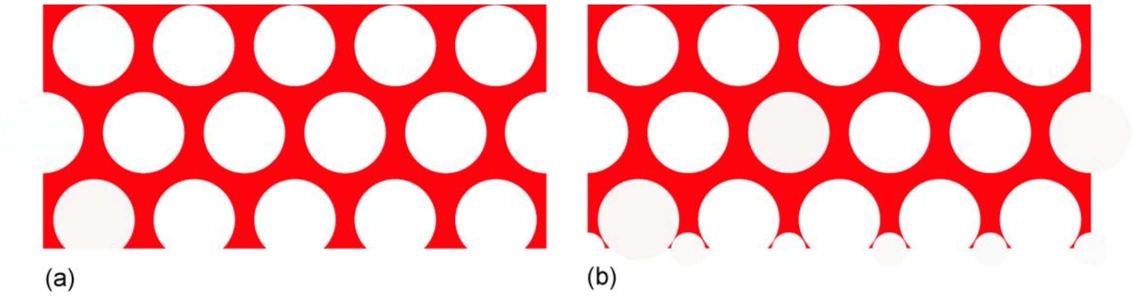

Fig. 7.3. The used boundaries: (a) Truncated holes (b) Truncated holes with superstructure.

For precise evaluation of the loss behavior we have to take into account multiple reflections at both boundaries of the PhC slabs including interference effects. Depending on the different slab widths the exact position of the step-transitions will be adapted for minimum reflection loss at normal incidence. This position will be fixed and we evaluate the angular dependency of the residual reflections using a 3 µm Gaussian beam. In Fig. 7.4 the reflection behavior is shown for a 1 µm wide slab and TM polarization. At normal incidence – due to constructive interference – for both kinds of transitions the residual reflection remains at 0.1 % or even less. As can also be seen from Fig. 7.4 the reflection loss increases for both transitions with increasing angle of incidence. However, with our superstructure this increase is strongly reduced. In the case of the superstructure boundary the residual power reflection remains below 6.5 % even for angles of incidence up to 60 degrees, whereas the simple boundary exceeds the 10 % limit already at 23 degrees indicating a significant improvement in reflection losses for the superstructure boundary at large angles of incidence.

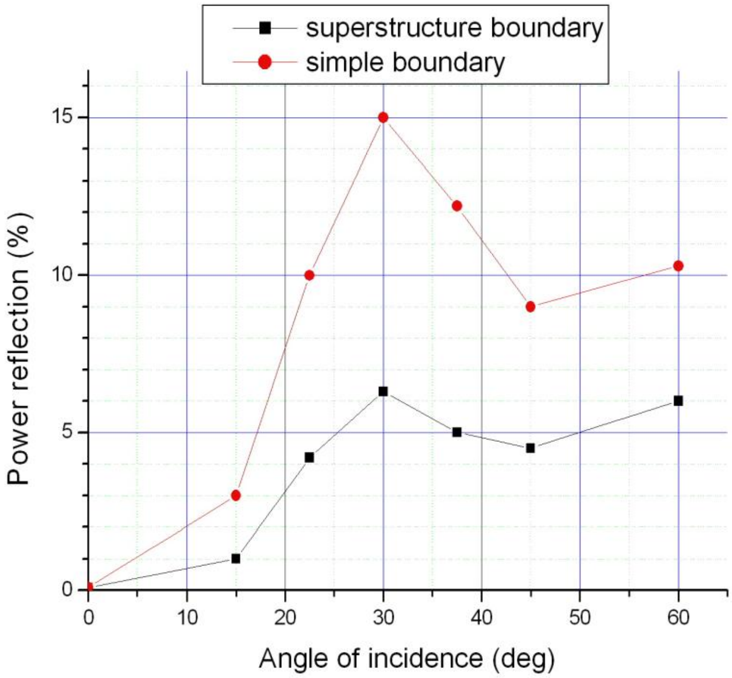

Fig. 7.4. Angular dependence of residual power reflection for a 5-layer PhC with simple (truncated holes) and superstructure boundaries using a 3 µm Gaussian beam. The optimum boundary position is chosen for the case of normal incidence.

7.4 Simulation results for different slab-widths

For the numerical calculations, we first use 2D-FDTD-simulations with the software FULLWAVE from RSOFT and take a point source for precise characterization of the refocusing properties (at a wavelength of 935 nm for TM and 643 nm for TE polarization). We investigate different widths of the PhC slab starting with a 43-layer (10 µm wide) structure and end up at a 3-layer design (about 0.6 µm wide). The launching point itself is always located in air at a distance being half of the width of the PhC slab as can be seen also from the ray path in Fig. 7.1.

In the evaluation of the refocusing properties the influences of reflection losses due to mismatch and scattering at the two boundaries were described by a transmission efficiency. Here this is the ratio of the total power flow in the *z*-direction across a plane through the refocusing point and the total power flow across a plane directly in front of the first boundary. In order to avoid the possible influence of back reflections, the second calculation (in front of the first boundary) is done without the PhC-structure itself. The second measure for characterization is the lateral focal extension of the image (refocus) in air (FWHM-values) which will be normalized to the wavelength in air. In all cases, the power flows are averaged over one period.

In the first step (Fig. 7.5.a) we took a 10 µm wide homogeneous triangular PhC with the simple boundary according to Fig. 7.3.a. The photonic crystals was exactly located between $-5.2\ \mu m < z < 5.2\ \mu m$. The point source is launched at $z = -10.4\ \mu m$ in air, and we got a transmission efficiency of 76 % for TM polarization. Although the lateral focal extension is large due to sidelobes (as can be seen from the intensity distribution in Fig. 7.5.b), we got a normalized smallest width of the refocus of 0.52 at about $z = 10.8\ \mu m$.

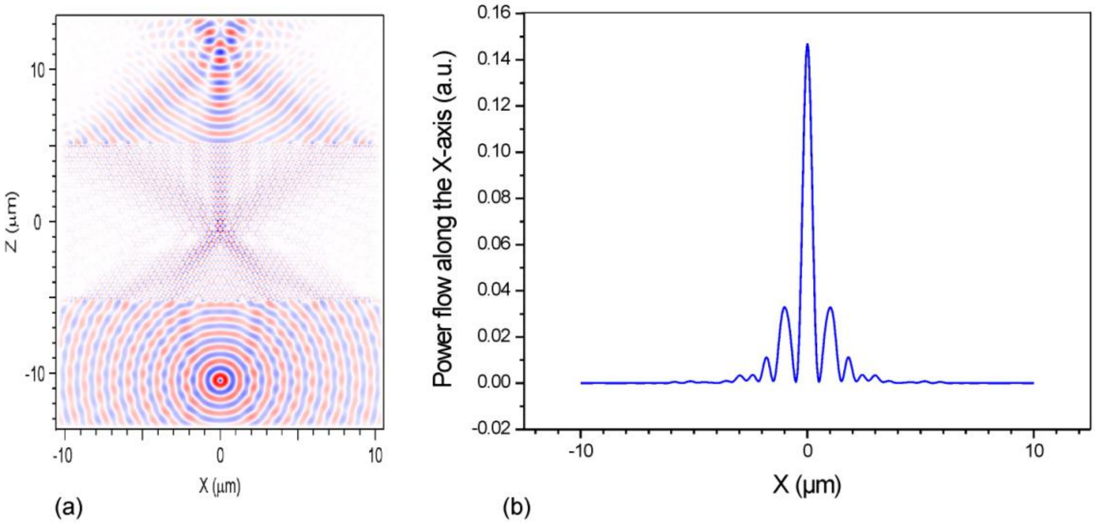

Fig. 7.5. Refocusing by a 10 µm homogeneous triangular photonic crystal lens with the simple boundary, TM polarization. (a) Field distribution, (b) Lateral intensity scan at focal point. Transmission efficiency: **76** %.

For compensation of the significant focusing aberrations due to the deviations of the dispersion curve in the PhC from an ideal circle (see Fig. 7.1.b) we introduced a lateral (not fully optimized) refractive index gradient in the PhC as explained above. For optimized positions of the simple step-transitions according to Fig. 7.3.a, we got a transmission efficiency of about 86 % again for TM polarization (Fig. 7.6.a). As can be seen from Fig. 7.6.b, the sidelobes in the lateral shape of the refocus are significantly reduced, whereas - due to being already near the diffraction limit - the reduction of the focal width to a value of 0.48 is only small. So the benefit from spatial dispersion compensation is significant at least for large widths of the PhC slab where source and refocus are clearly in the far field.

Further reduction of reflections at both transitions to the surrounding air can be accomplished with the new boundary design presented in Fig. 7.3.b. With this method losses are nearly halved and the transmission efficiency rises up to more than 93 % (TM polarization).

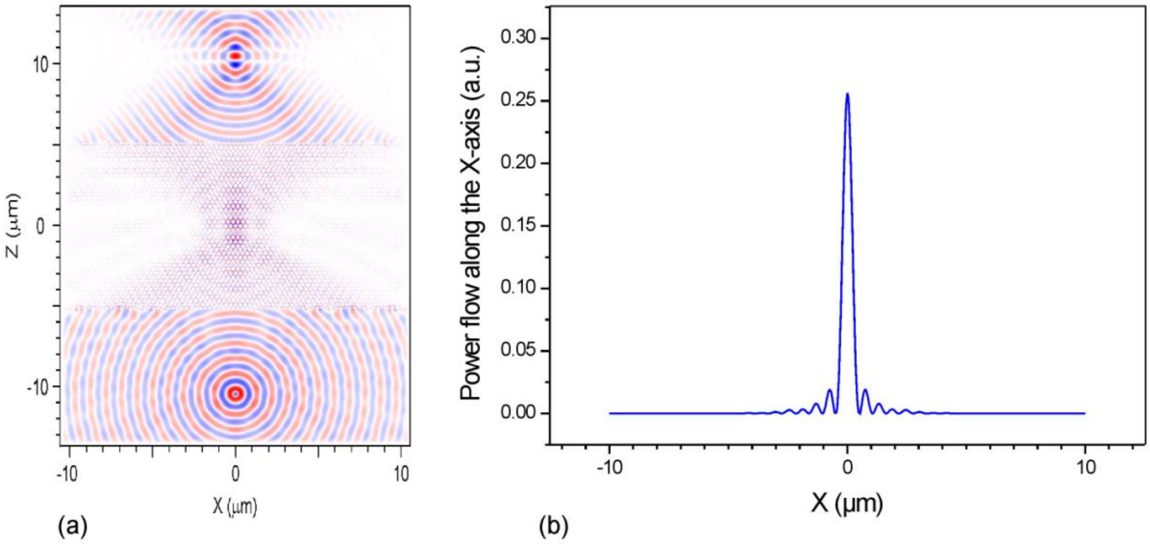

Fig. 7.6. Refocusing using a 10 µm inhomogeneous triangular photonic crystal slab with simple boundary, TM polarization. (a) Field distribution (b) Lateral intensity scan at focal point. Transmission efficiency: **86** %.

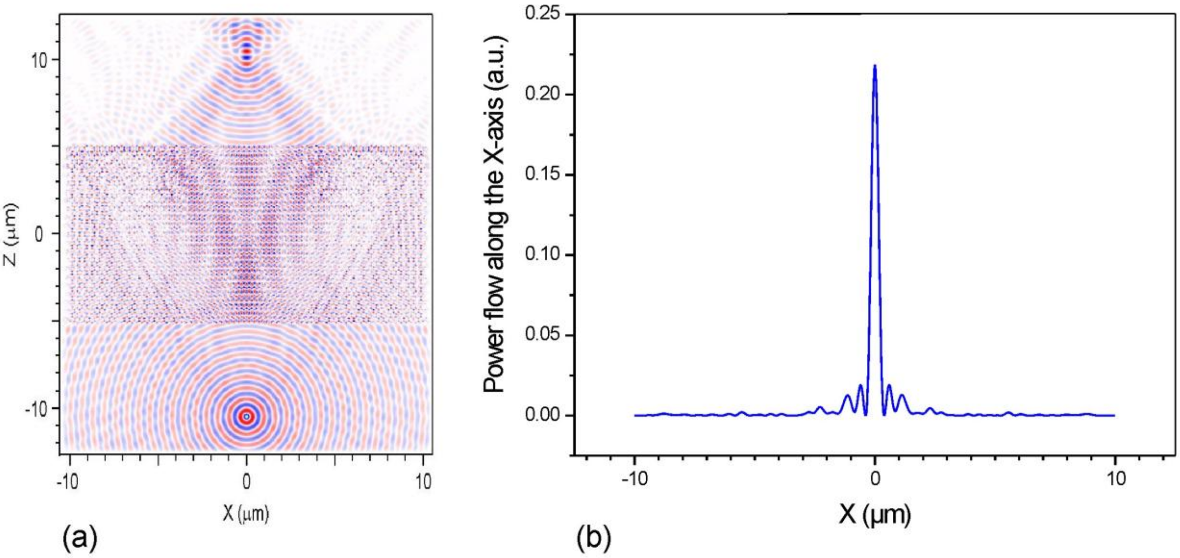

Fig. 7.7. Refocusing using a 10 µm inhomogeneous triangular photonic crystal slab with superstructure boundary, TE polarization. (a) Field distribution (b) Lateral intensity scan at focal point. Transmission efficiency: **68** %.

In the case of TE polarization the shape of the dispersion contour (Fig. 7.1.c) reveals strong deviations from a circular shape. Initial simulations show that refocusing with a homogeneous grating and TE polarization is not possible. However, introducing an appropriate lateral refractive index gradient enables refocusing again (Fig. 7.7). The (not fully optimized) values for the transmission efficiency (68 %) and normalized spot size (0.56), however, are worse than with TM polarization.

In order to investigate the refocusing properties for smaller distances between the source and the PhC a whole series of simulations for different widths of the PhC slab (10 µm, 4 µm, 2 µm, 1 µm and 0.6 µm) was calculated, however, maintaining the ray picture in Fig. 7.1. Our results for the two kinds of boundaries are summarized in table 7.1 for the simple boundary and in table 7.2 for the superstructure boundary (both for TM polarization).

Table 7.1. Refocusing properties of the photonic crystal slabs with simple boundary

Type of the PhC slab		Efficiency	Spot size
43 layers (10 µm)	Homogeneous	76.3 %	0.52
	Inhomogeneous	85.6 %	0.48
19 layers (4 µm)	Homogeneous	83.1 %	0.46
	Inhomogeneous	86.3 %	0.44
9 layers (2 µm)	Homogeneous	81.0 %	0.41
	Inhomogeneous	87.3 %	0.44
5 layers (1 µm)	Homogeneous	95.4 %	0.41
3 layers (0.6 µm)	Homogeneous	92.5 %	0.45

Table 7.2. Refocusing properties of the photonic crystal slabs with superstructure boundary

Type of the PhC slab		Efficiency	Spot size
43 layers (10 µm)	Homogeneous	83.8 %	0.52
	Inhomogeneous	93.2 %	0.48
19 layers (4 µm)	Homogeneous	90.7 %	0.46
	Inhomogeneous	91.3 %	0.46
9 layers (2 µm)	Homogeneous	84.5 %	0.41
	Inhomogeneous	86.5 %	0.46
5 layers (1 µm)	Homogeneous	96.7 %	0.43
3 layers (0.6 µm)	Homogeneous	97.6 %	0.45

Concerning the transmission efficiency for slab widths down to 2 µm lateral index inhomogeneities clearly reveal advantages. Nearly diffraction limited refocusing is possible down to a 3 layer structure. Additional improvement in the transmission efficiency can be obtained taking the new superstructure boundary. If we introduce the superstructure transition, the transmission efficiency can even be increased up to 97 % for all-angle refocusing with the 3-layer structure.

For all photonic crystal slabs with the exception of the 10 µm case, the normalized spot-size itself remains at 0.46 or below if one takes the FWHM – values. However, the sidelobes in the lateral power-flow distribution can also be significantly reduced by lateral inhomogeneities down to the 2 µm structure.

Fig. 7.8 represents the smallest photonic crystal slab taken into account. The launching point is about 350 nm in front of the boundary. As can clearly be seen, even a structure with only one complete row of holes together with 2 outer truncated rows of holes is convenient to get efficient refocusing at TM polarization.

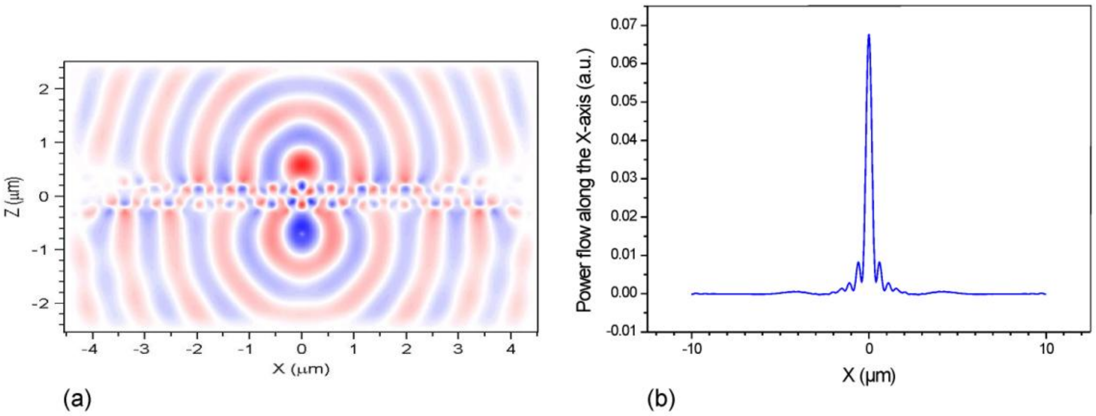

Fig. 7.8. Refocusing using a homogeneous triangular three-layer photonic crystal with superstructure boundary, TM polarization. (a) Field distribution (b) Lateral intensity scan at focal point. Transmission efficiency: **97** %.

According to the calculations for TE polarization refocusing with a homogeneous grating is impossible throughout the whole range of the investigated slab widths. However, the introduction of lateral inhomogeneities allows for refocusing even at a slab width of < 1 µm. In Fig. 7.9 the result for TE-polarization and the three-row structure with lateral inhomogeneities are depicted and show that a transmission efficiency of 70 % at a normalized spot size of 0.56 can be obtained.

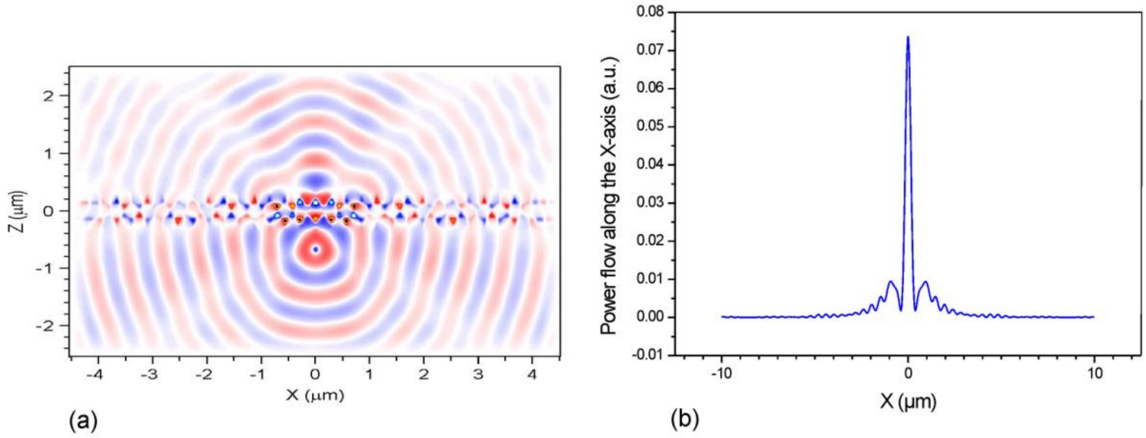

Fig. 7.9. Refocusing using a inhomogeneous triangular three-layer photonic crystal with superstructure boundary, TE polarization. (a) Field distribution (b) Lateral intensity scan at focal point. Transmission efficiency: **70** %.

7.5 3D Simulations

So far we investigated 2D-structures with the grating lattice being infinitely extended in the y-direction. In order to check the validity of the 2D results for a real 3D structure we took the 3 layer design of cylindrical air holes and incorporated it into a high-index membrane with a thickness of 0.25 µm. Such kinds of membranes are also used for resonators [HSHLKF06]. As the effective index of a membrane mode is smaller than in bulk material the wavelength of operation had to be adapted to the value of 800 nm. For better coupling from air into the waveguide, we used a short line source (0.3 µm long in *y* direction) at a distance of 0.25 µm with respect to the front of the membrane and got clear refocusing after its passage again at a distance of about 0.25 µm. The electrical field distributions both in the *x*-*z*-plane and in the *y*-*z* plane are shown in Fig. 7.10. At the refocusing point in air we got a spot size of 0.42 µm in the *x*-direction, thus, refocusing can be obtained being at least in the range of the diffraction limit. In the *y*-direction the spot size of 0.64 µm is due to beam spreading in free space.

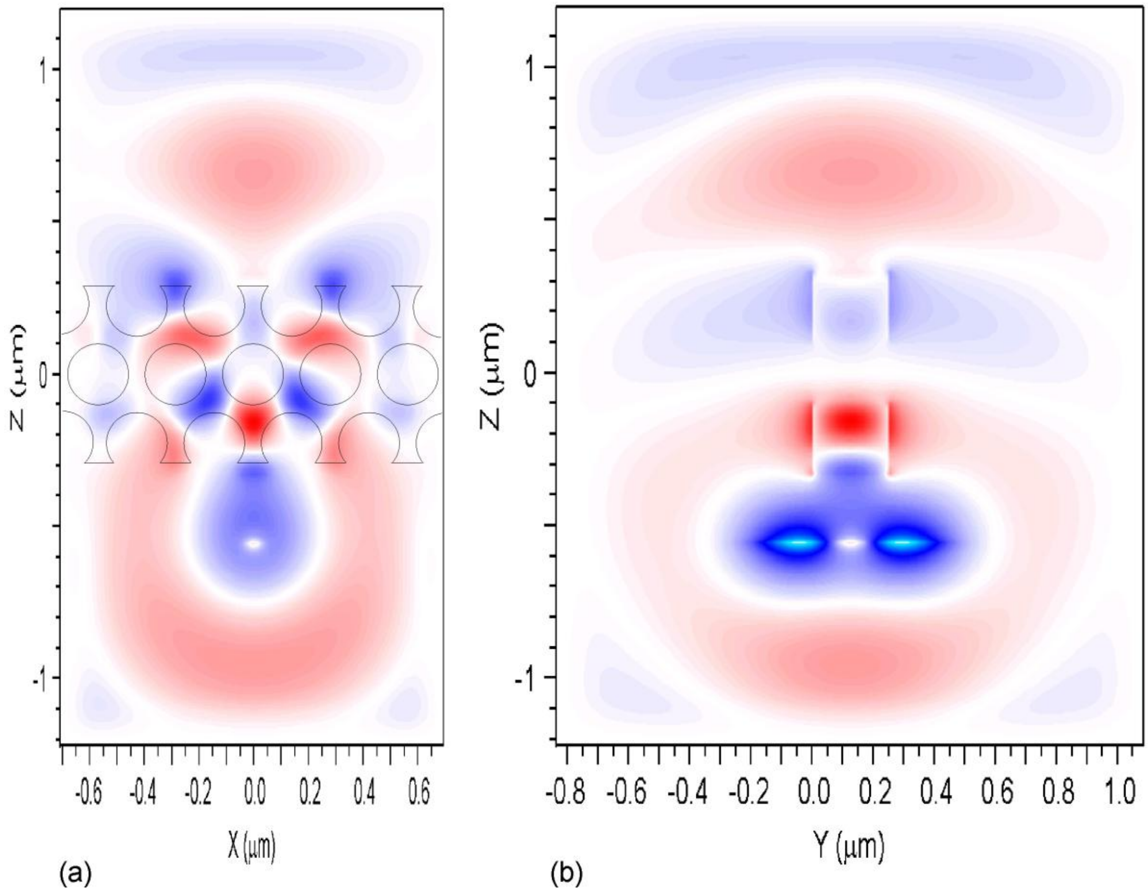

Fig. 7.10. Refocusing using a 3D photonic crystal membrane, TM polarization. Thickness of the membrane: 0.25 µm. (a) Electrical field distribution in the plane of the membrane (b) Electrical field distribution in a plane orthogonal to the membrane.

7.6 Conclusions

The highly efficient refocusing (imaging) of a point source using modified 2D triangular photonic crystal lattices with lateral inhomogeneities was investigated. Far field and near field imaging was studied starting with slab widths from 10 µm down to the sub-micron range of a truncated three-layer design. The proposed structures allow for verification of sub lambda-half resolution for nearly the whole range of slab widths. By introducing optimized lateral inhomogeneities, especially for large slab widths, the transmission efficiency can be significantly improved up to more than 90 %. The improvement in refocusing due to lateral inhomogeneities decreases with smaller slab width, however persists down to 2 µm slabs. With additional use of special superstructure boundaries, transmission efficiencies of up to 97 % were achievable especially in the cases of thin photonic crystal slabs.

Chapter 8

Compact phase-shifted photonic crystal filters with improved transmission characteristics

8.1 Introduction

Photonic crystal waveguides are attractive components for optical signal processing. Due to the achievable high refractive index contrast, photonic crystal devices can be made very small in the range of only several multiples of the used wavelengths. Concerning optical communications, various kinds of filters are needed. Regarding the implementation of optical bandpass filters two basic solutions are known: One uses a 2D photonic crystal with build-in defects to form a resonator structure [CMM03, YFSK06, PKPL05]. The other approach uses a narrow waveguide with an embedded 1D periodic structure [ZGCSR08, JPR03]. In addition to single channel filters, multichannel filters with 1D photonic crystal structures were also suggested [ZPLZW07]. It was successfully demonstrated [ZGCSR08] that hole diameter and position tapering outside and within the cavity significantly increases the optical transmission and enhances the resonance Q-factor of single-row photonic crystals embedded in photonic wire waveguide microcavities. By introducing a series of 1D periodic sections separated by phase-shift regions and by properly choosing their locations and magnitudes, a nearly rectangular shape of the bandpass transmission spectrum [ZL95] can be obtained, however, at the cost of an increased device length. Recently, a bandpass transmission filter based on 2D photonic crystals including multiple phase-shifted waveguide gratings was presented [CLLXWL07]. By means of an appropriate choice of the magnitude of the phase-shifts and the lengths of the waveguide gratings a nearly flat-top and sharp roll-off response was achieved. The amount of the phase-shifts itself was altered by introducing changes in the diameter of the border rods in the phase-shift regions.

In this thesis, a compact phase-shifted bandpass transmission filter based on 1D photonic crystal waveguides is presented. Besides the small size, special emphasis on two design criteria are given: The first is how to precisely adapt the shape of the transmission characteristic in a compact photonic crystal filter to a flat-top design, as it is not possible to get this by only changing the number of holes in a periodic section. The second criterion is how to tune the center wavelength of the filter without changing its geometry. Following these design criteria several designs of the phase-shifted regions are suggested. The various filter characteristics are calculated by numerical simulations using a 2D finite difference time domain algorithm. In order to show that the obtained design criteria are applicable for real 3D structures, results in 3D simulation are also presented.

8.2 Design of the filter structure

The initial considerations use a simple 2D filter structure build up of a narrow ridge waveguide with high lateral index contrast and equipped with a 1D photonic crystal consisting of a single row of air holes. First, the classical high-Q transmission filter design is considered [Hau84] with a single phase-shifted photonic crystal waveguide grating as depicted in Fig. 8.1. The radius of the air holes is $r = 0.2a$, with the lattice constant $a = 282.2$ nm. The dielectric medium has a refractive index of $n_d = 3.4$. A single-mode photonic crystal waveguide is formed by limiting the width of the dielectric medium to a value of 0.3 µm. For simplicity this medium is assumed to be surrounded by air on both sides. The phase-shift region is introduced by the insertion of an unmodulated waveguide region which is $0.5a$ long. This phase-shift is placed in the center of the photonic crystal waveguide grating. The lengths of two uniform grating sections around the phase-shift region are defined in units of a as $9a$. The spectral transmission characteristic is obtained using the Fourier transform of the impulse response. The impulse response itself is calculated with a 2D finite difference time domain method for TM polarization.

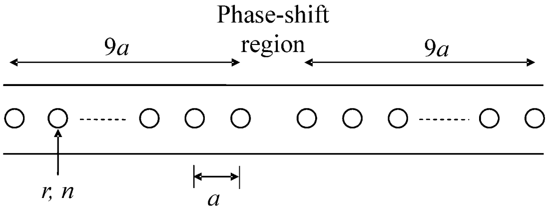

Fig. 8.1. Single phase-shifted photonic crystal waveguide grating.

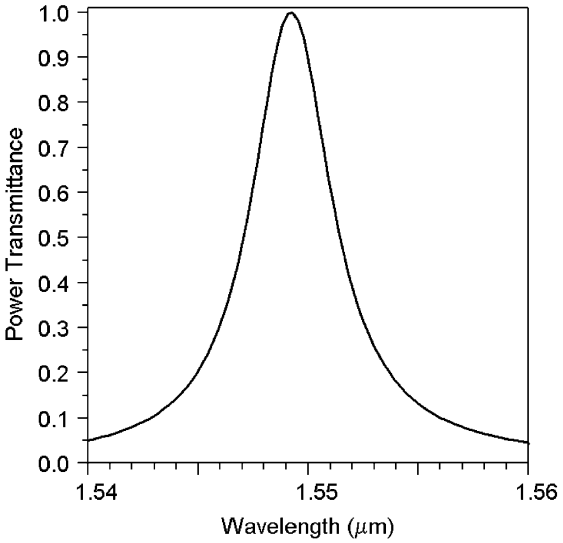

Fig. 8.2. Normalized transmission spectrum of the single phase-shifted photonic crystal waveguide grating.

Fig. 8.2 shows the calculated transmission spectrum of the photonic crystal waveguide grating with a single phase-shift. The transmission peak at the wavelength of 1549 nm is embedded in a 260 nm stop band. To analyze the performance of the proposed filter structures the bandwidth *bw* is characterized by the full width at half maximum (FWHM) value of the transmitted power. The spectral selectivity is specified by the ratio *R* between the -1 dB and the -10 dB bandwidth [ZL95]. For the single phase-shifted structure a bandwidth of *bw* = 4.3 nm and a ratio *R* of only 0.18 are obtained. Additionally, the losses connected with the filter structure are calculated by comparing the transfer characteristic of a reference waveguide without the holes with the filter transmission characteristic. For the central transmission peak the power loss remains in our 2D simulations less than 1 %.

8.3 Improvement of the transmission characteristic

For practical applications, the bandpass characteristic should have a flat-top design with good selectivity and thus a high value of the ratio *R*. In order to improve the filter characteristic of a phase-shifted grating filter multiple phase-shift sections can be introduced as presented in [ZL95]. For optimum filter performance, the lengths of the grating sections must be individually chosen [ZL95]. The disadvantage of this method is that for a high ratio *R*, the number of phase-shift regions has to be large and thus the total length of the filter structure is also increased. To maintain the compact size of the photonic crystal device, the introduction of only one additional phase-shift region is suggested as shown in Fig. 8.3.a. Three cases with the outer waveguide grating lengths of 8*a*, 9*a*, and 10*a* are investigated. The inner waveguide length is kept constant at 18*a*.

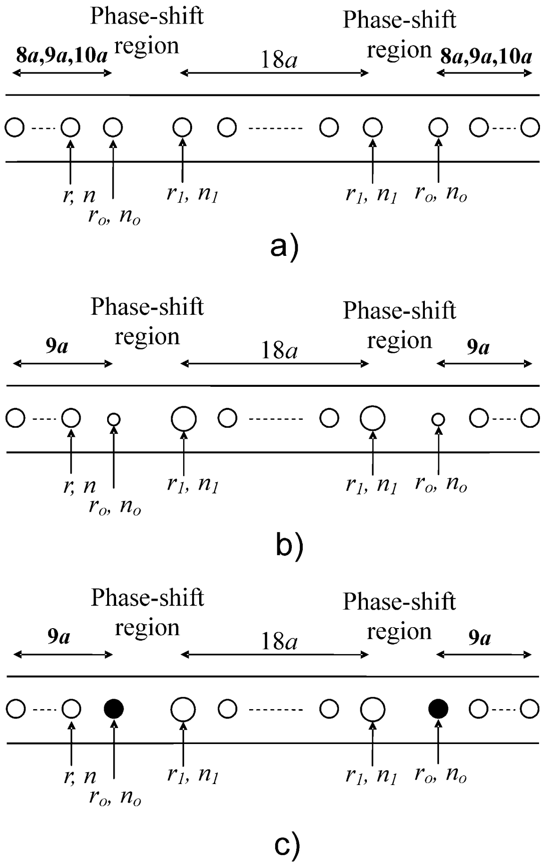

Fig. 8.3. Double phase-shifted photonic crystal waveguide grating.

(a) Initial layout with identical diameters of the holes.

(b) Improved layout with modified diameters of the holes at the phase-shift regions.

(c) Layout with both modified diameters of the holes and modified refractive index in selected holes.

As shown in Fig. 8.4, an increase of the outer waveguide grating length leads to three strongly different transmission characteristics. In the case where the outer waveguide grating length is 8*a*, a rounded shape of the transmission spectrum is obtained. A clear dip in the passband of the filter appears if the outer waveguide grating length is increased to 9*a*. This dip becomes much larger for an outer waveguide grating length of 10*a*. So, the shape of the passband can be tailored by adjusting the length of the outer waveguide gratings. Furthermore, the ratio R is increased from 0.37 to 0.56 by increasing the outer waveguide grating length from 8*a* to 10*a*. However, for all three cases, the transmission band is centered at the same wavelength of λ_c = 1549 nm.

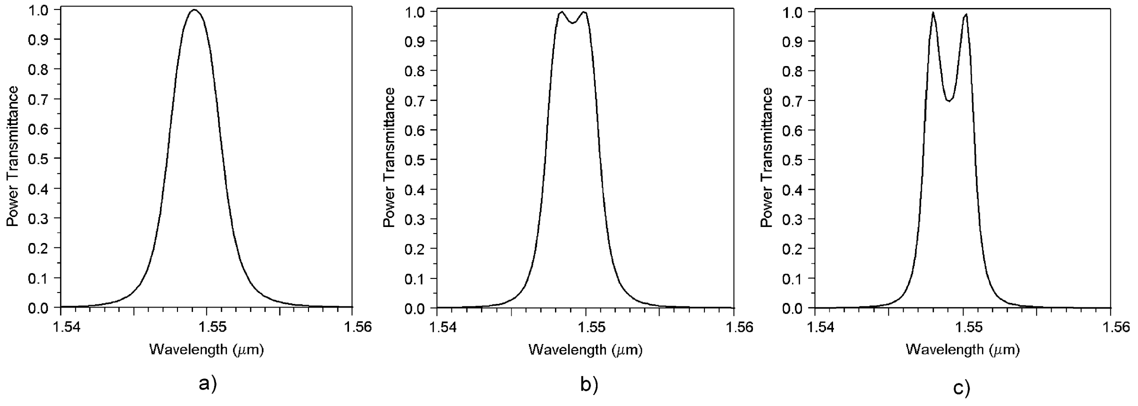

Fig. 8.4. Normalized transmission spectrum of the double phase-shifted photonic crystal waveguide grating with the outer waveguide grating lengths of 8*a* (a), 9*a* (b) and 10*a* (c). The length of the center grating is kept constant at 18*a*.

For filter applications, a flat-top transmission characteristic is prefered. In the present case, this design is "in between" a grating length of 8*a* and 9*a*. However, if we modify the homogeneous grating sections, we have only the possibility to add and drop an integer number of holes. So, another modification of the structure to get a real flat-top transmission spectrum has to be found. Several possible ways to achieve this are suggested.

One way is to use the 9*a* design and, in addition, to change simultaneously the diameters of the holes near the phase-shift regions. If the radius of the holes at the inner grating section is inceased to a value of $r_1 = 0.225a$ and the radius of the inner holes at the outer grating sections is decreased to a value of $r_0 = 0.175a$ (Fig. 8.3.b), the transmission spectrum (Fig. 8.5) describes a real flat-top characteristic at a fixed center wavelength of 1549 nm. This effect can be explained in the following way: with the use of a smaller 9th hole, the influence of coherent scattering is reduced and the resulting grating acts as a grating with reduced length. However, in order to keep the phase shift in the phase-shift regions constant and thus to maintain the center wavelength, the larger local effective index due to the smaller hole has to be compensated by a smaller local effective index resulting in an increase of r_1.

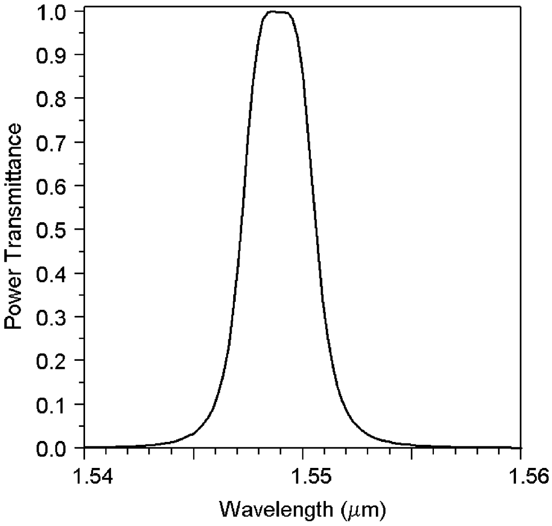

Fig. 8.5. Improved normalized transmission spectrum of the double phase-shifted photonic crystal waveguide grating by changing the diameters of the holes near the phase-shift positions: Bandwidth (FWHM): *bw* = 3.4 nm, center wavelength: λ_c = 1549 nm, ratio between -1 dB and -10 dB bandwidth: *R* = 0.42.

A nearly identical transmission characteristic as in Fig. 8.5 can be obtained by replacing the smaller holes at the phase-shift sections by holes with the original radii, however, filled with dielectric material with a refractive index of n_o = 1.7. The radii of the holes near the phase-shift region at the inner grating section are simultaneously increased to a value of $r_1 = 0.22a$ (Fig. 8.3.c).

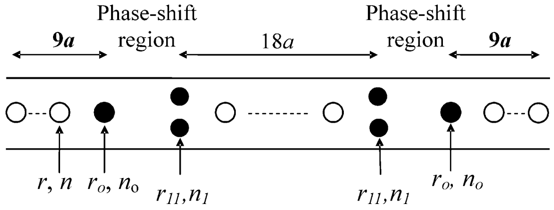

Fig. 8.6. Double phase-shifted photonic crystal waveguide grating with new design of the phase-shift region.

As a third way to get a real flat-top transmission spectrum a new design of the phase-shift region is also suggested as depicted in Fig. 8.6. The single holes in the inner periodic waveguide next to the phase shift region are replaced by double holes. First, the holes near the phase-shift region are filled with a dielectric medium with a moderate refractive index of $n_o = n_1 = 1.55$. The numerical simulations show that then a flat-top transmission spectrum remaining centered at the fixed wavelength of 1549 nm can be obtained for $r_o = 0.194a$ and $r_{11} = 0.18a$. The resulting transmission spectrum of this filter structure is presented in Fig. 8.7.a.

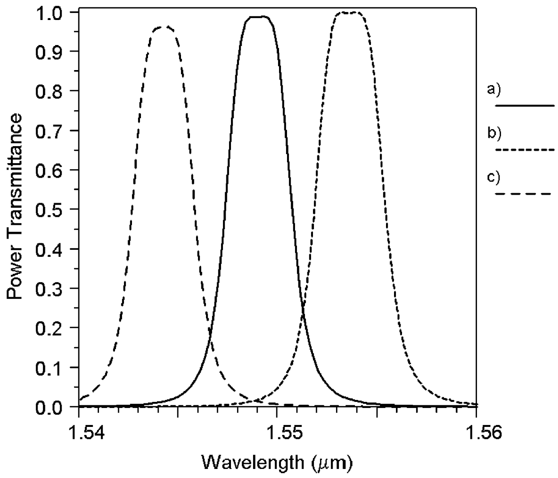

Fig. 8.7. Normalized transmission spectra of the double phase-shifted photonic crystal waveguide grating structure with $r_o = 0.194a$, $r_{11} = 0.18a$.

a) $n_o = n_1 = 1.55$. Bandwidth (FWHM): $bw = 3.5$ nm, center wavelength: $\lambda_c = 1549$ nm, ratio between -1 dB and -10 dB bandwidth: $R = 0.37$.

b) $n_o = 2.0$ $n_1 = 1.9$, $bw = 3.6$ nm, $\lambda_c = 1553.6$ nm, $R = 0.4$.

c) $n_o = n_1 = 1.0$, $bw = 3.3$ nm, $\lambda_c = 1544.4$ nm, $R = 0.41$.

In technical realizations – due to fabrication tolerances – there are always different between the original layout and the measured filter performance. So, from a practical point of view the tuning of the center wavelength without the need of geometrical changes in the filter design is to aspire. Our solution is to fill the holes at the phase-shift regions with media of modified refractive indices. For the investigations we use the structure in Fig. 8.6 because our calculations revealed that this design is best suited for tuning of the center frequency. If we take index materials with $n_o = 1.8$ and $n_1 = 1.75$, tuning of the center wavelength to +2.5 nm is possible. Tuning in the opposite direction by -2.5 nm, however, requires a low index dielectric with a refractive index $n_o = n_1 = 1.3$. If we further increase the span of the effective refractive indices of possible future artifical filling materials the tuning range is extended to +4.6 nm (for n_o = 2.0 and n_1 = 1.9) as shown in Fig. 8.7.b and to –4.6 nm (for n_o = 1.0 and n_1 = 1.0) as depicted in Fig. 8.7.c. If a small dip in the filter characteristic may be tolerated our calculations show that the tuning range to larger wavelengths can be even extended. Tuning to +10 nm by using filling materials with effective refractive indices of n_o = 2.4 and n_1 = 2.3 leads to a dip of 0.8 % in the power transmission. By filling material with effective refractive indices of n_o = 3.0 and n_1 = 2.9 a tuning to even +20 nm is possible, however, at the expense of a dip of 2.8 % and increased bandwidth of 4.5 nm. The limiting case is reached for n_o = n_1 = 3.4 with a wavelength shift of +28 nm and 5.3 % dip in the power transfer. The filter loss induced by our new design was again calculated following the previously introduced method. The loss depends slightly on the detuning and reaches its minimum at +4.6 nm with a power loss of 0.6 %. For the center frequency we got a loss of 1.6 %. The largest power loss with a value of 4 % occurred –4.6 nm away from the center frequency. So, a larger index contrast of the discontinuities in the phase-shift regions in the resonator leads to additional scattering and thus increased losses.

8.4 3D Simulations

It is not easy to change directly from approximate 2D to real 3D structure because moving to 3D structure results due to 3D scattering in a larger loss [VRLHPPCH06]. To reduce this loss, smaller radii of the air holes can be used but - due to smaller periodic modulation - at the cost of a larger bandwidth. A smaller bandwidth like in 2D simulations can only be obtained with a stronger modulation or larger radii of the air holes but then the loss is also increased and results in a change in the shape of the transmission curve. In our 2D structures, the power loss was only about 1 % or 2 % and does not affect the shape of the transmission curve.

Another difficulty in 3D simulations is the discretization. In 3D simulation, the grid size must be very carefully defined. If a large grid size is used (eg. 17 nm in z direction), the results of simulation are not reliable because they are not self consistent. For example, when the radii of the inner holes are reduced, the transmission characteristic does not change. Therefore, a grid size of 10 nm in z direction is chosen as a favourable value and gives good results.

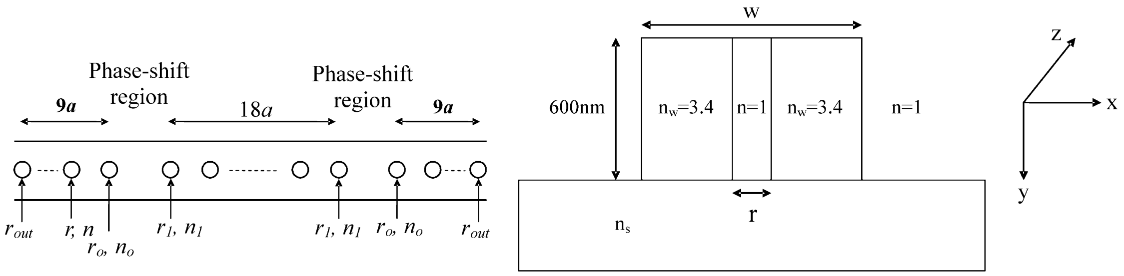

a) b)

Fig. 8.8. Double phase-shifted 3D photonic crystal waveguide grating. a) layout; b) cross-section

In this thesis, a double phase-shifted 3D photonic crystal structures (Fig. 8.8) consisting of air holes with radius of $r = 0.2a$ where $a = 282.2$ nm is a grating constant were embedded in a $w = 370$ nm wide, rectangular cross-section photonic wire with a thickness of 600 nm. A larger width of $w = 370$ nm has been chosen to reduce the loss. The number of air holes is kept at 19 at the inner grating section and 10 at the outer grating regions i.e identical to the 2D case. The spectral transmission characteristic is obtained using the Fourier transform of the impulse response. The impulse response itself is calculated with a 3D finite difference time domain method for TM polarization. A small dip in the transmission characteristic appears (Fig. 8.9.a) with the transmission efficiency of 92.2 % at the center wavelength of 1483 nm and a bandwidth of 10.4 nm, which means double of the bandwidth in the 2D simulation. The transmission efficiency of the filter structure is calculated by comparing the transfer characteristic of a reference waveguide without the holes with the filter transmission characteristic. A real flat-top transmission characteristic can be obtained by decreasing the radii of the two holes near the phase-shift regions to a value of $r_1 = r_0 = 0.19a$ (Fig. 8.9.b). In this case, the transmission efficiency is increased to 95.3 % and the bandwidth is kept at 10.5 nm. If the radii of the two holes near the phase-shift regions is further reduced to a value of r_1

= r_0 = 0.185*a* (Fig. 8.9.c), the transmission efficiency can reach 96.4 % and the shape of the transmission characteristic shows no longer a flat-top but has a small-dip.

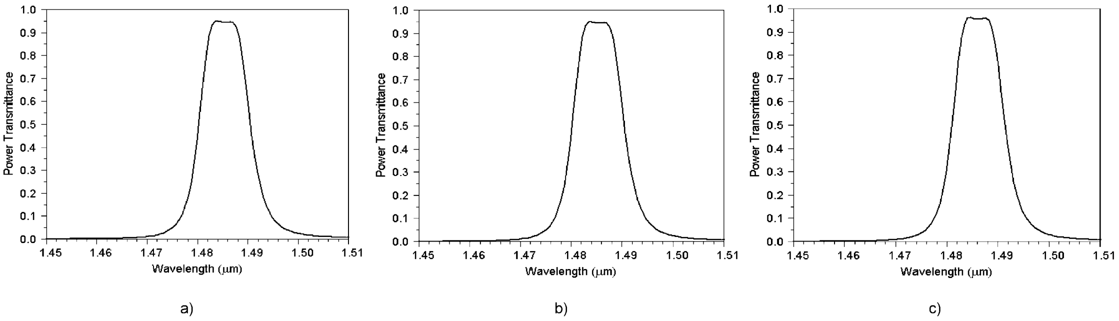

Fig. 8.9. Normalized transmission spectra of the double phase-shifted 3D photonic crystal waveguide grating structure with r = 0.2*a*:

(a) radii of two holes near the phase-shifted region: r_1 = r_0 = 0.2*a*.

(b) r_1 = r_0 = 0.19*a*.

(c) r_1 = r_0 = 0.185*a*.

The bandwidth of the filter can be reduced by increasing the radii of the air holes but at the cost of reducing the transmission efficiency. A bandwidth of about 6.4 nm can be obtained by increasing all radii of the air holes to a value of r = 0.23*a* and the transmission efficiency is then reduced to 73.6 %. By reducing the radii of two holes near the phase-shift region to r_1 = r_0 = 0.21*a*, the transmission efficiency can be improved to 85.2 %. This effect can be explained by reduced mismatch of the propagating waves due to "tapering" [ZGCSR08, SLLH04].

If the periodic modulation is further increased (r = 0.26*a*) and the width of the photonic wire is simultaneously altered to w = 350 nm, the bandwidth of the filter can be strongly reduced to 3.1 nm, however, the shape of the transmission curve is changed from a flat-top to a round shape with the transmission efficiency of only 26.6 % (Fig. 8.10.a). A nearly flat-top transmission characteristic can now be obtained by two simultaneous methods: a different reduction of the radii of the two holes near the phase-shift regions to r_1 = 0.185*a*, r_0 = 0.165*a* and a reduction of the radii of holes at the outermost grating sections to $r_{out} = 0.16a$. The bandwidth is now 4.3 nm and the transmission efficiency is increased to 91.2 % (Fig. 8.10.b). The transmission efficiency can be further improved up to 98.9 % (Fig. 8.10.c) if we fill the two holes near the phase-shift regions with a dielectric with a refractive index of $n_1 = n_0 = 1.9$. The bandwidth is now increasing to 4.8 nm and there is a small dip in the transmission curve.

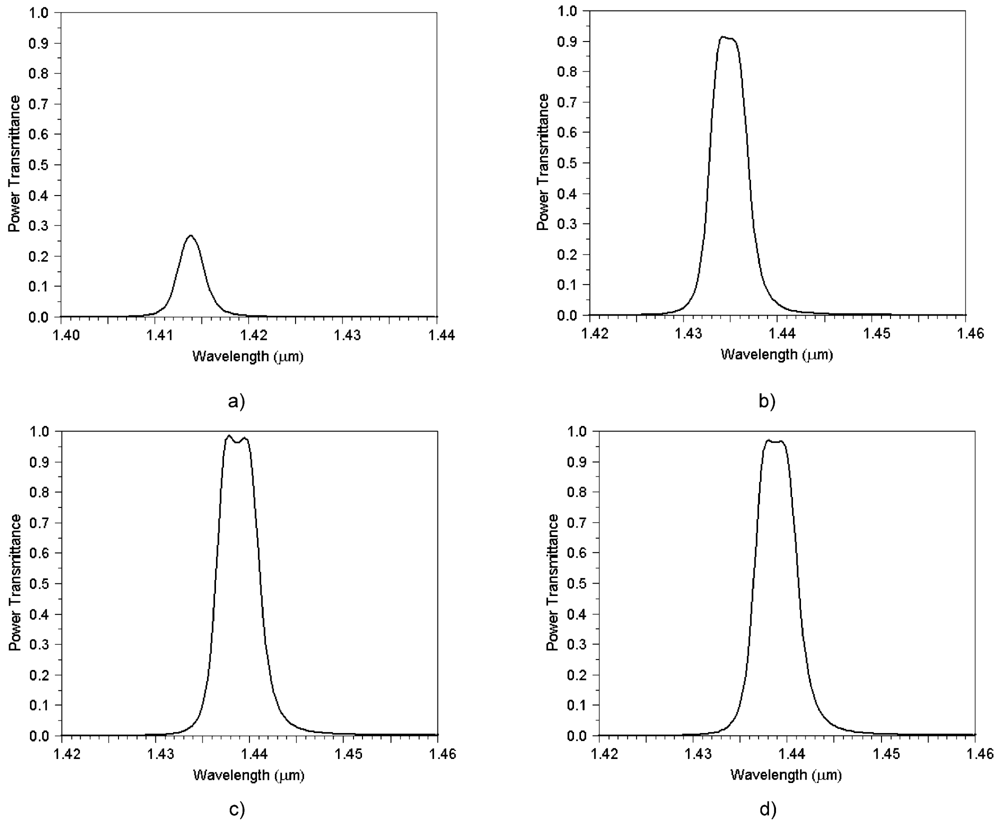

a) b) c) d)

Fig. 10. Normalized transmission spectra of the double phase-shifted 3D photonic crystal waveguide grating structure with $w = 350$ nm:

(a) $r = 0.26a$.

(b) $r = 0.26a$, $r_1 = 0.185a$, $r_0 = 0.165a$, $r_{out} = 0.16a$.

c) $r = 0.26a$, $r_1 = 0.185a$, $r_0 = 0.165a$, $r_{out} = 0.16a$, $n_1 = n_0 = 1.9$.

d) $r = 0.26a$, $r_1 = 0.185a$, $r_0 = 0.165a$, $r_{out} = 0.12a$, $n_1 = n_0 = 1.9$.

By reducing the outermost radii of the holes to $r_{out} = 0.12a$, the dip in the transmission curve is reduced and results in the improvement in the shape of the transmission curve to a flat-top design (Fig. 8.10.d) [JPR04]. The bandwidth is now 4.9 nm and the transmission efficiency slightly decreases to 97.1 %. To summarize, one can see clearly that the simultaneous reduction tapering of the radii of the two holes near the phase-shift regions has a significant effect on the reduction of the losses (Fig. 8.10 a,b).

To check the tunabilty of the center wavelength by filling the holes at the phase-shift regions with media of modified refractive indices, we use double phase-shifted 3D photonic crystal structures (Fig. 8.8) consisting of air holes with radii of $r = 0.26a$, the two holes near the phase-shift region with radii of $r_1 = 0.185a$, $r_0 = 0.165a$. The radii of holes at the outermost of the grating sections are $r_{out} = 0.12a$ and the width of the photonic wire is $w = 350$ nm. The holes near the phase-shift region are filled with a dielectric medium with a moderate refractive index of $n_o = n_1 = 1.65$ (Fig. 8.11.a). Simulation results show that tuning of the center wavelength to +2.4 nm is possible if we take index materials with $n_o = n_1 = 2.1$ (Fig. 8.11.b). Tuning in the opposite direction, however, requires a low index dielectric. Tuning by -2.4 nm is possible with a refractive index $n_o = n_1 = 1.1$ (Fig. 8.11.c).

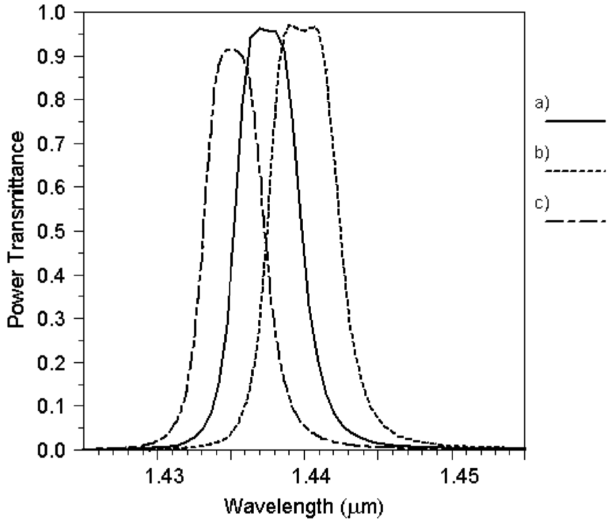

Fig. 8.11. Normalized transmission spectra of the double phase-shifted 3D photonic crystal waveguide grating structure: $r = 0.26a$, $r_1 = 0.185a$, $r_0 = 0.165a$, $r_{out} = 0.12a$, $w = 350$ nm.

a) $n_o = n_1 = 1.65$, $bw = 4.7$ nm, $\lambda_c = 1437.5$ nm, $R = 0.42$.

b) $n_o = n_1 = 2.1$, $bw = 5$ nm, $\lambda_c = 1439.9$ nm, $R = 0.44$.

c) $n_o = n_1 = 1.1$, $bw = 4.4$ nm, $\lambda_c = 1435.1$ nm, $R = 0.41$.

8.5 Conclusions

A compact double phase-shifted photonic crystal waveguide bandpass filter is investigated with respect to the two design criteria of adapting the shape of the transmission characteristic in short filters and by tuning the center of the transmission band without changes in the geometry of the structure. Several designs of the phase-shifted region are proposed to get real flat-top transmission spectra. Tunability of the center wavelength in both directions of at least ±4.6 nm is obtained by filling the holes near the phase-shifted regions with dielectrics of different refractive indices. Moving to 3D simulation causes some difficulties because of the problem of loss due to radiation. The loss is reduced by simultaneously decreasing the radii of the two holes near the phase-shifted regions. Simulations show that a flat-top transmission characteristic can be obtained also in the 3D structure with the transmission efficiency of about 97.1 %.

The tunability of the center wavelength is also possible by filling the holes near the phase-shifted regions with dielectrics of different refractive indices. In 3D simulations, there is a difficulty in chooing the discretization. So, the grid size must be very carefully defined. If a large grid size is used (eg. 17 nm in *z*-direction), the results of simulation are not reliable because they are not self consistent. For example, when the radii of the inner holes are reduced, the transmission characteristic does not change. Therefore, a grid size of 10 nm in z direction is chosen as a favourable value and gives good results.

Chapter 9

Summaries

9.1 English

Photonic crystals are inhomogeneous dielectric media with periodic variation of the refractive index. A photonic crystal gives us new tools for the manipulation of photons and thus has received great interests in a variety of fields. Photonic crystals are expected to be used in novel optical devices such as thresholdless laser diodes, single-mode light emitting diodes, small waveguides with low-loss sharp bends, small prisms, and small integrated optical circuits. They can be operated in some aspects as "left handed materials" which are capable of focusing transmitted waves into a sub-wavelength spot due to negative refraction.

The thesis is focused on the applications of photonic crystals in communications and optical imaging:

- Photonic crystal structures for potential dispersion management in optical telecommunication systems

- 2D non-uniform photonic crystal waveguides with a square lattice for wide-angle beam refocusing using negative refraction

- 2D non-uniform photonic crystal slabs with triangular lattice for all-angle beam refocusing

- Compact phase-shifted band-pass transmission filter based on photonic crystals

For applications of photonic crystals in new or improved functional components used for communications, several unique properties which may be of special interest are investigated: spatial and chromatic dispersion as well as anomalous refraction phenomena. Especially the strong angular difference between phase and group velocity in the vicinity of an optical bandgap may be used in practical devices. These strongly frequency dependent beam-steering effects were demonstrated by Zengerle decades before and they may now be interesting for spatial optical frequency discrimination and thus also for dispersion compensation or pulse shaping. Photonic crystals can be used as a means to compensate for chromatic dispersion by potential dispersion management in optical telecommunication systems. For adaptive dispersion management, one can profit from the combined effect of spatial and chromatic dispersion. Here, the strong dispersion in the vicinity of an optical bandgap is used. The thesis demonstrates the principle of adaptive dispersion compensation using one dimensional photonic crystal planar waveguides consisting of vertical slices inclined at an angle of 45 degrees with respect to the straight boundaries. The structure in this thesis can be used for compensation of tolerances of the required fiber lengths in ultrahigh-speed signal transmission. Adaptive dispersion compensation is done by turning the photonic crystal structures in a range of +/-2 degrees around an inclination angle of 2 degrees. In the case of a reversed dispersion fiber (RDF) a tolerance in the fiber length of 10 m can be compensated.

On the other side, photonic crystals also have applications in imaging. A number of imaging principles were demonstrated in the past, however, for potential applications they have to be combined with efficiency. One part of this thesis is focused on the wide-angle beam refocusing using negative refraction in non-uniform 2D square photonic crystal waveguides. Here, the two major problems are solved: the reduction of reflection losses due to mismatch at the boundaries of the photonic crystal slabs and to find a solution of the inherent problem that the real shape of the dispersion contours of a homogeneous photonic crystal usually causes significant aberrations at high NA. To reduce the reflection problem, gradual (tapered) transitions will be used. The reflection loss can then be significantly reduced with respect to a step-transition up to angles of incidence of 35 degrees. For a smaller angular range almost vanishing reflection can be achieved. For solving the problem of precise imaging, an inhomogeneous photonic crystal structure is introduced, with a non-uniform background refractive index of the still homogeneous grating itself in order to get additional degrees of freedom for design. Using the introduced new form of local dispersion engineering we were able - in a first step of optimization - to improve the refocusing efficiency to 90 % for a 1.6 µm wide Gaussian beam launched in air. At least 85 % for refocusing of a 0.8 µm wide Gaussian beam in homogeneous media with a refractive index of 2.0 are possible. Compared to a value of less than 20 % for a homogeneous photonic crystal structure with step-like transitions, this is an enormous progress in giving design rules for efficient practical applications of photonic crystal lenses.

High resolution imaging is also possible in 2D triangular photonic crystal slabs. In this thesis we mainly investigate the all-angle beam refocusing in non-uniform triangular photonic crystals. The highly efficient refocusing (imaging) of a point source using modified 2D triangular photonic crystal lattices with lateral inhomogeneities is presented. Far field and near field imaging was studied starting with slab widths from 10µm down to the sub-micron range of a truncated three-layer design. Clearly improved far-field imaging properties in comparision to a square lattice were otained. The proposed structures allow for verification of sub lambda-half resolution for nearly the whole range of slab widths. By introducing optimized lateral inhomogeneities, especially for large slabwidths, the transmission efficiency can be significantly improved up to more than 90 %. The improvement in refocusing due to lateral inhomogeneities decreases with smaller slab width however persists down to 2 µm slabs. With additional use of the special super-structure boundaries, the wide-angle reflection loss due to mismatch at the boundaries of the PhC slab is further reduced and transmission efficiencies of up to 97 % were achievable especially in the cases of thin photonic crystal slabs. In order to check the validity of the 2D results for a real 3D structure, we took a 3 layer design of cylindrical air holes and incorporated it into a high-index membrane with a thickness of 0.25 µm. As the effective index of a membrane mode is smaller than in bulk material the wavelength of operation had to be adapted to the value of 800 nm. For better coupling from air into the waveguide, we used a short line source (0.3 µm long in y direction) at a distance of 0.25 µm with respect to the front of the membrane and got a clear refocusing after its passage again at a distance of about 0.25 µm. At the refocusing point in air we got a spot size of 0.42 µm in the *x*-direction, thus, refocusing can be obtained being at least in the range of the diffraction limit. In the *y*-direction the spot size of 0.64 µm is due to beam spreading in free space.

Photonic crystal waveguides are also attractive components for optical signal processing. Concerning optical communications, various kinds of frequency filters are needed. Due to the achievable high refractive index contrast, photonic crystal devices can be made very small in the range of only several multiples of the used wavelengths.

In this thesis, a compact phase-shifted bandpass transmission filter based on 1D photonic crystal waveguides is presented. Besides the small size, special emphasis on two design criteria are given: The first is how to precisely adapt the shape of the transmission characteristic in a compact photonic crystal filter to a flat-top design, as it is not possible to get this by only changing the number of holes in a periodic section. The second criterion is how to tune the center wavelength of the filter without changing its geometry. Following these criteria several designs of the phase-shifted region are proposed to get real flat-top transmission spectra. Tunability of the center wavelength in both directions of at least ±4.6 nm is obtained by filling the holes near the phase-shifted regions with dielectrics of different refractive indices. The various filter characteristics are calculated by numerical simulations using a 2D finite difference time domain algorithm. In order to show that the obtained design criteria are applicable for real 3D structures, results in 3D simulation are also presented. Moving to 3D simulation causes some difficulties because of the problem of loss due to radiation. To reduce this loss, smaller radii of the air holes can be used but - due to smaller periodic modulation - at the cost of a larger bandwidth. A smaller bandwidth like in 2D simulations can only be obtained with a stronger modulation or larger radii of the air holes but then the loss is also increased and results in a change in the shape of the transmission curve. In our 2D structures, the power loss was only about 1 % or 2 % and does not affect the shape of the transmission curve. The loss is further reduced by simultaneously decreasing the radii of the two holes near the phase-shifted regions. Simulations show that a flat-top transmission characteristic can be obtained also in the 3D structure with the transmission efficiency of about 97.1 %. The tunability of the center wavelength is also possible by filling the holes near the phase-shifted regions with dielectrics of different refractive indices. In 3D simulations, there is a difficulty in chooing the discretization. So, the grid size must be very carefully defined. If a large grid size is used (eg. 17 nm in *z* direction), the results of simulation are not reliable because they are not self consistent. For example, when the radii of the inner holes are reduced, the transmission characteristic does not change. Therefore, a grid size of 10 nm in z direction is chosen as a favourable value and gives good results.

9.2 Deutsch

Photonische Kristalle sind inhomogene dielektrische Materialien mit periodischer Schwankung des Brechungskoeffizienten. Ein photonischer Kristall gibt uns neue Möglichkeiten zur optischen Informationsverarbeitung. Von photonischen Kristallen wird erwartet, dass sie in neuen optischen Komponenten wie "schwellenlosen" Laserdioden, einwelligen lichtemittierenden Dioden, kleinen Wellenleitern mit dämpfungsarmer scharfer Biegung, kleinen Prismen und integrierten optischen Schaltungen benutzt werden. Sie können in einigen Aspekten auch wie "linkshändige Materialien" wirken, welche zur Fokussierung sich ausbreitender Wellen mit einer Auflösung im Subwellenlängenbereich aufgrund negativer Brechung verwendet werden können.

In dieser Arbeit werden insbesondere Anwendungen photonischer Kristalle in der Kommunikation und bei der optischen Abbildung betrachtet:

- Photonische Kristallstrukturen für mögliches Dispersionsmanagement in optischen Telekommunikationssystemen.

- Zweidimensionale inhomogene photonische Kristallwellenleiter mit quadratischer Gitterstruktur zur Strahl-Refokussierung bei hoher Winkeldivergenz unter Verwendung der negativen Brechung.

- Zweidimensionale inhomogene photonische Kristallstrukturen mit dreiecksförmiger Gitterstruktur zur Strahlrefokussierung über den gesamten Emission-Winkelbereich.

- Kompakte Bandpass-Transmissionsfilter, basierend auf phasenverschobenen eindimensionalen photonischen Kristallwellenleitern

Für die Anwendungen der photonischen Kristalle in neuen oder verbesserten Funktions-Komponenten in der optischen Kommunikation werden einige einzigartige Eigenschaften untersucht, die von spezielle Interesse sein können: Räumliche und chromatische Dispersion sowie ungewöhnliche Brechungsphänomene. Insbesondere kann der starke Unterschied in der Ausbreitungsrichtung zwischen Phasen- und Gruppengeschwindigkeit in der Nähe eines optischen Sperrbandes in praktischen Komponenten verwendet werden. Diese stark frequenzabhängigen Effekte wurden von Zengerle Jahrzehnte vorher demonstriert und können jetzt interessant für die Dispersionskompensation, die Pulsformung und die optische Abbildung sein. Photonische Kristalle können als Komponenten zur Kompensation der chromatischen Dispersion in optischen Telekommunikationssystemen benutzt werden. Für adaptives Dispersionsmanagement kann man insbesondere vom kombinierten Effekt der starken räumlichen und chromatischen Dispersion profitieren. Auch hier wird die starke Dispersion in der Nähe einer optischen Bandlücke benutzt. In dieser Arbeit wird das Prinzip der adaptiven Dispersionskompensation unter Verwendung von einfach periodischen photonischen planaren Kristallwellenleitern gezeigt, die aus einer Gitterstruktur bestehen, die schräg in einem Winkel von 45^0 in Bezug auf die Einstrahlungsrichtung geneigt ist. Die Struktur in dieser Arbeit kann zur Kompensation von Toleranzen der erforderlichen Faserlängen im Bereich der Ultrahochgeschwindigkeitssignalübertragung genutzt werden. Adaptive Dispersionskompensation erfolgt, indem man die Orientierung der photonische

Kristallstruktur in einem mikrooptischen System um +/-2 Grad bei einem Neigungwinkel von 2 Grad verändert. Bei einer Bitrate von 640 Gbit/sec können Längenvariation der mit verwendeten Dispersionskompensationsfaser im Bereich von 421 m bis 431 m ausgeglichen werden.

Auf der anderen Seite haben photonische Kristalle auch attraktive Anwendungsmöglichkeiten im Bereich der optischen Abbildungen. Einige neuartige Abbildungsverfahren wurden bereits in der Vergangenheit im Hinblick auf potentielle Anwendungen untersucht, zusätzlich ist aber auch die Transmissioneffizienz zu maximieren. In dieser Arbeit wird zunächst die Weitwinkel-Lichtstrahlsrefokussierung betrachtet, und zwar unter Verwendung der negativen Brechung in einem inhomogenen photonischen Kristallwellenleiter mit quadratischer Kristallstruktur. Dazu werden die Resultate einer theoretischen Studie mit dem Hauptziel der effizienten Fernfeldabbildung (Refokussierung) eines stark divergenten (hohe NA) Gaußschen Wellenbündels vorgestellt. Hierbei werden die zwei Hauptschwierigkeiten gelöst: Die Verkleinerung der Reflexionsverluste wegen der Fehlanpassung an den Grenzen der photonischen Kristallwellenleiter, und eine Lösung des inhärenten Problems, dass die reale Form der Dispersionskurven eines homogenen photonischen Kristalles normalerweise starke Verzerrungen in der optischen Abbildung bei hoher NA verursacht. Um das Reflexionsproblem zu verringern, werden graduelle Übergänge verwendet. Der Reflexionsverlust kann dann in Bezug auf einen Stufen-Übergang bis zu Einfallswinkeln von 35^0 erheblich verringert werden. Für kleinere Winkelbereiche kann sogar fast verschwindende Reflexion erzielt werden. Für das Lösen des Problems einer exakten Abbildung wird eine nicht homogene photonische Kristallstruktur mit einem ortsvarianten Hintergrundbrechungskoeffizienten - bei sonst homogenen Kristallgitter - eingeführt, um zusätzliche Freiheitsgrade für den Entwurf zu erhalten. Unter Verwendung der eingeführten neuen Form der lokalen räumlichen Dispersionskompensation waren wir - in einem ersten Schritt der Optimierung – in der Lage, die Refokussierungseffizienz für einen 1.6 µm breiten Gaußschen Lichtstrahl der Wellenslänge 1345 nm der in Luft emittiert wurde auf bis 90 % zu verbessern. Eine Refokussierungseffizienz von wenigstens 85 % bei einem 0.8 µm breiten Gaußschen Lichtstrahl für einen photonischen Kristall möglich, der in einem homogenen

Dielektrikum mit einem Brechungskoeffizienten von 2.0 eingebettet ist. Verglichen mit einer Effizienz von weniger als 20 % für eine homogene photonische Kristallstruktur mit Stufen-Übergängen ist dies ein erheblicher Fortschritt in der Entwicklung von Entwurfsrichtlinien für praktische Anwendungen photonischer Kristallslinsen.

Abbildungen mit hoher Auflösung lassen sich auch in zweidimensionalen Photonischen Kristallen mit Dreiecks-Kristallgitter realisieren. In dieser Arbeit wird hierzu die Vollwinkel- Lichtstrahl-Refokussierung in lateral inhomogenen photonischen Kristallen betrachtet. Die Fernfeld- und Nahfeld-Abbildung wurde beginnend mit einer Kristalldicke von 10 µm bis zu einer Dicke im Submikronbereich untersucht. Die vorgeschlagenen Strukturen lassen Auflösungen im Bereich der halben Wellenlänge für nahezu alle untersuchten Kristalldicken zu. Mit Hilfe einer optimierten seitlichen Inhomogenität kann die Transmissionseffizienz, besonders für große Kristalldicken, bis zu erheblich mehr als 90 % verbessert werden. Die Verbesserung bei der Refokussierung infolge der seitlichen Inhomogenität, sinkt mit kleinerer Kristalldicke ist aber bis herunter zu einer Dicke von 2 µm vorhanden. Bei zusätzlichem Gebrauch von speziellen Superstruktur-Übergängen werden die Reflexionsverluste infolge der Fehlanpassung an den Grenzen des photonischen Kristalls weiter verringert, und führen zu einer Transmissionseffizienz von bis zu 97 %, insbesondere bei dünnen Photonischen Kristallen. Um die Gültigkeit zweidimensionaler Resultate anhand einer realen dreidimensionalen Struktur zu überprüfen, nahmen wir einen Fall mit zylinderförmigen Luftlöchern in einer Hochindex-Membrane mit einer Dicke von 0.25 µm an. Da der effektive Index eines Membranenmodus kleiner als im 2D Kristall ist, mussten wir die Betriebswellenlänge auf einen Wert von 800 nm reduzieren. Für eine bessere Kopplung in den Wellenleiter benutzten wir eine kurze Linienquelle (0.3 µm lang in der *y*-Richtung) in einem Abstand von 0.25 µm in Bezug auf die Frontseite der Membrane und erhielten eine klare Refokussierung nach Durchquerung der Membranstruktur wieder in einem Abstand von ungefähr 0.25 µm. Im Refokussierungspunkt erhielten wir eine Strahltaille von 0.42 µm in der *x*-Richtung, so dass in der Kristallebene eine Refokussierung im Bereich der Beugungsgrenze auch im dreidimensionalen Fall erreicht werden kann. In der *y*-Richtung hat der Fokus eine Ausdehnung von 0.64 µm, bedingt durch die Lichtausbreitung im freien Raum.

Photonische Kristallwellenleiter sind auch attraktive Komponenten für die optische Signalverarbeitung. Im Bereich der optischen Kommunikation sind verschiedene Arten von Filtern erforderlich. Wegen des hohen erreichbaren Brechungszahl-Kontrastes können hier Photonische Kristall-Strukturen mit Abmaβen von nur wenigen Vielfachen der verwendeten Wellenlängen hergestellt werden.

In dieser Arbeit wird ein kompaktes Bandpass-Transmissionsfilter, das auf eindimensionalen phasenverschobenes photonischen Kristallwellenleitern basiert, entworfen. Außer der kleinen Größe wird besondere Betonung auf zwei Entwurfskriterien gelegt: Das erste ist ein flacher Verlauf der Transmissionscharakteristik im Durchlassband. Das zweite Kriterium ist, die Abstimmung der Mittenwellenlänge des Filters, ohne dessen Geometrie zu ändern. Basierend auf diesen Kriterien werden einige Entwürfe für phasenverschobene Gitterbereiche vorgeschlagen. Eine Änderung der Mittenwellenlänge von mindestens ±4.6 nm wird erreicht, indem die Löcher nahe den phasenverschobenen Regionen mit Dielektrika mit verschiedenen Brechungskoeffizienten gefüllt werden. Verschiedene Filtercharakteristiken werden durch numerische Simulationen unter Verwendung eines zweidimensionalen FDTD Algorithmus berechnet. In unseren zweidimensionalen Strukturen war der Leistungsabfall im Transmissionsband nur ungefähr 1 % oder 2 %. Um zu zeigen, dass die erreichten Entwurfskriterien für reale dreidimensionale Strukturen anwendbar sind, werden auch einige Resultate der dreidimensionalen Simulation gezeigt. Eine dreidimensionale Simulation offenbart zusätzliche Verlustprobleme. Um diese Verluste zu verringern, können kleinere Radien der Luftlöcher, aber - wegen der kleineren periodischen Modulation - auf Kosten einer größeren Bandbreite, benutzt werden. Eine kleinere Bandbreite wie in zweidimensionalen Simulationen kann mit einer stärkeren Modulation oder einem größeren Radius der Luftlöcher erhalten werden. Die dann im 3D-Fall auftrettenden Verluste können wieder verringert werden, wenn der Radius der beiden Löcher nahe den phasenverschobenen Regionen gleichzeitig reduziert wird. Simulationen zeigen, dass ein flaches Maximum der Transmission in der dreidimensionalen Struktur mit einer Transmissionseffizienz von ungefähr 97.1 % bei einer Transmissionsbandbreite von 4.9

nm erreicht werden kann. Die Änderung der Mittenwellenlänge der dreidimensionalen Struktur ist auch möglich, indem die Löcher nahe den phasenverschobenen Regionen mit Dielektrika unterschiedlicher Brechungskoeffizienten gefüllt werden. In den dreidimensionalen Simulationen muss die Größe des Simulationsgitters sehr sorgfältig definiert werden, da sonst widersprüchliche Ergebnisse entstehen. Eine Große des numerischen Simulationsgitters von nur 10 nm in *z*-Richtung erwies sich hier als vorteilhaft.

Appendix

A.1 Transmission characteristic calculated by Fourier Transform of the Impulse Response

Given is an impulse excitation:

$$\phi(r,t) = f(x,y)\cdot h(z)\cdot \delta(t_0) \tag{A.1.1}$$

Where: *f(x,y)* is the spatial distribution in *x* and *y*
h(z) is the spatial distribution in *z*
$\delta(t_0)$ is the delta function

An impulse excitation is normally only used for a cavity mode calculation, and results predominantly in a forward traveling wave. It has a different meaning than other excitation types: it sets an initial field pattern at $t = 0$, then lets it propagate for $t > 0$ without any further driving of the field.

This impulse propagates through the structure and the power is measured by a time monitor at the output side of the structure. The data obtained by time monitor are then processed by frequency analysis.

Frequency analysis can be expressed as a Fourier sum which is based on a discretized Fourier Transform evaluated over a finite domain. The Fourier sum evaluated is:

$$\tilde{\phi}(r,\omega) = \alpha \cdot \sum_{t=0}^{ts} \phi(r,t)\cdot e^{i\omega t} \cdot dt \tag{A.1.2}$$

Where $\phi(r,t)$ are the data produced by the time monitor and
ts is the simulation stop time
ω is frequency

α is the normalization factor

For the "Fast Fourier Transform" (FFT) frequency analysis, the Fourier sum is calculated at the end of the simulation. The complete time response of the time monitor is recorded, and the above sum can be regarded as post-processing.

In Fourier transform of the time based systems, both the sampling rate and the total number of points sampled have an important effect. So, frequency resolution δf is given by:

$$\delta f = \frac{1}{T_0} = \frac{1}{N\delta t} \qquad \text{(A.1.3)}$$

Where: δt is the sampling rate in time

N is the total number of points sampled and is always an integer

T_0 is the total length of time domain data and is equal to $N \cdot \delta t$

The above result shows that the greater the total length of time domain data T_0, the better the frequency resolution.

It is important that N, the number of time domain points, be equal to power of two. The easiest way to do is to set the stop time equal to $2^P \cdot$*fdtd_monitor_time* where P is an integer, N is equal to 2^P and *fdtd_monitor_time* is the built in variable for the monitor time (and is identified to the *fdtd_time_step*). If N is not a power of two, the FFT will compute the frequency response for the closest power of two that is less than N, resulting in an inefficient calculation.

Data will be output with a frequency resolution given by δf defined above. To increase this resolution, the length of time data, T_0, must increase. This can simply be done by increasing the stop time and thus by increasing the value of integer P described above.

In case when the field has diminished to zero after a certain period of time, there will be no more information to gain by continuing propagation. The padding factor ($2^{(N-1)}$)

combats this difficulty by padding the time monitor response with zeros before performing the FFT analysis to obtain higher resolution.

In our calculation, we set the stop time equal to $2^{18} \cdot fdtd\_time\_step$ and the padding factor equal to 4 to get the acceptable frequency resolution.

A.2 Average of the transmitted power

In the case where the launch type is "point source" and, as the power flow is not constant during one period, it is needed to measure the transmitted power by averaging it over one period. Here, the power flow at cT is the same as the power flow at $cT+\lambda$ where λ is the free space wavelength. In all simulations, all time values must be specified as cT in units of µm, where c is the speed of light in vacuum.

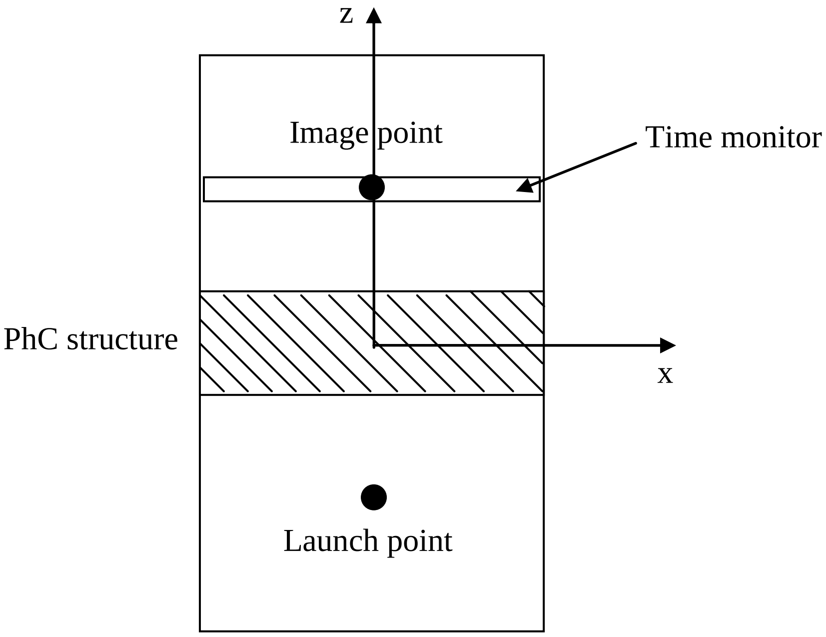

Fig. A. 2. 1. Layout of the numerical experiment

The time monitor is placed at the image position to measure the transmitted power. In order to get the necessary precision, a period λ is divided into 20 subsections, that means the stop time of simulation cT is divided into $cT/(\lambda/20)$ slice times. The time steps are set as a multiple of $\lambda/20$ so that they fulfill the convergence condition (the Courant condition which relates the spatial and temporal step size $c\Delta t < \frac{1}{\sqrt{\left(\frac{1}{\Delta x^2}+\frac{1}{\Delta y^2}+\frac{1}{\Delta z^2}\right)}}$) to obtain a stable simulation. The simulation calculates the power flow at all slice times $\lambda/20$, $2\cdot\lambda/20$, $3\cdot\lambda/20, \ldots cT$ (cT is chosen as the multiple of $\lambda/20$).

The 20 last data files of the power flow through the time monitor (at the 20 last slice times) are used. So the transmitted power at position x is then averaged as:

$$P_{avg}(x) = \frac{1}{20}\sum_{i=1}^{20} P_i(x) \tag{A.2.1}$$

$P_{avg}(x)$: average transmitted power at position x

$P_i(x)$: transmitted power at each slice time i in one period λ

The total power flow across the time monitor is then integrated along the x-axis:

$$P_{total} = \sum_{i=0}^{n} P_{avg}(x_i)\cdot(x_{i+1} - x_i)\cdot \tag{A.2.2}$$

The procedure to average the transmitted power and to integrate the average transmitted power is done by writing a program in visual C++

A.3 Calculation of the group velocity in a 1D photonic crystal structure

The layout of the numerical experiment is shown in Fig.A.3.1:

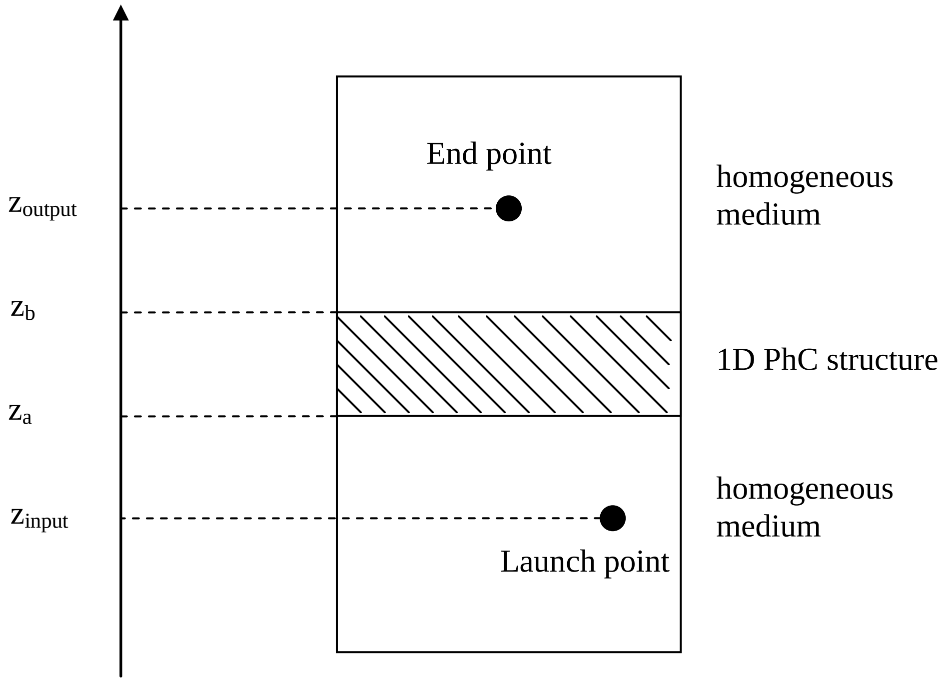

Fig. A. 3. 1. Layout of the numerical experiment for calculation of group velocity in a 1D photonic crystal structure

The beam propagates through structure in *z* direction. After wave propagation through all three subsections, the output beam is monitored in the third subsection after predefined time *T*. From the output field monitored by the time monitor, one can determine the position of the envelope of the light pulse after a given time *T* and then one can calculate the group velocity.

In general, if the beam propagates in a homogeneous medium, group velocity in *z* direction is determined as:

$$v_{gr} = \frac{\Delta z}{T}$$
$$\Delta z = z_{output} - z_{input} \tag{A.3.1}$$

Where: v_{gr} is the group velocity

Δz is the distance of beam propagation

z_{input} is the position of the launch point

z_{output} is the position of the beam after propagation

T the time the beam needs to propagate from z_{input} to z_{output}

In our case, the beam propagates both outside and inside the photonic crystal structure, so the group velocity must be calculated in a more complicated way.

We have:

$$v_{gr,sl} \cdot \Delta t_1 + v_{gr,grat} \cdot \Delta t_2 + v_{gr,sl} \cdot \Delta t_3 = \Delta z \tag{A.3.2}$$

Where: $v_{gr,sl}$ is the group velocity in homogeneous medium (slab waveguide)

$v_{gr,grat}$ is the group velocity in a grating structure (1D photonic crystal structure)

Δt_1 is the time the beam needs to propagate from the input position to the front of the grating (from z_{input} to z_a)

Δt_2 is the time the beam needs to propagate in grating structure (from z_a to z_b)

Δt_3 is the time the beam needs to propagate from ending position of the grating structure to the end point(from z_b to z_{output})

Group velocity in a homogeneous medium $v_{gr,sl}$ can be easily obtained by separate simulation and analysis using equation (A.3.1)

From equation (A.3.2), the group velocity in a 1D photonic crystal structure can be calculated as:

$$v_{gr,grat} = \frac{z_b - z_a}{T - \left(\frac{z_a - z_{input} + z_{output} - z_b}{v_{gr,sl}} \right)} \tag{A.3.3}$$

$v_{gr,grat}$ is then calculated by writing a program in visual C++

A.4 Compensation of the chromatic dispersion using a photonic crystal structure

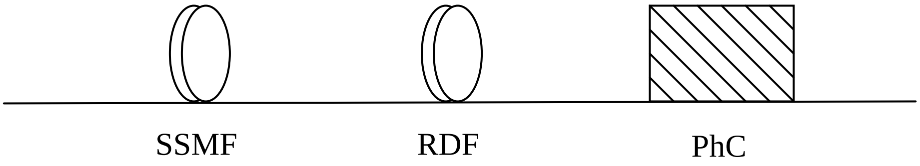

Fig. A.4.1. Compensation scheme

Given: SSMF with the length L_1 and chromatic dispersion D_{21}

PhC with the length L_3 and chromatic dispersion D_{23}

Calculate: The length of RDF structure L_2 with given chromatic dispersion D_{22}

In the case of full compensation:

$$\begin{aligned} &L_1 D_{21} + L_2 D_{22} + L_3 D_{23} = 0 \\ &\Rightarrow L_2 = \frac{-L_1 D_{21} - L_3 D_{23}}{D_{22}}. \end{aligned} \tag{A.4.1}$$

A.5 Program for pattern generation

In some cases, there is no available pattern in the program fullwave and one has to generate a new pattern by oneself.

Here we show the way to create photonic crystal structures which are oriented at a specific angle with respect to the straight boundaries.

A.5.1 2D pattern with polygons (squares) which are oriented at an angle of 45 degrees with respect to the straight boundaries

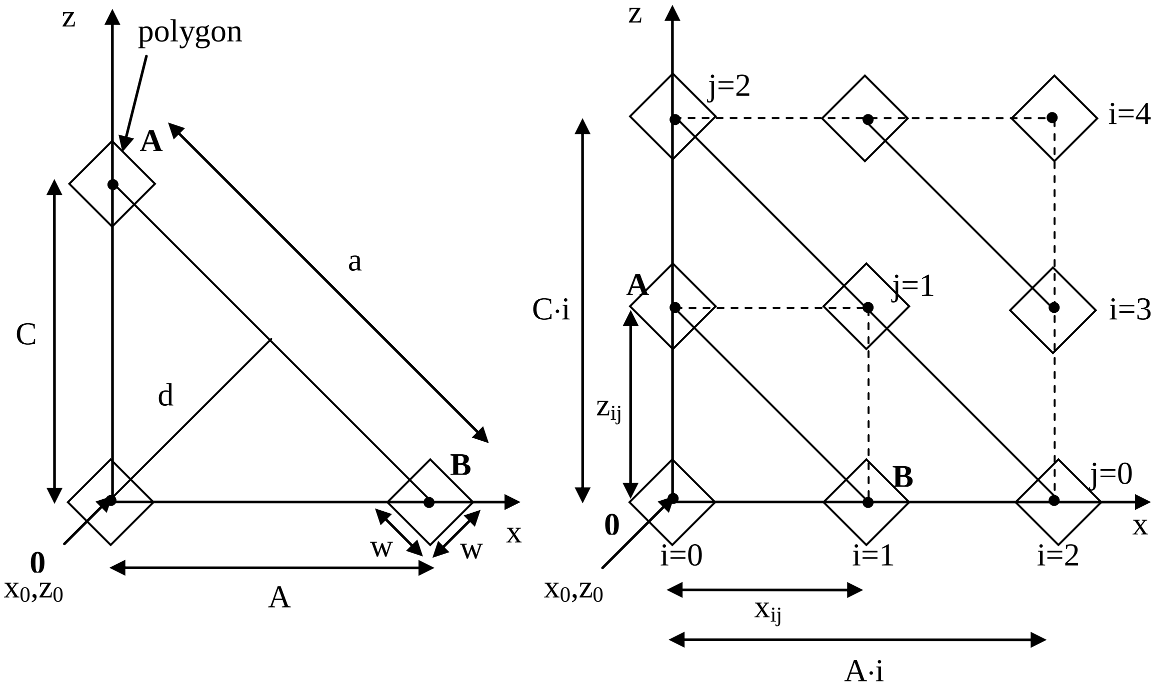

a) b)

Fig. A.5.1. Pattern generation model for 2D grating

Given: the width *w* of the polygons

the distance *d* between two diagonals

the maximum number of polygons *N* in the second diagonal (for the square grating we have $N = 2$)

the starting position x_0, z_0 of polygons in the grating structure

the maximum number of polygons in *x* direction N_x

the maximum number of polygons in *z* direction N_z

Aim: generation of the photonic crystal structure as in Fig. A.5.1.b

Fig. A.5.1.a is a detail of the grating structure in Fig. A.5.1.b.

The number of polygons in each direction *x* and *z* and the number of polygons in the second diagonal (*i=1*) can be freely chosen to get the desired photonic crystal structure. For a square grating structure the number of polygons in the second diagonal is 2. One can also choose the width w of the polygon and the distance d between two diagonals.

The position of a polygon can be calculated as:

$$\begin{aligned} x_{ij} &= A \cdot i - \frac{A}{N-1} \cdot j \\ z_{ij} &= \frac{C}{N-1} \cdot j \\ &\textit{where}: \\ A &= \sqrt{\frac{a^2}{2} - a\sqrt{\frac{a^2}{4} - d^2}} \\ C &= \sqrt{\frac{a^2}{2} + a\sqrt{\frac{a^2}{4} - d^2}} \end{aligned} \qquad \text{(A.5.1)}$$

and:

i: the index of a diagonal

j: the index of polygon in the diagonal

x_{ij}, z_{ij}: position of the polygon in the grating structure

$a = (N\text{-}1)\cdot w$

The number of diagonals is given by $(N_x + N_z - 1)$.

All the calculation and the generation of the data file of the structure to further use in fullwave are done by writing a program in visual C++

A.5.2 Pattern with rectangular stripes which are oriented at an angle of 45 degrees with respect to the straight boundaries

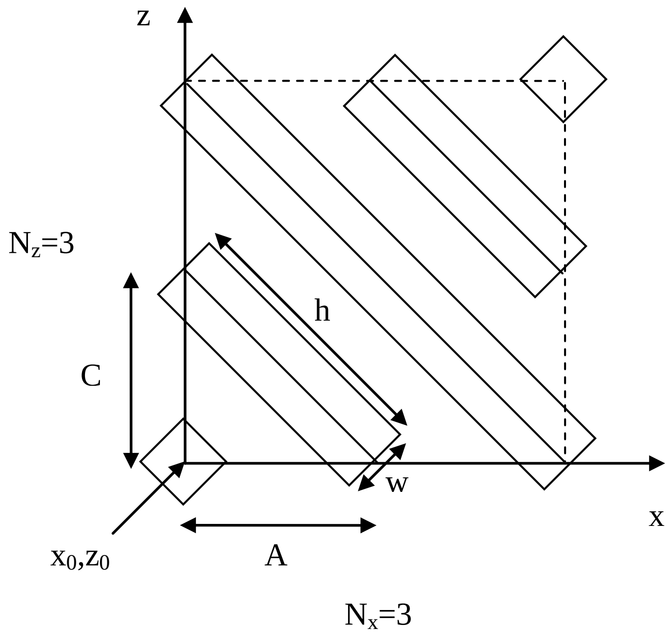

Fig. A.5.2. Pattern generation model with stripes rectangles which are oriented in 45 degrees with respect to the straight boundaries

Given: A, C, w, N_x, N_z

N_x: the maximum number of intersections between the x-axis and the grating center lines

N_z: the maximum number of intersections between the coordinate z and the grating line

w: the width of the polygons

l: the lengths of the polygons which are changed in every diagonal

For the above structure: $l = w$ in the 1st diagonal, $l = h$ in the 2nd diagonal, $l = 2 \cdot h$ in the 3rd diagonal, $l = h$ in the 4th diagonal, $l = w$ in the 5th diagonal

Calculate: the grating structure as in Fig. A.5.2

The length of the polygon in the second diagonal is given by:

$$h = \sqrt{A^2 + C^2}$$

The number of diagonals *i* is given by (N_x+ N_z-1).

The center position (*x*,*z*) and the length l of the polygons can be calculated as follows:

We have to distinguish three cases and we have to take care of special sub-intervals:

1. $N_z < N_x$
    - $0 \le i \le N_z - 1$

      $$x = x_0 + \frac{A}{2} \cdot i$$

      $$z = z_0 + \frac{C}{2} \cdot i$$

      $$l = h \cdot i$$

      If $i = 0$ then $l = w$
    - $N_z \le i \le N_x - 1$

      $$x = x_0 + \frac{A}{2} \cdot (N_z - 1) + (i - N_z + 1) \cdot A$$

      $$z = z_0 + \frac{C}{2} \cdot (N_z - 1)$$

      $$l = h \cdot (N_z - 1)$$
    - $N_x \le i \le N_x + N_z - 2$

      $$x = x_0 + \frac{A}{2} \cdot (N_z - 1) + A \cdot (N_x - N_z) + \frac{A}{2} \cdot (i - N_x + 1)$$

      $$z = z_0 + \frac{C}{2} \cdot (N_z - 1) + \frac{C}{2} \cdot (i - N_x + 1)$$

      $$l = h \cdot (N_z - 1) - h \cdot (i - N_x + 1)$$

      If $l = 0$ then l is assigned to w
2. $N_z > N_x$
    - $0 \le i \le N_x - 1$

      $$x = x_0 + \frac{A}{2} \cdot i$$

      $$z = z_0 + \frac{C}{2} \cdot i$$

      $$l = h \cdot i$$

      If $i = 0$ then $l = w$

- $N_x \le i \le N_z$-1

  $$x = x_0 + \frac{A}{2} \cdot (N_x - 1)$$
  $$z = z_0 + \frac{C}{2} \cdot (N_x - 1) + (i - N_x + 1) \cdot C$$
  $$l = h \cdot (N_x - 1)$$

- $N_z \le i \le N_x + N_z$-2

  $$x = x_0 + \frac{A}{2} \cdot (N_x - 1) + \frac{A}{2} \cdot (i - N_z + 1)$$
  $$z = z_0 + \frac{C}{2} \cdot (N_x - 1) + C \cdot (N_z - N_x) + \frac{C}{2} \cdot (i - N_z + 1)$$
  $$l = h \cdot (N_x - 1) - h \cdot (i - N_z + 1)$$

  If l = 0 then l is assigned to w

3. $N_z = N_x$

- $0 \le i \le N_x$-1

  $$x = x_0 + \frac{A}{2} \cdot i$$
  $$z = z_0 + \frac{C}{2} \cdot i$$
  $$l = h \cdot i$$

  If i = 0 then $l = w$

- $N_x \le i \le Nx+Nz$-2

  $$x = x_0 + \frac{A}{2} \cdot (N_x - 1) + \frac{A}{2} \cdot (i - N_x + 1)$$
  $$z = z_0 + \frac{C}{2} \cdot (N_x - 1) + \frac{C}{2} \cdot (i - N_x + 1)$$
  $$l = h \cdot (N_x - 1) - h \cdot (i - N_x + 1)$$

  If l = 0 then l is assigned to w

All the calculation and the generation of the data file of the structure to further use in fullwave are done by writing a program in visual C++

List of frequently used abbreviations and symbols

Abbreviations

1D	One Dimensional
2D	Two Dimensional
3D	Three Dimensional
DWDM	Dense Wavelength Division Multiplexing
EL	Electroluminescent
FDTD	Finite Different Time Domain
FWHM	Full Width at Half Maximum
LD_1,..LD_n	Laser Diode
LED	Light Emitting Diodes
Lin	Linear
Nonlin	Nonlinear
m	Modulated
NA	Normalized Aperture
NAG	Numerical Algorithms Group
O/E_1,..O/E_n	Optical/Electrical Converter
OTDM	Optical Time Division Multiplex

PhCs	Photonic Crystals
PhCDC	Photonic Crystal Dispersion Compensator
PLCs	Planar Lightwave Circuit
RDF	Reverse Dispersion Fiber
RZ-signal	Return to Zero signal
SSMF	Standard Single-Mode Fiber
T_1, T_2	Transition of area 1, 2
TE	Transverse Electric
TM	Transverse Magnetic
u_1, u_2	Unmodulated area 1, 2
WVD	Wave-Vector Diagram

Symbols

a	grating constant
$a_0,a_1..a_7$	coefficients of a seven order polynom
$\vec{b}_1,\vec{b}_2$	reciprocal lattice vectors
c_0	speed of light in vacuum
c_{med}	speed of light in a medium
d_0	diameter of the Gaussian beam waist at its $1/e^2$ intensity points
$dnback$	small changing in the background refractive index
D_2	chromatic dispersion [ps/nm.km]
D_3	dispersion slope [$ps/nm^2.km$]
D_4	dispersion curvature [$ps/nm^3.km$]
$\vec{E}$	electric field vector
f_{00}, f_{mn}	dimensionless frequencies
$\vec{G}_j$	primitive reciprocal lattice vector
$\vec{H}$	magnetic field vector
F^*	complex conjugation of F

$\vec{H}_{n,\vec{k}}$	periodic envelope function of the magnetic field
incl0,2,4	angles of inclination of 0, 2, 4 degrees
J_1	Bessel function
$\vec{k}$	Bloch wave vector
L	the width of modulated area in waveguide
n_0, n_1	refractive index of the background and the columns in a photonic crystal waveguide
nback	background refractive index
neff	effective refractive index
nhom	refractive index of a homogeneous medium
n_{med}	refractive index of the medium
$n(x,y)$	refractive index function
r	radius
$\vec{R}_i$	lattice vector (i=1,2,3 for a crystal with periodicity in all three dimensions)
t	time
T	time
U	symbol of unmodulated area in waveguide

Ü	Transition between unmodulated and modulated waveguide
$\vec{v}_g$	group velocity vector
v_{gr}	group velocity
x,y,z	cartesian coordinates
$\alpha^{(u)}$	angle of inclination
$\alpha^{(m)}$	beam-steering angle
β	propagation constant
β_1	group delay of the carrier wave
β_x, β_y	components of propagation constant in the wave-vector diagram
β_u, β_m	average of propagation constant in unmodulated and modulated waveguides
Δt	time step
$\Delta_x, \Delta_y, \Delta_z$	grid spacing in x,y,z
δ_{ij}	Kronecker delta function
ε	dielectric constant
θ_d	divergence angle

Λ	grating constant
λ_0	light wavelength in vacuum
μ	permeability
ϕ_{incl}	angle of inclination of grating structure
ψ	angle of a wave vector ralative to grating structure
Ω	normalized frequency with respect to the case of Bragg reflection
$\tau(\lambda)$	group delay [ns/km]

References

[AASN03] Y. Akahane, T. Asano, B. S. Song, and S. Noda, "Investigation of high-Q channel drop filters using donor-type defects in two-dimensional photonic crystal slabs," Appl. Phys. Lett. **83**, 1512-1514 (2003)

[AASN05] Y. Akahane, T. Asano, B. S. Song, and S. Noda, "Fine-tuned high-Q photonic-crystal nanocavity," Opt. Express **13**, 1202-1214 (2005)

[AMHIBSA02] K. Aoki, H. T. Miyazaki, H. Hirayama, K. Inoshita, T. Baba, N. Shinya, Y. Aoyagi, "Three-dimensional photonic crystals for optical wavelengths assembled by micromanipulation," Appl. Phys. Lett. **81**, 3122-3124 (2002)

[AWP99] J. Arriaga, A. J. Ward, and J. B. Pendry, "Order N photonic band structures for metals and other dispersive materials," Phys. Rev. B **59**, 1874-1877 (1999)

[BCO05] I. Bulu, H. Caglayan, and E. Ozbay, "Negative refraction and focusing of electromagnetic wave by metallodielectric photonic crystals," Phys. Rev. B **72**, 045124 (2005)

[Blo29] F. Bloch, "Über die Quantenmechanik der Elektronen in Kristallgittern," Z. Phys. **52**, 555-600 (1929)

[BMSQTTA04] A. Berrier, M. Mulot, M. Swillo, M. Qiu, L. Thylén, A. Talneau, and S. Anand, "Negative refraction at infrared wavelengths in a two-dimensional photonic crystal," Phys. Rev. Lett. **93,** 073902 (2004)

[BN02] T. Baba, M. Nakamura, "Photonic crystal light deflection devices using the superprism effect," IEEE J. Quan. Elec. **38,** 909-914 (2002)

[BO01] T. Baba, and D. Ohsaki, "Interfaces of Photonic crystals for high efficiency light transmission," Jpn. J. Appl. Phys. **40**, 5920-5924 (2001)

[BPMW95] P. M. Bell, J. B. Pendry, L. M. Moreno, and A. J. Ward, "A program for calculating photonic band structures and transmission coefficients of complex structures," Comput. Phys. Comm. **85**, 306-322 (1995)

[Bri46] L. Brillouin, "Wave Propagation in Periodic Structures," *McGraw-Hill, New York,* (1946)

[CAOFS03] E. Cubukcu, K. Aydin, E. Ozbay, S. Foteinopoulou, C. M. Soukoulis, "Subwavelength Resolution in a Two-Dimensional Photonic-Crystal-Based Superlens," Phys. Rev. Lett. **91**, 207401 (2003)

[CBB05] J. V. Campenhout, P. Bienstman, R. Baet, "Band-edge lasing in gold-clad photonic-crystal membranes," IEEE J. Selec. Areas Commun. **23**, 1418-1423 (2005)

[CBMR97] J. Chongjun, Q. Bai, Y. Miao, and Q. Ruhu, "Two-dimensional photonic band structure in the chiral medium-transfer matrix method," Opt. Commun. **142**, 179-183 (1997)

[CDYSHS94] C. T. Chan, S. Datta, Q. L. Yu, M. Sigalas, K. M. Ho, C. M. Soukoulis, "New structures and algorithms for photonic band gaps," Physica A **211**, 411-419 (1994)

[CLH95] C. T. Chan, Q. L. Lu, and K. M. Ho, "Order-N spectral method for electromagnetic waves," Phys. Rev. B **51**, 16635-16642 (1995)

[CLLXWL07] C. Chen, X. Li, H. Li, K. Xu, J. Wu, J. Lin, "Bandpass Filters Based on Phase-shifted Photonic Crystal Waveguide Gratings", Opt. Express **15**, 11278-11284 (2007)

[CMIN01] A. Chutinan, M. Mochizuki, M. Imada, and S. Noda, "Surface-emitting channel drop filters using single defects in two-dimensional photonic crystal slabs," Appl. Phys. Lett. **79**, 2690-2692 (2001)

[CMM03] R. Costa, A. Melloni, M. Martinelli, "Bandpass Resonant Filters in Photonic-Crystal Waveguides", IEEE Photon. Technol. Lett. **15**, 401-403 (2003)

[CON02] A. Chutinan, M. Okano, and S. Noda, "Wider bandwidth with high transmission through waveguide bends in two-dimensional photonic crystal slabs," Appl. Phys. Lett. **80**, 1698-1700 (2002)

[DEWSL06] G. Dolling, C. Enkrich, M. Wegener, C. M. Soukoulis, and S. Linden, "A low-loss negative-index metamaterial at telecommunication wavelengths," Opt. Letters **31**, 1800-1802 (2006)

[DKSCJLKL03] Y. R. Do, Y. C. Kim, Y. W. Song, C. O. Cho, H. Jeon, Y. J. Lee, S. H. Kim, and Y. H. Lee, "Enhanced light extraction from organic light-emitting diodes with 2D SiO_2/SiN_x photonic crystals," Adv. Mater. **15**, 1214-1218 (2003)

[EAPSO01] R. L. Espinola, R. U. Ahmad, F. Pizzuto, M. J. Steel, and R. M. Osgood, "A study of high-index-contrast 90 degree waveguide bend structures," Opt. Express **8**, 517-528 (2001)

[ET96] J. M. Elson, and P. Tran, "Coupled-mode calculation with the R-matrix propagator for the dispersion of surface waves on truncated photonic crystal," Phys. Rev. B **54**, 1711-1715 (1996)

[FJWKO05] G. Freymann, S. John, S. Wong, V. Kitaev, G. A. Ozin, "Measurement of group velocity dispersion for finite size three-dimensional photonic crystals in the near-infrared spectral region," Appl. Phys. Lett. **86**, 053108 (2005)

[Flo1883] G. Floquet, "Sur les équations differentielles linéaires à coefficients périodiques," Ann. Ecole Norm. Sup. **12,** 47-88 (1883)

[FUIANOTNS04] M. Fujita, T. Ueno, K. Ishihara, T. Asano, S. Noda, H. Ohata, T. Tsuji, H. Nakada, and N. Shimoji, "Reduction of operating voltage in organic light-emitting diode by corrugated photonic crystal structure," Appl. Phys. Lett. **85**, 5769-5771 (2004)

[FVJ96] S. Fan, P. R. Villeneuve, and J. D. Joannopoulos, "Large omnidirectional band gaps in metallodielectric photonic crystals," Phys. Rev. B **54**, 11245-11251 (1996)

[FYWSP06] S. Fan, M. F. Yanik, Z. Wang, S. Sandhu, M. L. Povinelli, "Advances in theory of photonic crystals," J. Lightwave Technol. **24**, 4493-4501 (2006)

[GMSEMFDPLAW07] C. Grillet, C. Monat, C. L. C. Smith, B. J. Eggleton, D. J. Moss, S. Fre'de'rick, D. Dalacu, P. J. Poole, J. Lapointe, G. Aers, R. L. Williams, "Nanowire coupling to photonic crystal nanocavities for single photon sources," Opt. Express **15**, 1267-1276 (2007)

[Gün1876] Günther, S. *Zeitschrift für Mathematik* **21**, 185 (1876)

[Hau84] H. A. Haus, *Waves and Fields in Optoelectronics*, Englewood Cliffs, NJ: Prentice-Hall (1984)

[HCS90] K. M. Ho, C. T. Chan, C. M. Soukoulis, "Existence of a photonic gap in periodic dielectric structures," Phys. Rev. Lett. **65**, 3152-3155 (1990)

[HKF03] T. D. Happ, M. Kamp, A. Forchel et al., "Two-dimensional photonic crystal coupled-defect laser diode," Appl. Phys. Lett. **82**, 4-6 (2003)

[HSHLKF06] R. Herrmann, T. Sünner, T. Hein, A. Löffler, M. Kamp, and A. Forchel, "Ultrahigh-quality photonic crystal cavity in GaAs," Opt. Letters **31**, 1229-1231 (2006)

[HSS06] S. T. Hanic, C. M. de Sterke, J. J. Steel, "Design of high-Q cavities in photonic crystal slab heterostructures by air-holes infiltration", Opt. Express **14**, 12451-12456 (2006)

[JFVJ99] S. G. Johnson, S. Fan, P. R. Villeneuve, and J. D. Joannopoulos, "Guided modes in photonic crystal slabs ," Phys. Rev. B **60**, 5751 (1999)

[JISWJF02] S. G. Johnson, M. Ibanescu, M. A. Skorobogatiy, O. Weisberg, J. D. Joannopoulos, and Y. Fink, "Perturbation theory for Maxwell’s equations with shifting material boundaries," Phys. Rev. E **65,** 066611 (2002)

[JJ01] S. G. Johnson, and J. D. Joannopoulos, "Block-iterative frequency-domain methods for Maxwell’s equations in a planewave basis," Opt. Express **8**, 173-190 (2001)

[JJ03] S. G. Johnson, and J. D. Joannopoulos (2003) *Introduction to Photonic crystals: Bloch’s theorem, band diagrams, and Gaps (but no defects)*, Photonic crystals tutorials by Prof. S. Johnson (2003)

[Joa95] J. Joannopoulos et al, "Photonic Crystals", *Princeton Press, Princeton, N.J.*, (1995)

[Joh87] S. John, "Strong Localization of Photons in Certain Disordered Dielectric Superlattices", Phys. Rev. Lett. **58**, 2486 (1987)

[JPR03] A. S. Jugessur, P. Pottier, R. M. De la Rue, "One-dimensional Periodic Photonic Crystal Microcavity Filters with Transition Mode-matching Features Embedded in Ridge Waveguides", Electron. Lett **39**, 367-368 (2003)

[JPR04]	A. S. Jugessur, P. Pottier, R. M. De la Rue, "Engineering the filter response of photonic crystal microcavity filters", Opt. Express **12**, 1304-1312 (2004)
[KBR01]	J. C. Knight, T. A. Birks and P. St. J. Russell, "Holey silica fibres," in Optics of Nanostructured Materials, Editors V. A. Markel and T. F. George, 39 (John Wiley & Sons, New York, 2001)
[KK99]	H. Kosaka, T. Kawashima et al.,"Superprism phenomena in photonic crystals: Toward microscale lightwave circuits," J. Lightwave Technol. **17**, 2032-2038 (1999)
[KKKLK04]	S. H. Kwon, S. H. Kim, S. K. Kim, Y. H. Lee, and S. B. Kim, "Small, low-loss heterogeneous photonic bandedge laser," Opt. Express **12**, 5356-5361 (2004)
[KKTNTSK98]	H. Kosaka, T. Kawashima, A.Tomita, M. Notomi, T. Tamamura, T. Sato, and S. Kawakami, "Superprism phenomena in photonic crystals," Phys. Rev. B **58**, 10096-10099 (1998)
[KSKF08]	S. H. Kwon, T. Sünner, M. Kamp, A. Forchel, "Ultrahigh-Q photonic crystal cavity created by modulating air hole radius of a waveguide", Opt. Express **16**, 4605-4614 (2008)
[LCSSMSP05]	Z. Lu, C. Chen, C. A. Schuetz, S. Shi, J. A. Murakowski, G. J. Schneider, D. W. Prather, "Subwavelength imaging by a flat cylindrical lens using optimized negative refraction," Appl. Phys. Lett. **87**, 091907 (2005)
[Lem02]	O. Leminger, "Wave-vector diagrams for two-dimensional photonic crystals," Opt. and Quant. Electron. **34**, 435-443 (2002)
[LF99]	S. Y. Lin, J. G. Fleming, "A three-dimensional optical photonic crystal," J. Lightwave Technol. **17**, 1944-1947 (1999)

[LFHSBHSZKB98] S. Y. Lin, J. G. Fleming, D. L. Hetherington, B. K. Smith, R. Biswas, K. M. Ho, M. M. Sigalas, W. Zubrzycki, S. R. Kurtz, J. Bur, "A three-dimensional photonic crystal operating at infrared wavelengths," Nature **394**, 251-253 (1998)

[LJJ02] C. Luo, S. G. Johnson, and J. D. Joannopoulos, "All-angle negative refraction in a three-dimensionally periodic photonic crystal," Appl. Phys. Lett. **81**, 2352-2354 (2002)

[LJJP02] C. Luo, S. G. Johnson, J. D. Joannopoulos, and J. B. Pendry, "All angle negative refraction without negative effective index," Phys. Rev. B **65**, 201104 (2002)

[LJJP03] C. Luo, S. G. Johnson, J. D. Joannopoulos, J. B. Pendry, "Subwavelength imaging in photonic crystals," Phys. Rev. B **68**, 045115 (2003)

[LMSSSP05] Z. Lu, J. A. Murakowski, C. A. Schuetz, S. Shi, G. J. Schneider, and D. W. Prather, "Three-dimensional subwavelength imaging by a photonic-crystal flat lens using negative refraction at microwave frequencies," Phys. Rev. Lett **95,** 153901 (2005)

[LL03] Z. Y. Li, and L. L. Lin, "Evaluation of lensing in photonic crystal slabs exhibiting negative refraction," Phys. Rev. B **68,** 245110 (2003)

[LL90] K. M. Leung, Y. F. Lu, "Full vector wave calculation of photonic bandgap structures in faced-centered-cubic dielectric medium," Phys. Rev. Lett. **65**, 2646-2649 (1990)

[LLFLFTC07] J. Li, M. H. Lu, T. Fan, X. K. Liu, L. Feng, Y. F. Tang, and Y. F. Chen, "All-angle negative refraction imaging effect with complex two-dimensional hexagonal photonic crystals," J. Appl. Phys. **102**, 073538 (2007)

[LSSP05] Z. Lu, S. Shi, C. A. Schuetz, D. W. Prather, "Experimental demonstration of negative refraction imaging in both amplitude and phase," Opt. Express **13,** 2007-2012 (2005)

[LSSMP05] Z. Lu, S. Shi, C. A. Schuetz, J. A. Murakowski, D.W. Prather, "Three-dimensional photonic crystal flat lens by full 3D negative refraction," Opt. Express **13**, 5592-5599 (2005)

[MA70] I. M. Mason and E. A. Ash, "Acoustic surface-wave beam diffraction on anisotropic substrates," J. Appl. Phys. **42**, 5343-5351 (1970)

[MCKFVJ96] A. Mekis, J. C. Chen, I. Kurland, S. H. Fan, P. R. Villeneuve, and J. D. Joannopoulos, "High transmission through sharp bends in photonic crystal waveguides," Phys. Rev. Lett. **77**, 3787-3790 (1996)

[MJFVHJ99] C. Manolatou, S. G. Johnson, S. Fan, P. R. Villeneuve, H. A. Haus, J. D. Joannopoulos, "High-density integrated optics," J. Lightwave Technol. **17**, 1682-1692 (1999)

[MM05] A. Martinez, and J. Marti, "Analysis of wave focusing inside a negative-index photonic-crystal slab," Opt. Express **13**, 2858-2868 (2005)

[MMGM04] A. Martinez, H. Miguez, A. Griol, and J. Marti, "Experimental and theoretical analysis of self-focusing of light by a photonic crystal lens," Phys. Rev. B **69**, 165119 (2004)

[MRBJA93] R. D. Meade, A. Rappe, K. Brommer, J. D. Joannopoulos, and O. Alerhand, "Accurate theoretical analysis of photonic band-gap materials," Phys. Rev. B **48**, 8434 (1993)

[NKB07] K. Nozaki, S. Kita, and T. Baba, "Room temperature continuous wave operation and controlled spontaneous

	emission in untrasmall photonic crystal nanolaser," Opt. Express **15**, 7506-7514 (2007)
[Nod06]	S. Noda, "Recent Progresses and Future Prospects of Two- and Three-Dimensional Photonic Crystals," J. Lightwave Technol. **24**, 4554-4567 (2006)
[Not00]	M. Notomi, "Theory of light propagation in strongly modulated photonic crystals: Refractionlike behavior in the vicinity of the photonic bad gap," Phys. Rev. B **62**, 10696-10705 (2000)
[NTYC00]	S. Noda, K. Tomoda, N. Yamamoto, and A. Chutinan, "Full three-dimensional photonic bandgap crystals at near-infrared wavelengths," Sience **289**, 604 (2000)
[NYSTTY01]	M. Notomi, K. Yamada, A. Shinya, J. Takahashi, C. Takahashi, and I. Yokohama, "Extremely large group-velocity dispersion of line-defect waveguides in photonic crystal slabs," Phys. Rev. Lett. **87**, 253902 (2001)
[NYT02]	M. Nakazawa, T. Yamamoto and K. R. Tamura, "Ultrahigh-Speed OTDM Transmission beyond 1 Tera Bit-Per-Second Using a Femtosecond Pulse Train," IEICE Trans.Electron, vol. **E85-C**, No.1, 117-125 (2002)
[OKN03]	M. Okano, S. Kako, and S. Noda, "Coupling between a point-defect cavity and a line-defect waveguide in three-dimensional photonic crystal," Phys. Rev. B **68**, 235110 (2003)
[Pen00]	J. B. Pendry, "Negative Refraction Makes a Perfect Lens," Phys. Rev. Lett. **85**, 3966-3969 (2000)
[PKPL05]	D. Park, S. Kim, I. Park, H. Lim, "Higher Order Optical Resonant Filters Based on Coupled Defect Resonants in Photonic Crystals", J. Lightwave Technol. **23**, 1923-1928 (2005)

[PLVSDS04] P. V. Parimi, W. T. Lu, P. Vodo, J. Sokoloff, J. S. Derov, S. Sridhar, "Negative refraction and left-handed electromagnetism in microwave photonic crystals," Phys. Rev. Lett. **92**, 127401 (2004)

[PM92] J. B. Pendry, A. MacKinnon, "Calculation of photon dispersion relations," Phys. Rev. Lett. **69**, 2772-2775 (1992)

[PTVF92] W. H. Press, S. Teukolsky, W. Vetterling, and B. Flannery, *Numerical recipes in FORTRAN*, Cambridge University Press, New York, 455 (1992)

[Qua03] H. Quan, "Optimierung der Simulationsalgorithmen zum Entwurf optischer Vielkanal-Kommunikationssysteme unter Berücksichtigung der Vierwellenmischung", PhD thesis, *Technical University of Kaiserslautern*, (2003)

[Ray1888] J. W. S. Rayleigh, "On the remarkable phenomenon of crystalline reflexion described by Prof. Stokes," Phil. Mag. **26**, 256-265 (1888)

[RKR02] W. H. Reeves, J. C. Knight, P. St. J. Russel et al, "Demonstration of ultra-flattened dispersion in photonic crystal fibers," Opt. Express **10**, 609-613 (2002)

[RTLPSHS04] T. Ritari, J. Tuominen, H. Ludwigsen, J. C. Petersen, T. Sorensen, T. P. Hansen, H. R. Simonsen, "Gas sensing using air-guiding photonic bandgap fibers," Opt. Express **12**, 4080-4087 (2004)

[Rus81] P. St. J. Russell, "Thick Grating Focussing-Device-Design using Poynting-Vector-Optics," Appl. Phys. B **26**, 37-42 (1981)

[Rus86] P. St. J. Russell, "Interference of integrated Floquet-Bloch waves," Phys. Rev. A **33**, 3232-3242 (1986)

[SAN04] A. Sugitatsu, T. Asano, and S. Noda, "Characterization of line-defect-waveguide lasers in two-dimensional photonic-crystal slabs," Appl. Phys. Lett. **84**, 5395-5397 (2004)

[Sch1904] A. Schuster, *An Introduction to the Theory of Optics*, Edward Arnold, London (1904)

[SF06] H. Shin, and S. Fan, "All-angle negative refraction for surface plasmon waves using a Metal-Dielectric-Metal Structure," Phys. Rev. Lett. **96**, 073907 (2006)

[SHE03] J. Smajic, C. Hafner, D. Erni, "Design and optimization of an achromatic photonic crystal bend," Opt. Express **11**, 1378-1384 (2003)

[Sil72] R. A. Silin, "Optical properties of artificial dielectrics," Radiophysics and Quantum Electronics **15**, 615-624 (1972)

[Sil78] R. A. Silin, "Possibility of creating plane-parallel lenses," Opt. Spektrosk. **44**, 189-191 (1978)

[SLLH04] C. Sauvan, G. Lecamp, P. Lalanne, J. P. Hugoni, "Modal-reflectivity enhancement by geometry tuning in Photonic Crystal microcavities", Opt. Express **13**, 245-255 (2004)

[SMSOON05] K. Sakai, E. Miyai, T. Sakaguchi, D. Ohnishi, T. Okano, and S. Noda, "Lasing band-edge identification for a surface emitting photonic crystal laser," IEEE J. Selec. Areas Commun. **23**, 1335-1340 (2005)

[SS97] K. Sakoda, H. Shiroma, "Numerical method for localized defect modes in photonic lattices," Phys. Rev. B **56**, 4830-4835 (1997)

[TAAN04] H. Takano, Y. Akahane, T. Asano, and S. Noda, "In-plane-type channel drop filter in a two-dimensional photonic crystal slab," Appl. Phys. Lett. **84**, 2226-2228 (2004)

[TSAN06] H. Takano, B. S. Song, T. Asano, and S. Noda, "Highly efficient multi-channel drop filter in a two-dimensional hetero photonic crystal," Opt. Express **14,** 3491-3496 (2006)

[UZ80] R. Ulrich, and R. Zengerle, "Optical Bloch waves in periodic planar waveguides," Integrated and Guided-Wave Optics, Incline Village, NV, USA, 1980, TuB1/1-4 (1980)

[Ves68] V. G. Veselago, "The electrodynamics of substances with simultaneous negative values of ε□ and μ," Sov. Phys. Usp. **10**, 509-514 (1968)

[VRLHPPCH06] P. Velha, J. C. Rodier, P. Lalanne, J. P. Hugonin, D. Peyrade, E. Picard, T. Charvolin, E. Hadji, "Ultra-high-refrectivity photonic-bandgap mirrors in a ridge SOI waveguide", New Journal of Physics **8**, 22501 (2006)

[VP94] P. R. Villeneuve, M. Piché, "Photonic bandgaps in periodic dielectric structures", *Prog. Quantum Electron.* **18,** 153 (1994)

[WP00] A. J. Ward, J. B. Pendry, "A program for calculating photonic band structures, Green’s functions and transmission/reflection coefficients using a non-orthogonal FDTD method," Comput. Phys. Comm. **128**, 590-621 (2000)

[WRK04] X. Wang, Z. F. Ren, and K. Kempa, "Unrestricted superlensing in a triangular two-dimensional photonic crystal," Opt. Express **12**, 2919-2924 (2004)

[XQRH04] S. Xiao, M. Qiu, Z. Ruan, and S. He, "Influence of the surface termination to the point imaging by a photonic crystal slab with negative refraction," Appl. Phys. Lett. **85**, 4269-4271 (2004)

[Yab87] E. Yablonovitch, "Inhibited Spontaneous Emission in Solid-State Physics and Electronics," Phys. Rev. Lett. **58**, 2059-2062 (1987)

[Yee96] K. S. Yee, "Numerical solution of initial boundary value problems involving Maxwell’s equations in isotropic media," IEEE Trans. Anttennas Propagat., AP-**14**, 302 (1996)

[YFSK06] N. Yokoi, T. Fujisawa, K. Saitoh, M. Koshiba, "Apodized Photonic Crystal Waveguide Gratings", Opt. Express **14**, 4459-4468 (2006)

[YGL91] E. Yablonovitch, T. J. Gmitter, K. M. Leung, "Photonic Band Structure: The Face-Centered-Cubic Case Employing Nonspherical Atoms," Phys. Rev. Lett. **67**, 2295-2298 (1991)

[YSN04] A. Yokoo, H. Suzuki, and M. Notomi, "Organic photonic crystal band edge laser fabricated by direct nanoprinting," Jpn. J. Appl. Phys. **43**, 4009-4011 (2004)

[Zen79] R. Zengerle, "Light propagation in singly and doubly periodic planar waveguides," PhD Thesis, *University of Stuttgart*, (1979)

[Zen87] R. Zengerle, "Light propagation in singly and doubly periodic planar waveguides," J. Modern Optics **34**, 1589-1617 (1987)

[Zen88] R. Zengerle, "Polarization splitter based on beam steering in periodic planar optical waveguides," Electron. Lett. **24**, 11-12 (1988)

[Zen04] R. Zengerle, "Photonic Crystal Waveguides: Dispersion, Anomalous Refraction and Application," Advances in Solid State Physics **44**, Springer, (2004)

[Zen05] R. Zengerle, *Vorlesung 3D optoelektronik*, University of Kaiserslautern (2005)

[ZGCSR08]	A. R. M. Zain, M. Gnan, H. M. H. Chong, M. Sorel, R. M. De la Rue, "Tapered Photonic Crystal Microcavities Embedded in Photonic Wire Waveguides with Large Resonance Quality-Factor and High Transmission", IEEE Photon. Technol. Lett. **20**, 6-8 (2008)
[ZH05]	R. Zengerle, and P. C. Hoang, "Wide-angle beam refocusing using negative refraction in non-uniform photonic crystal waveguides," Opt. Express **13**, 5719-5730 (2005)
[ZL89]	R. Zengerle, O. Leminger, "Frequency-dependent focusing in doubly-periodic planar optical waveguides," Proceedings of the IOOC **89**, Kobe, (1989)
[ZL90]	R. Zengerle and O. Leminger, "Frequency demultiplexing based on beam steering in periodic planar optical waveguides," Journal of Optical Communications **11**, 11-12 (1990)
[ZL92]	R. Zengerle, O. Leminger, "Propagation of Gaussian beams in singly and doubly periodic dielectric wave-guides," Proceedings of the URSI International Symposium on Electromagnetic Theory, Sydney, pp 19 (1992)
[ZL95]	R. Zengerle, O. Leminger, "Phase-shifted Bragg-Grating Filters with Improved Transmission Characteristics", J. Lightwave Technol. **13**, 2354-2358 (1995)
[ZPLZW07]	X. H. Zou, W. Pan, B. Luo, W. L. Zhang, M. Y. Wang, "One-dimensional Photonic Crystal-Based Multichannel Filters Using Binary Phase-Only Sampling Aproach", J. Lightwave Technol. **25**, 2482-2486 (2007)
[ZS90]	Z. Zhang, S. Satpathy, "Electromagnetic wave propagation in periodic structures: Bloch wave solution of Maxwell equations," Phys. Rev. Lett. **65**, 2650-2653 (1990)

Tabellarischer Lebenslauf

Name:	Phuong Chi HOANG
Adresse:	Kurt-Schumacher-Str. 22 67663 Kaiserslautern
Geburtsdatum:	15. Juni 1976
Familienstand:	verheiratet
Staatsangehörigkeit:	vietnamesisch
Schulausbildung:	September 1982 – Juli 1991 Grundschule in Hanoi September 1991 – Juli 1994 Gymnasium in Hanoi
Hochschulaufnahmeprüfung:	Juli 1994
1. Studium:	September 1994 – Juli 1999 Studium der Elektronik an der Technischen Universität Hanoi, Vietnam
Studienabschluss:	Bachelor of Engineering
2. Studium:	März 2001 – März 2003 Studium der Elektrotechnik an der Technischen Universität Kaiserslautern
Studienabschluss:	Master of Science
Berufstätigkeit:	von Juli 1999 bis März 2001 Arbeiten an der Technischen Universität Hanoi, Vietnam seit Juli 2003 wissenschaftliche Mitarbeiterin am Lehrstuhl für Elektrodynamik und Optische Technologien der Technischen Universität Kaiserslautern